UNIVERSITY
OF TRENTO - Italy
DEPARTMENT OF INDUSTRIAL ENGINEERING

XXXII cycle

Doctoral School in Materials, Mechatronics
and Systems Engineering

Organic and hybrid polysiloxane-based scintillators and passive dosimeters

Enrico Zanazzi

June 2020

ORGANIC AND HYBRID POLYSILOXANE-BASED SCINTILLATORS AND PASSIVE DOSIMETERS

Enrico Zanazzi

E-mail: enrico.zanazzi-1@unitn.it

Approved by:

Prof. Alberto Quaranta, Advisor
Dept. of Industrial Engineering
University of Trento*, Italy.*

Ph.D. Commission:

Prof. Alessandro Pegoretti,
Dept. of Industrial Engineering
University of Trento*, Italy.*

Prof. Anna Paola Caricato,
Dept. of Mathematics and Physics
University of Salento*, Italy.*

Prof. Sandra Moretto,
INFN Padova, Italy.

University of Trento,

Department of Industrial Engineering

June 2020

University of Trento - Department of Industrial Engineering

Doctoral Thesis

Enrico Zanazzi – June 2020
Published in Trento (Italy) – by University of Trento

ISBN: - - - - - - - - -

Abstract

The growing interest towards polysiloxane-based radiation detection systems is related with the several advantages that polysiloxanes offer in comparison with other state-of-the-art plastic materials used in scintillation, like polyvinyltoluene and polystyrene. In this respect, polysiloxane elastomers offer higher thermal stability, flexibility and radiation hardness than the traditional plastic counterpart. For this reason, the study of polysiloxane-based systems for the detection of several types of radiation such as neutrons, high-energy photons and charged particles has recently received increasing attention by the scientific community. In this thesis, we report the current advances on both organic and hybrid polysiloxane-based radiation detection systems for scintillation and passive dosimetry applications. In this framework, we will start from the recent advances on organic polysiloxane-based scintillators for the detection of fast neutrons, with particular emphasis on their pulse-shape discrimination capabilities, allowing for the distinction of neutrons from the γ-ray background. The other and main part of the thesis will be then dedicated to hybrid nanostructured polysiloxane-based radiation detection systems. In this context, latest progress on polysiloxane scintillators embedding ^{6}LiF nanocrystals for thermal neutron detection will be presented, with particular focus on the role of the nanocrystal size and dispersion in the detection performances. Subsequently, polysiloxane/quantum dots nanocomposites will be investigated for their possible use in both scintillation and passive dosimetry. In this latter application, the optical properties of the samples are analyzed after irradiation, with the aim to correlate the radiation-induced effects with the radiation dose. Lastly, the role of the polymer matrix in the post-irradiation optical response of the nanocrystals will be investigated.

Table of Contents

Introduction

Radiation detectors are widely used across several fields, spanning from nuclear and particle physics experiments in scientific research, to material analyses in both scientific research and industries, to medicine for diagnostic and therapeutic purposes, and to safety and security.

Among the different types of radiation detectors, scintillation detectors offer the highest versatility in terms of operating modes, variety of detectable radiation types and energy range [1]. For this reason, the scientific community is dedicating large effort in studying and developing new scintillation detection systems. In this context, state-of-the-art commercial scintillators based on plastic materials such as polyvinyltoluene (PVT) and polystyrene (PS) suffer of intrinsic limitations, mainly related to lack of flexibility, low thermal stability and limited radiation hardness of plastic [2,3]. These drawbacks may therefore limit their future applications, especially with the advent of the flexible electronics, which is carrying with it completely flexible radiation detectors [4,5], but also for what concerns the operation in high-temperature environments and the long-term stability in extremely radiation-harsh conditions. In this context, polysiloxane elastomers offer higher flexibility, thermal stability and radiation hardness in comparison with the plastic counterpart, mainly thanks to the larger angle, length and strength of the Si-O bond in comparison with the C-C bond, and to their low glass transition temperature (T_g) [2,3]. In this framework, the first target of this thesis is the study, development and characterization of both organic and hybrid polysiloxane-based scintillation detectors for ionizing radiation.

In the first instance, several studies on polysiloxane scintillators have been reported in recent years in neutron detection, with particular focus on the capability of discriminating neutrons from the γ-ray background [6–8]. In fact, nowadays neutron detection mainly relies on the use of ^{3}He-based detectors, which are highly efficient but fragile and highly expensive. A cheaper possibility is represented by the use of large-volume liquid-based scintillation detectors, which however present serious problems related to toxicity, spillage risk and waste disposal. A valid alternative in terms of ease of processing and cost of production is therefore represented by solid scintillators. A commercial solution for fast neutron detection with optimal pulse-shape discrimination (PSD) capabilities is represented by the PVT-based EJ-299-33A (Eljen Technologies, USA). In the latter, a high amount of 2,5-diphenyloxazole (PPO) as primary dye (30 wt.%) assures the proximity of directly-ionized dye molecules, promoting therefore their triplet-triplet annihilation (TTA) and hence the PSD capabilities of the scintillator. However, the high content inside the polymer matrix of extraneous compound can potentially compromise the overall mechanical and thermal

resistance of the sample, making the long-term stability of highly PPO-loaded PVT-based scintillators still under investigation. Aiming at overcoming the limitation of this commercial PVT-based scintillator, Chapter 4 of this thesis, which is reported after a general background on radiation interactions, detection and experimental methods (Chapter 1, 2 and 3), deals with the optical analysis and with the study of the PSD capabilities of polysiloxane scintillators embedding moderate amount of PPO (2-8 wt.%). In this context, the versatile chemical structure of polysiloxanes can be exploited in order to allow for PSD although maintaining a relatively low content of primary dye. This is achieved by favouring the formation of primary dye clusters, with specific conformation to accept energy from the matrix, through Förster-type mechanism, and allowing for having T_1 states in close proximity to promote TTA. This resulted in good PSD capabilities compared with the commercial PVT-based EJ-299-33A scintillator, paving the way for flexible, robust and high thermally-resistant scintillators for fast neutron detection [9].

As regards the detection of thermal neutrons, state-of-the-art commercial scintillators are fragile and with low adaptability. For example, several sensors based on ZnS activated with Ag (ZnS:Ag) and mixed with ^{6}LiF powder are available on the market, such as EJ-426/EJ-420 (Eljen Technologies, USA) and BC-704 (Saint Gobain, France). In this context, in Chapter 5 we investigate the thermal neutron capabilities of hybrid scintillators composed of polysiloxanes matrices embedding ZnS:Ag powder and ^{6}LiF nanocrystals. According to the detection process, which exploits the ^{6}Li (n, α) ^{3}H reaction, crucial role is played by the size of the ^{6}LiF nanocrystals in the detection efficiency, since the reaction products must impinge the ZnS:Ag powder for the production of scintillation light. Therefore, the detection efficiency is investigated and optimized by tuning the crystal size through different solvent/co-solvent ratios. The role of the polysiloxane matrix is also investigated: two different siloxanes, either with pendant phenyl groups or with aliphatic groups are used, the former being intrinsically fluorescent and with higher polarizability than the latter. In the best conditions, a flexible and robust polysiloxane hybrid scintillator with thermal neutron detection efficiency reaching 90% of the commercial analogue (EJ-420) was successfully obtained [10].

The development of hybrid scintillators is of special interest not only for thermal neutron detection, but also for the detection of γ-rays and charged particles. In this context, especially for γ-rays, the general advantages of pure organic scintillators are often overwhelmed by the lack of stopping power of organic materials. The embedment of fractions of inorganic materials is therefore aimed at improving the overall scintillation yield, although maintaining the strengths of organic media. With this purpose, particular interest has been dedicated in recent years at using colloidal nanocrystals Quantum Dots (QDs) as loading elements, since they can potentially offer both high-Z sensitization and luminescence properties. In this respect, the most

promising study reported in the literature, proposed by Liu et el. [11], investigates the scintillation response of PVT-based nanocomposites with very high QD loading (up to 60 wt.%), where the nanocrystals are used as donors in the Förster resonance energy transfer mechanism, with organic dyes as acceptors. With a different approach, in Chapter 6 we investigate the possibility of using QDs as acceptors in the energy transfer process with the polysiloxane matrix acting as donor. Although evidences of nonradiative energy transfer are not observed up to 1 wt.% of QD concentration within the matrix, the optical response under proton irradiation of the samples embedding a very low amount of colloidal QDs (below 0.015 wt.%) shows an increase in the polysiloxane luminescence emission up to 8% in comparison with the undoped sample. This phenomenon is correlated with both the high-Z sensitization offered by the nanocrystals that slightly increases the specific energy loss experienced by protons, although the excitation mechanisms mainly occur within the matrix, and to the good transparency maintained by the samples loaded with very low QD concentrations [12].

The development of hybrid composites embedding QDs in radiation detection is not only important for scintillation purposes, but also for their possible application as luminescence passive dosimeters. In this respect, nowadays thermoluminescence dosimeters (TLDs) are the most common passive dosimeters used for personal radiation protection as well as for planning and monitoring the dose in cancer treatments with high-energy photons. With the growing of adrotherapies, TLDs have started to be used also in dosimetry with protons and other ions, showing however saturation effects due to the high density of ionization events along the particle track [13,14]. Moreover, TLDs do not offer flexibility, limiting their potential applications. Therefore, the development of innovative systems for post-irradiation ion dosimetry is of great importance. As already partially investigated with high-energy photons, one possibility is the exploitation of the photoluminescence (PL) degradation induced by ionizing radiation in colloidal QDs dispersed in a given medium, in order to correlate the optical change with the release dose [15–17]. In this context, in Chapter 7 we investigate the proton irradiation effects on QDs embedded in polysiloxane films, reporting the QD PL degradation with the increasing dose and therefore providing the proof-of-concept for using these flexible composites also in proton dosimetry. Moreover, we demonstrate the possibility, by means of time-resolved photoluminescence (PL) analysis, to discriminate between inner and outer defects induced by the radiation within the QD structure [18]. As further deepening, Chapter 8 is dedicated at investigating the role of the polymer matrix in the post-irradiation QD optical response. In this respect, colloidal QDs are embedded in a different matrix (polyvinyl alcohol, PVOH) and irradiated by protons at different fluences. The optical characterization of samples shows a lowering followed by an increase of the QD PL yield with the increasing irradiation fluence. This increase is ascribed to the arising of

energy transfer mechanisms between radiation-induced luminescence defects in PVOH, acting as donors, and QDs, acting as acceptors, demonstrating the important role of the matrix in the QD optical response after irradiation [19].

Chapter 1 - Radiation interactions with matter

The operation of any radiation detector depends on the way the radiation to be detected interacts and loses energy in the detector's active material. In this chapter, therefore, an overview on the interaction mechanisms of the main radiation typologies with matter will be presented. As a first general subdivision, radiation of interest can be divided into four major categories:

- Heavy charged particles;
- Electrons;
- High-energy photons (X- and γ-rays);
- Neutrons.

As a wider classification, in the previous list it should be noted that heavy charged particles and electrons are both charged radiation, while photons and neutrons are uncharged radiation [20].

1.1 Heavy charged particles

Heavy charged particles represent a category that includes all energetic ions with mass equal or greater to one atomic mass, such as protons, alpha particles, fission products, or the products of many nuclear reactions. Being charged particles, their interaction with matter mainly occurs through the Coulomb force between their positive charge and the negative charge of the orbital electrons within the absorbing material. Although interaction events of the charged particle with the nuclei of the material atoms are possible, such phenomena occur rarely and they are not significant in the response of radiation detectors. Therefore, when a charged particle enters the absorbing medium it interacts simultaneously with many electrons giving rise to ionization and excitation events, depending on the proximity of the encounter. In particularly close interactions, an electron may undergo an impulse large enough to have sufficiently kinetic energy to create, after leaving its atom, further ionization events. These energetic electrons, which represent an indirect way by which the charged particle transfers its energy to the absorbing medium, are called δ rays, and they represent the main way through which the energy of the charged particle is transferred to the material. As a result, the charged particle loses its energy continuously and its velocity decreases until the particle is stopped. Moreover, because of the difference in mass between the charged particle and the electron, the charged particle is not significantly deflected and therefore its trajectory within the absorbing material can be approximated by a straight path [20].

Under the previous phenomenological context, the *linear stopping power* S (or the *specific energy loss*) of a charged particle interacting within a given material is defined as the ratio between the differential energy loss experienced by the particle and its differential path length:

$$S = -\frac{dE}{dx} \tag{1.1}$$

More specifically, the classical expression describing the specific energy loss of a charged particle within an absorbing material is the *Bethe formula*:

$$-\frac{dE}{dx} = \frac{4\pi e^4 z^2}{m_0 v^2} NB \tag{1.2}$$

where

$$B = Z\left[ln\frac{2m_0 v^2}{I} - ln\left(1 - \frac{v^2}{c^2}\right) - \frac{v^2}{c^2}\right] \tag{1.3}$$

In the previous expressions, v and ze are the velocity and charge of the interacting particle, N and Z are the number density (atoms/cm^3) and atomic number of the absorbing material, m_0 is the electron rest mass, and e is the electron charge. The parameter I is an empirical constant representing the average excitation and ionization potential of the absorber. Therefore, the specific energy loss depends on both the charged particle and the material properties: the greater the particle charge, the higher its specific energy loss; the higher the density and atomic number of the absorbing material, the greater the linear stopping power. For nonrelativistic charged particles ($v \ll c$) only the first term in B is significant. Moreover, the expression for B varies slowly with particle energy, meaning that the specific energy loss varies as $1/v^2$. From the phenomenological point of view, this behaviour is explained considering that the particle spends more time in the proximity of an electron when its velocity is low and therefore the energy transfer increases accordingly. As a result, when the specific energy loss is plotted as a function of the penetration depth, a peak, known as *Bragg peak*, is observed at the end of the particle path (Figure 1.1). Another important parameter to define when dealing with charged particle interactions is the particle *range*, namely the mean distance travelled by the particle within the absorbing medium. For example, 2 MeV protons and alpha particles of the same energy have ranges of about 85 μm and 12 μm in polysiloxane, respectively (Figure 1.1) [20].

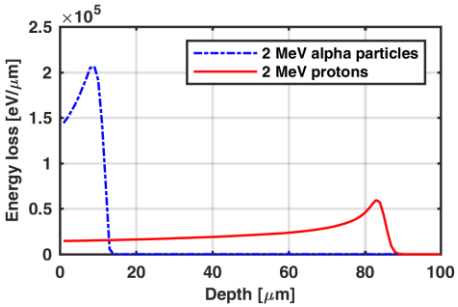

Figure 1.1: Energy loss profile of 2 MeV protons and alpha particles in polysiloxane (SRIM simulation).

1.2 Electrons

Unlike heavy charged particles, electrons lose their energy in matter at a lower rate and, since their mass is equal to the orbital electrons with which they interact, large deviations in the electron path are possible (Figure 1.2). For this reason, the concept of range is less definite for electrons than for heavy charged particles, since the total path length may be considerably greater than the distance of penetration along the initial velocity vector. The range is therefore an empirical quantity, corresponding to the thickness of absorber required to stop most of the electrons. To describe the energy loss of electrons due to ionization and excitation events an expression similar to the Bethe formula has been derived [20]. However, electrons differ from heavy charged particles also for their possibility to lose energy by radiative processes (*bremsstrahlung*), and therefore the total linear stopping power is the sum of the collisional and radiative losses:

$$\frac{dE}{dx} = \left(\frac{dE}{dx}\right)_c + \left(\frac{dE}{dx}\right)_r \tag{1.4}$$

The ratio between the specific energy losses due to radiative and collisional events is approximately given by:

$$\frac{\left(\frac{dE}{dx}\right)_c}{\left(\frac{dE}{dx}\right)_r} \approx \frac{EZ}{700} \tag{1.5}$$

where the energy is in MeV. It is possible to note that for electron energies lower than few MeV the radiative energy losses are negligible, especially if the interactions occur in low Z materials [20].

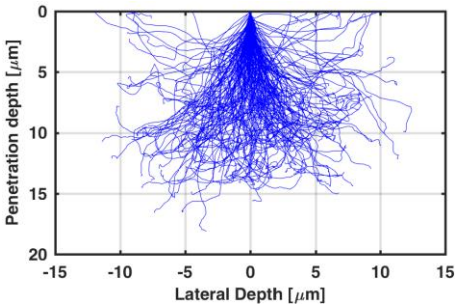

Figure 1.2: 2D path profile of 30 keV electron beam (10 nm radius) in polysiloxane (CASINO simulation).

1.3 High-energy photons

High-energy photons include X-rays emitted in the rearrangement of electron shell of atoms and γ-rays originating from transitions within the nucleus itself (radioactive decay). When X- or γ-rays interact with matter, three main mechanisms play an important role in radiation measurements: *photoelectric absorption*, *Compton scattering* and *pair production*. All these processes lead to the partial or complete transfer of the photon energy to an electron, resulting in the disappearance or scattering of the incoming photon. This single-event behaviour is in contrast with that of charged particles previously discussed, which gradually slow down through continuous interactions with many absorber atoms. If monoenergetic γ-rays hit an absorber of a given thickness *d*, the fraction of the incident particles that are absorbed, i.e. undergo one of the three previous interactions, is:

$$f = 1 - e^{-\mu d} \tag{1.6}$$

where μ is the *linear attenuation coefficient,* that is the sum of the linear attenuation coefficients corresponding to the three interactions:

$$\mu = \tau\ (photolelectric\ ) + \sigma(compton) + \ \kappa\ (pair) \tag{1.7}$$

These quantities, which represent the probability of occurrence of the relative interaction mechanism, depend on both the photon energy and the atomic number of the material (Figure 1.3) [20].

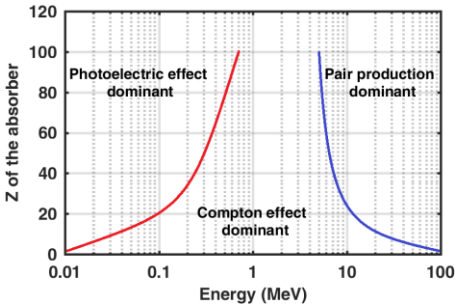

Figure 1.3: Relative importance of the three main types of γ-ray interaction. The lines show the values of Z and E for which the two close effects are equally probable [20].

As can be observed in Figure 1.3, for relatively low Z materials, like polymers, the Compton effect dominates in the energy range between few hundreds keV and few MeV. This concept is also reported in Figure 1.4 for the more specific case involving polysiloxane as absorbing material.

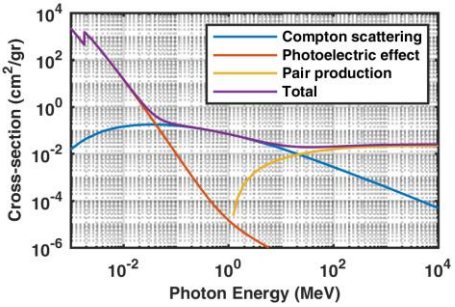

Figure 1.4: Cross-section of the three different γ-ray interactions in polysiloxane (NIST XCOM Database).

1.3.1 Photoelectric effect

In the photoelectric absorption process, a photon interacts with an atom of the absorbing material and the photon completely disappears, giving rise to the ejection by the atom of a shell electron, called *photoelectron*, and to an ionized atom. As a

result of this interaction, that occurs with the atom as a whole and cannot take place with free electrons, the photoelectron appears with an energy equal to:

$$E_{e^-} = h\nu - E_b \tag{1.8}$$

where $h\nu$ is the photon energy and E_b is the binding energy of the electron in its original shell. The probability of photoelectric absorption as a function of the photon energy and atomic number of the material is approximately given by:

$$\tau \approx \frac{Z^n}{E_\gamma^{3.5}} \tag{1.9}$$

where n varies between 4 and 5. The photoelectric process is therefore the predominant interaction mechanism of X- or γ-rays of relatively low energy and it is enhanced for absorbing materials of high atomic number Z [20].

1.3.2 Compton effect

The Compton effect occurs between an incident γ-ray photon and an electron of the atom in the absorbing material, and it is the predominant interaction mechanism for γ-ray energies typical of radioisotope sources. In this phenomenon, the incoming photon interacts with an electron (assumed at rest) and transfers part of its energy to the electron itself, which is then known as *recoil electron*. As a result of the interaction, the photon is deflected with an angle θ and energy $h\nu'$, and the recoil electron with an angle φ and energy E_{e^-}. The energy $h\nu'$ of the photon is given by:

$$h\nu' = \frac{h\nu}{1 + \frac{h\nu}{m_0 c^2}(1 - \cos\theta)} \tag{1.10}$$

where $h\nu$ is the initial incident photon energy and $m_0 c^2$ the rest-mass energy of the electron (0.511 MeV). The energy of the recoil electron will be therefore:

$$E_{e^-} = h\nu - h\nu' \tag{1.11}$$

As it is possible to notice from Equation 1.10, the energy of the scattered photon, and therefore of the recoil electron, depends on the scattering angle θ. For $\theta = 0°$ no energy is transferred. On the other hand, the maximum energy is transferred for $\theta = 180°$, which corresponds to an energy of the recoil electron given by:

$$E_{e^-max} = h\nu - \frac{h\nu}{1 + \frac{2h\nu}{m_0c^2}} \tag{1.12}$$

The angular distribution of the scattered photon depends on the energy of the incoming photon, as predicted by the *Klein-Nishina* formula [20]. When operating with radiation detectors, the dependence of the amount of transferred energy on the scattering angle explains therefore the broad and continuum nature of the Compton energy spectrum, which ends at the highest transferred energy E_{e^-max} with a sharp cutoff known as *Compton edge (*Figure 1.5*)* [20].

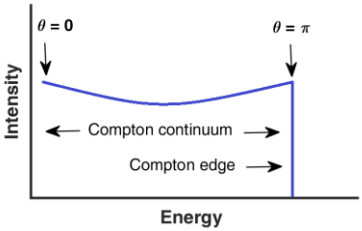

Figure 1.5: Sketch of the Compton continuum [20].

1.3.3 Pair Production

If the energy of the incoming γ-ray exceeds twice the rest mass of an electron ($2m_0c^2 = 1.02$ MeV), the pair production process becomes energetically possible, although the probability of this interaction remains very low until the photon energy approaches several MeV. In this interaction mechanism, which occurs in the coulomb field of a nucleus, the photon is completely absorbed and its energy is converted into the rest mass energy ($2m_0c^2$) and kinetic energy E_{pp} of an electron-positron pair. The total kinetic energy of the pair is:

$$E_{pp} = \mathrm{E} - 2m_0c^2 \tag{1.13}$$

where E is the initial photon energy. However, due to the high photon energy needed for a significant probability of pair production, this phenomenon is not of relevant importance in this work [20].

1.4 Neutrons

In common with photons, neutrons are uncharged particles and therefore they do not experience the Coulomb force with electrons or nuclei of the absorbing materials. Unlike the other types of radiation, neutrons easily penetrate the electron cloud and interact with the nuclei through the strong nuclear force. However, since the nuclear force is very short ranged (10^{-13} cm), neutrons have to pass close to a nucleus to give rise to an effective interaction. Because of the small size of a nucleus in relation to the atom, neutrons have therefore low probability of interaction and they can travel relatively long distances within the material. Depending on their energy, neutrons can interact with the nuclei through two main different phenomena: absorption and scattering. In absorption phenomena, the neutron is absorbed by the nucleus causing its excitation. The excited product nucleus may emit γ-rays and subsequently be stable or radioactive, or a nuclear reaction may occur with the emission of heavy charged particles. In scattering events, the neutron collides with a nucleus transferring to it a fraction of its energy. Since the relative probability of the two phenomena strongly depends on the neutron energy, different neutron classifications have been proposed according to their energy. For example, a classification divides neutron in cold, thermal, epithermal, resonance and fast, whose respective energies are reported in Table 1.1.

	Energy (eV)	Velocity (km/s)	λ (nm)
Cold	< 0.025	< 2.2	> 0.18
Thermal	$\simeq$ 0.025	$\simeq$ 2.2	$\simeq$ 0.18
Epithermal	0.025 – 1	2.2 – 13.8	0.18 – 0.03
Resonance	1 – 10^3	13.8 – 437.4	0.03 – 0.001
Fast	10^3 – 10^7	437.4 – 4.37×10^4	0.001 – 9×10^{-6}

Table 1.1: Neutron classification [21].

However, a widest classification divides neutron in *slow* (0.025 eV – 1 keV) and *fast* (1 keV – 10 MeV) neutrons, according to which their interaction properties with matter will be discussed below [1,20,21].

1.4.1 Slow neutrons

The interaction mechanism of slow neutrons with matter occurs mainly by nuclear capture reactions, since the cross section of these processes scales as $1/v$ (excluding resonance peaks, Figure 1.6), where v is the neutron velocity. In this context, the most important slow neutron interactions for neutron detection are nuclear reactions involving the emission of heavy charged particles of enough energy to be

subsequently detected, such as (n,α) and (n,p) reactions. Among them, reaction involving ^{3}He, ^{10}B and ^{6}Li nuclei are widely exploited in neutron detection because of their high interaction cross sections. For example, ^{3}He-based neutron detectors exploit the reaction:

$$^{3}_{2}He + n \rightarrow {}^{3}_{1}H\ (0.191\ MeV) + p\ (0.573\ MeV)$$

Another common reaction involves the neutron-boron interaction:

$$^{10}_{5}B + n \rightarrow \begin{cases} ^{7}_{3}Li\ (1.01\ MeV) + \alpha\ (1.78\ MeV) \\ ^{7}_{3}Li^{*}(0.84\ MeV) + \alpha\ (1.47\ MeV) \end{cases}$$

where the branching indicates that the ^{7}Li product may be either in its ground state or in its excited state. Lastly, another popular reaction for the detection of slow neutron is the (n,α) reaction in ^{6}Li:

$$^{6}_{3}Li + n \rightarrow {}^{3}_{1}H\ (2.73\ MeV) + \alpha\ (2.05\ MeV)$$

which is particularly attractive due to the high energy of its products [1,20].

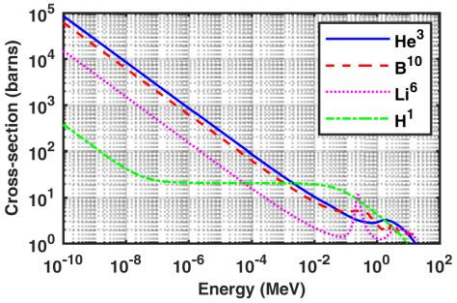

Figure 1.6: Neutron cross-sections for absorption (^{3}He, ^{10}B, ^{6}Li) and elastic scattering (^{1}H) plotted as a function of the neutron energy [1].

1.4.2 Fast neutrons

As the neutron energy increases, especially above the keV range, the neutron absorption cross section falls and the elastic scattering becomes the dominant interaction phenomenon (Figure 1.6). In this process, a neutron collides with a

nucleus, transferring part of its energy to it. The nucleus recoils with an energy given by:

$$E_r = \frac{2AE_n}{(A+1)^2}(1-\cos\alpha) \tag{1.14}$$

where A is the mass of the nucleus, E_n is the kinetic energy of the incoming neutron and α is the scattering angle of the neutron in the centre-of-mass coordinate system. As it can be noticed, the maximum energy is transferred for $\alpha = 180°$, where the nucleus recoils with an energy given by:

$$E_{r_{max}} = \frac{4AE_n}{(A+1)^2} \tag{1.15}$$

It therefore follows that for $A = 1$ (i.e. for hydrogen atoms), $E_{r_{max}} = E_n$, namely the entire neutron energy is transferred to the nucleus in a head-on collision. This explains the use of light hydrogen-rich materials to attenuate fast neutron for shielding purposes, as well as for fast neutron detection exploiting the recoil protons. In this respect, it has been demonstrated that for neutron-proton collision, over the most of the neutron energy range of interest ($E_n < 10MeV$), the scattering is isotropic, namely all the angles of recoil are equally probable in the centre-of-mass system. This means that the energy distribution of the recoil protons is uniform (a simple rectangle, Figure 1.7) extending from zero to E_n [1,20].

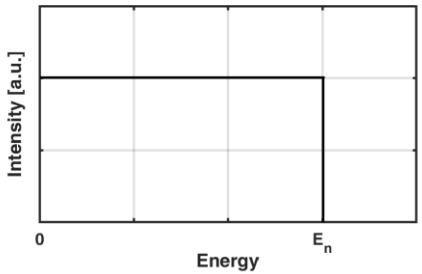

Figure 1.7: Qualitative graph representing the expected energy spectrum of recoil protons produced by neutrons with E<10 MeV impinging on hydrogen atoms [1].

1.5 Radiation flux, fluence and dose

The incident radiation *flux* is a measure of the amount of radiation received by an object, like the detector active material, from a given radiation source, and it is measured as the incident number of particles per unit time and area ($length^{-2}time^{-1}$). The radiation *fluence* is the time integral of the flux over the exposure duration. For a monodirectional beam, the fluence is simply the total incident number of particles per unit area ($length^{-2}$), where the area is perpendicular to the direction of the beam. As we have previously reported, beyond the differences in the interaction mechanisms among the various radiation types, when radiation interacts with matter releases a given amount of energy to the absorbing material. However, two different materials subjected to the same radiation treatment will in general absorb different amounts of energy. Since many important phenomena, including changes in physical properties or induced chemical reactions, scale with the energy absorbed per unit mass of the material, a unit measuring this quantity is of great interest in radiation protection as well as in radiation detection in certain cases. The energy absorbed from any type of radiation per unit mass of the absorbing material is defined as the *absorbed dose*, whose physical unit is *Gray* (Gy), where 1 Gy = 1Joule/1 Kg [20].

Chapter 2 - Radiation detection with scintillators and dosimeters

As a general wide classification, it is possible to divide the different types of radiation detectors into three broad groups:

- Counters: devices that detect individual ionizing particles, record them in the form of electrical pulses which are subsequently counted by electronic circuits. Different detectors belong to this group: gas ionization and proportional counters, Geiger-Müller counters, liquid and solid ionization counters, Cerenkov counters and scintillation counters.
- Dosimeters: devices that measure the integrated effects of several ionizing events and therefore do not record individual particles. Depending on the dosimeter, the output signal is not necessarily electric but it can be also an optical signal.
- Track visualization instruments: devices that record the trajectories of individual ionizing particles through a medium [1].

2.1 Radiation detection with scintillators

Among the detector counters, scintillation detectors offer the highest versatility in terms of operating modes, variety of detectable radiation types and energy range. In this context, a scintillation detector is a device based on a material, called *scintillator*, that converts the ionization and excitation events generated by the interacting high-energy particle into a visible light pulse, through the process of *luminescence*. The light is subsequently detected by a coupled photodetector, like a photomultiplier tube (PMT) (Figure 2.1), which converts the scintillation pulse into an electric pulse. The ideal scintillator should have the following properties:

- High scintillation efficiency, that is the fraction of the incident particle energy that is converted into visible light;
- Linearity between particle energy and light yield in a range as wide as possible;
- High transparency to the wavelength of its emission;
- Short decay time;
- Emission wavelength as close as possible to the wavelength of maximum sensitivity of the coupled photodetector;
- Manufacturability in different sizes;
- Refractive index as close as possible to that of photodetector window ($n \approx 1.5$);

- Low toxicity;
- Low cost;
- Particle discrimination.

Since no material possesses all the previous features together, different scintillators exist with their strengths and limitations. As a wide general classification, depending on their primary material, scintillators can be divided into inorganic and organic scintillators [1,20].

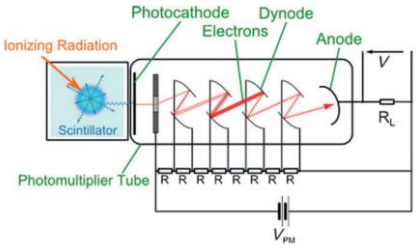

Figure 2.1: Schematic drawing representing a scintillator coupled with a PMT [22].

2.1.1 Inorganic scintillators

The scintillation process in inorganic materials depends on the energy states resulting from the crystalline properties of the material. Considering the energy band structure (Figure 2.2), when radiation interacts with an inorganic scintillator creates electron-hole pairs. Since for several reasons in a pure crystal the deexcitation process resulting in the emission of photons would be inefficient, inorganic scintillators are doped with impurities, called *activators*, which introduce energy states within the forbidden gap, favouring the deexcitation mechanism and the subsequent luminescence with the emission of visible photons.

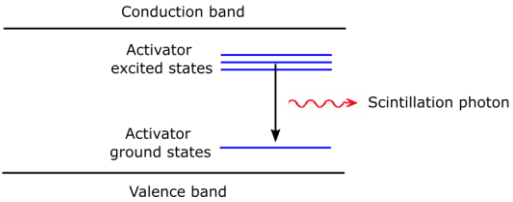

Figure 2.2: Schematic energy band structure of an activated inorganic crystalline scintillator [20].

The most common inorganic scintillators are alkali halide crystals doped with a given activator, such as NaI(Tl), CsI(Tl), CsI(Na) and LiI(Eu). Among the previous ones, due to its excellent light yield sodium iodide activated with thallium is the reference standard inorganic scintillation material for γ-ray spectroscopy. LiI(Eu)-based scintillators are of special interest in neutron detection since the $^{6}Li(n,\alpha)$ reaction can be exploited. In general, scintillators based on alkali halides offer a high light output, a good linearity, a high stopping power and a good radiation hardness. On the other hand, they have a long decay time (from few hundred ns to few μs) and they are hygroscopic, delicate and difficult to grow in large sizes. Among the many other inorganic scintillation materials, it is worth mentioning the barium fluoride BaF_2, that is the only inorganic scintillator having a decay time less than 1 ns, although its light yield is about 20% of NaI(Tl). Lastly, another inorganic scintillation material is the silver-activated zinc sulfide ZnS(Ag): it has a scintillation efficiency comparable to that of NaI(Tl), although it is available only as a polycrystalline powder. As a result, it is used only in certain applications, for example in thin screens for the detection of alpha particles and other heavy ions in hybrid scintillators [1,20].

2.1.2 Organic scintillators

Unlike inorganic scintillators, the luminescence process in organic scintillators arises from transitions in the energy level structure of a single molecule and therefore it is independent of the material physical state. In fact, the emission of light is the result of excitation-deexcitation mechanisms of electrons belonging to the aromatic groups, which play a fundamental role in any organic scintillator. The main advantages of organic scintillators are they short decay time (few ns), the possibility to be produced in large sizes with limited costs and the high hydrogen content, which makes them suitable for the detection of fast neutrons. On the other hand, in comparison with the inorganic counterpart, organic scintillators have a lower light yield and a lower radiation hardness. As a general classification, organic scintillators can be mainly divided in:

- pure organic crystals;
- liquid organic solutions;
- solid organic scintillators.

Scintillators of pure organic crystals, like anthracene, are the oldest organic scintillators and they have the highest scintillation efficiency of any organic scintillator, although being fragile and difficult to obtain in large sizes. Liquid organic scintillators, obtained by dissolving an organic scintillator in an appropriate solvent, are suitable for large sizes applications with limited costs and, since they do not present a solid structure, they have the highest radiation hardness among the organic scintillators.

However, their main drawbacks are related with the toxicity of certain solvents and with their high sensitivity to dissolved oxygen, which acts as luminescence quencher. As regard solid organic scintillators, since they are particularly important for this work they are presented more in detail in the following subsections [1,20].

2.1.2.1 Introduction to solid organic scintillators

Solid organic scintillators are obtained through the polymerization of an aromatic polymer initially in liquid form. Depending on the specific case, before its polymerization one or two organic dyes may be added in appropriate weight percentages to the solution. The addition of these dyes, which are characterized by a higher probability of radiative emission than the matrix molecules, has the aim to efficiently activate the scintillation process in the system and to shift the light emission to longer wavelengths, in order to reduce self-absorption and improve the spectral matching with the sensitivity of the coupled photodetector. At present, the most common matrices used in commercial solid organic scintillators are aromatic plastic compounds like polyvinyltoluene (PVT) and polystyrene (PS) (Figure 2.3). Other less common scintillation matrices are polyepoxydes, polyesters and polyimides. In recent years, polysiloxanes have started to be widely investigated in scintillation. Although sometimes classified as plastic scintillators, polysiloxanes differ from traditional plastic materials as they are elastomers, commonly known as silicon rubbers (silicones). Unlike plastic, polysiloxanes offer a higher degree of flexibility as well as a higher temperature stability and radiation tolerance.
In general, the main common advantage of solid organic scintillators is their possibility to be shaped differently (in rods, cylinders, flat sheets) and in various sizes. Moreover, being the material relatively inexpensive, plastics are at present the only practical choice if large-volume solid scintillators are needed [22,23].

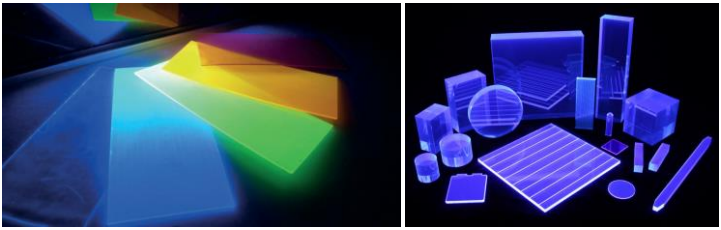

Figure 2.3: Polystyrene scintillators displaying different emission wavelength (left) [22] and polyvinyltoluene scintillators shaped differently (right) [24] under UV excitation.

Since plastic scintillators are completely organic compounds, they have a relatively low atomic number which makes them suitable for the detection of certain radiation

types such as beta particles, alpha particles and fast neutrons, the latter through the proton recoil process. However, for the detection of other radiation such as slow neutrons and high-energy photons, plastic scintillators suffer of intrinsic limitations. In fact, as reported in the first chapter, for the detection of slow neutron nuclear reactions involving neutron-sensitive elements (like B or Li) needs to be exploited. Moreover, due to their low Z plastic scintillators do not present a significant photoelectric cross section for γ-rays of typical energies, showing therefore no photopeak and only a Compton continuum in their spectrum. Therefore, with the aim of improving the detection performances of these scintillators to slow neutron and γ-rays, modifications of solid organic scintillators through the embedment of inorganic material have been reported, representing still nowadays an open research topic. Since these scintillators are not completely made of organic materials, they are usually referred to as either *hybrid* or *loaded* plastic scintillators [22,23].

2.1.3 Working principles of solid organic scintillators

When a high-energy particle interacts with a plastic scintillator, a fraction of its energy is released through ionization and excitation events mainly involving the scintillator matrix. The resulting excitations are subsequently partially transferred to the primary dyes and eventually to the secondary dyes (wavelength shifter), which are the responsible of the final light emission through the process of luminescence. Although occurring in few nanoseconds, the overall process is therefore composed of different steps (Figure 2.4), which will be deepen separately in the following subsections [23].

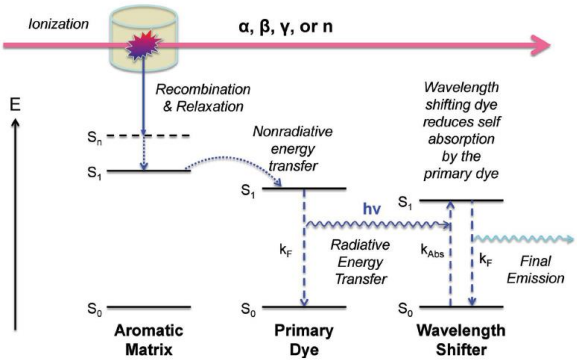

Figure 2.4: Schematic drawing of the main processes involved in the scintillation of organic materials [23].

2.1.3.1 Luminescence of organic molecules

The luminescence is the capability of a substance to emit light after its proper excitation. Since the nature of this excitation can be different, several luminescence phenomena exist depending on the excitation process. For example, luminescence can be induced by absorption of light (photoluminescence, PL), ionizing radiation (scintillation), chemical processes (chemioluminescence), biochemical processes (bioluminescence), the presence of an electric field (electroluminescence) and others phenomena [25,26].

Although in scintillation the excitation mechanism is slightly different and more complex, the luminescence process is hereafter explained in first approximation considering the PL case. The excitation process under ionizing radiation will be therefore deepen subsequently.

The mechanism of light absorption and emission is represented by the Jablonski diagram, reported in Figure 2.5. First of all, luminescence occurs from deexcitation phenomena of electronically excited states and it typically arises, in organic materials, from aromatic molecules (fluorophores). In these molecules, the presence of unsaturated bonds (with sp or sp^2 hybridization) allows for the electrons to occupy π orbitals: if several π orbitals are present next to each other, a delocalized system is formed and its excited state is responsible for luminescence (π-π* transitions). Considering Figure 2.5, the singlet ground, first, and second electronic states are depicted by S_0, S_1, and S_2, respectively. At each of these electronic energy levels the fluorophores can exist in a given number of vibrational energy levels, depicted by 0, 1, 2, etc. The transitions between electronic states are often referred as vertical transitions since they are much faster than the possible displacement of nuclei (*Frank-Condon* principle). The first mechanism involved in PL is the light absorption (occurring in 10^{-15} s), resulting with the fluorophore in a given vibrational level of either S_1 or S_2. At this point, the molecule rapidly relaxes to the lowest vibrational level of S_1 through the process of internal conversion *(*occurring in 10^{-12} s). The excited state involving the molecule in the lowest vibrational level of S_1 typically lasts few nanoseconds (10^{-8} -10^{-9} s). For this reason, internal conversion is generally complete before the emission, the latter resulting from a thermally equilibrated excited state. Return to the ground state typically occurs towards a higher excited vibrational ground state, which then quickly (10^{-12} s) reaches thermal equilibrium. Because of energy losses due to thermalization, the final result is that the emitted *fluorescence* photon has a lower energy than the excitation photon. This difference in energy is called *Stokes shift*. An interesting consequence of the decay to higher vibrational ground states is that the emission spectrum is typically a mirror image of the absorption spectrum of the $S_0 \rightarrow S_1$ transition. This similarity occurs because of the Frank-Condon principle, since electronic transitions do not significantly alter the nuclear geometry. Therefore, the

spacing of the vibrational energy levels of the excited states is similar to that of the ground state [25,26].

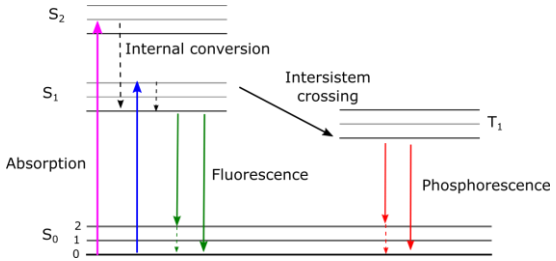

Figure 2.5: Jablonski diagram [26].

Molecules in the S_1 state can also undergo a spin conversion to the first triplet state T_1. Emission from T_1 is called *phosphorescence*, and is generally shifted to longer wavelengths (lower energy) relative to the fluorescence. Conversion of S_1 to T_1 is called *intersystem crossing*. Transition from T_1 to the singlet ground state is forbidden, and as a result the lifetime of triplet excited state is several orders of magnitude larger (from 10^{-6} to 1 s) than that of fluorescence. For these reasons, phosphorescence is not a relevant process in scintillation.

Important parameters for characterizing an organic fluorophore are the *fluorescence quantum yield* (Φ_F) and *fluorescence lifetime* (τ). The fluorescence quantum yield is defined as the ratio of the number of photons emitted to the number of photons absorbed. The fluorescence lifetime is defined as the average time the molecule spends in the excited state before returning to the ground state. Since fluorescence emission is a random process, fluorescence lifetime can be obtained by the time-resolved decay of the intensity of the light emitted by the fluorophore, which typically follows an exponential function:

$$I(t) = I_0 e^{-\frac{t}{\tau}} \tag{2.1}$$

where the lifetime τ represents therefore the time for which the intensity is decreased by 63%. Moreover, it is worth mentioning that the fluorescence emission can be multiexponential, especially if delayed fluorescence phenomena occur. In this case the time evolution of the intensity is modeled with the sum of two or more exponentials:

$$I(t) = I_{0_1} e^{-\frac{t}{\tau_1}} + I_{0_2} e^{-\frac{t}{\tau_2}} + \cdots \tag{2.2}$$

2.1.3.2 Energy transfer

After reaching a first excited state, either S_1 or T_1, in the presence of a primary dye the matrix molecule can, in certain conditions, return to the ground state by transferring the energy to the primary dye through *non-radiative energy transfer* processes. Unlike *radiative energy transfer*, non-radiative processes do not involve the emission and reabsorption of photons and therefore they occur faster and more efficiently than the radiative one. In general, energy transfer processes occurs between a donor (D) molecule in the excited state and an acceptor (A) molecule in the ground state, and they can only occur if the emission spectrum of the donor overlaps the absorption spectrum of the acceptor (Figure 2.6) [25,26].

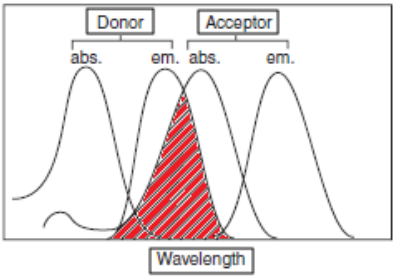

Figure 2.6: Example of spectrum overlap between the emission spectrum of the donor and the absorption spectrum of the acceptor [25].

Depending on the type of interactions between the donor and acceptor, different non-radiative energy transfer phenomena can occur. In fact, the interactions may be Coulombic and/or due to intermolecular orbital overlap. The Coulombic interactions rely on long-range dipole-dipole interactions (Förster 's mechanism) and short-range multipolar interactions. On the other hand, the interactions due to intermolecular orbital overlap foresee both electron exchange (Dexter mechanism) and charge resonance interactions, which are only short-range interactions (< 1 nm). It is worth precising that for non-radiative energy transfer involving single states, all types of interactions are involved, whereas triplet-triplet energy transfer is due to only orbital overlap (Figure 2.7) [25,26].

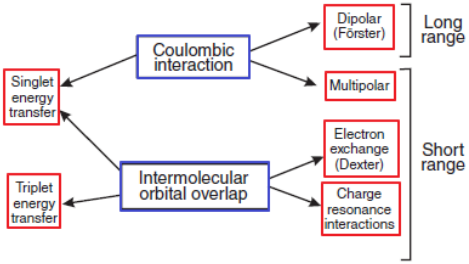

Figure 2.7: Types of interactions involved in nonradiative energy transfer mechanisms [25].

In solid organic scintillators, under regular conditions, Förster resonance energy transfer (FRET) can be considered the main nonradiative process through which the excitations are transferred to the primary dye from the excited states of the polymer matrix, and therefore only the S_1 are transferred to the primary dye, determining a scintillation efficiency usually around 3-4% [27].
The rate of Förster energy transfer k_τ (r) from a donor to an acceptor molecule is given by:

$$k_\tau(r) = \frac{1}{\tau_D}\left(\frac{R_0}{r}\right)^6 \tag{2.3}$$

where τ_D is the lifetime of the donor in the absence of acceptor, R_0 is the Förster distance, and r is the donor-to-acceptor distance. As it can be observed, the rate of FRET depends strongly on distance, since it is proportional to r^{-6}. The Förster distance R_0 (Figure 2.8), which represents the donor-acceptor separation for which the process is 50% efficient (generally in the range 1-8 nm), is given by:

$$R_0 = \frac{9000(ln10)\kappa^2\Phi_D}{128\pi^5 N_A n^4}\int_0^\infty I_D(\lambda)\varepsilon_A(\lambda)\lambda^4 d\lambda \tag{2.4}$$

where κ^2 is an orientation factor between the donor and acceptor, equal to 2/3 for randomly distributed freely rotating molecules and to 0.476 for rigid media where the molecules rotation is slower than the deexcitation rate. N_A is the Avogadro's number, n is the refractive index of the medium and Φ_D is the donor quantum yield. The last term is the overlap integral, where I_D is the wavelength dependent donor emission spectrum normalized to an area of 1, ε_A is the extinction coefficient spectrum of the acceptor and λ is the wavelength in nm. In general, from Equation 2.4 follows that a

large spectral overlap and a high donor efficiency translate into larger values of the Förster distance and therefore to higher nonradiative energy transfer rate.

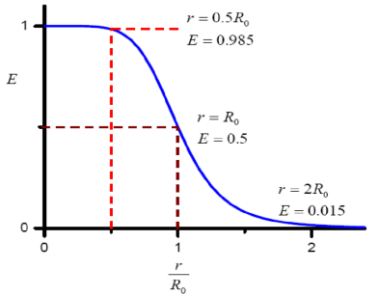

Figure 2.8: Energy transfer efficiency as a function of the ratio r/R_0 [25].

Moreover, since the energy transfer rate is inversely proportional to the sixth power of the intermolecular distance (Equation 2.3), the efficiency of the process increases with the concentrations. For this reason, in order to ensure complete and efficient transfer of the excitation energy, primary dye loadings in organic scintillators are typically in the range of 1-5 wt.%. However, with most of the dyes this percentage result in significant loss of the emitted photons due to self-absorption. To mitigate these losses, a secondary, wavelength shifting dye is added, with much lower loading content (0.005-0.5 wt.%). However, at this lower concentration the average intermolecular distance between the two dyes does not usually allow for a high efficiency of nonradiative energy transfer and therefore the process usually occurs by radiative energy transfer, as also indicated in Figure 2.4 [25,26].

2.1.3.3 Pulse shape discrimination

The pulse shape discrimination (PSD) is the capability of a radiation detection system to discriminate different particles. In order to understand the principle, the excitation mechanisms induced by ionizing radiation in organic media need to be deepen.
Neglecting the presence of a secondary dye due to its low concentration, when a high-energy particle interacts with an organic solid scintillator the main effect is the formation of ionized molecules of both matrix and primary dye, which subsequently recombine, through a process known as *ion recombination*, with scattered electrons to form excited states. Due to spin statistics, 25% of the excited states resulting from ion recombination will be singlet states (S_n), while the remaining 75% will be triplet states (T_n). It is also possible that the passage of the high-energy particle (or its δ-rays) may result in direct excitation from the ground state to S_n states, a process that

would not result in the formation of T_n states. Moreover, because of the high density of excited states along the particle track, bimolecular reaction of higher excited states can occur, in a process known as ionization quenching. Ionization quenching (or Birks' quenching) is a very fast process, which will directly compete with internal conversion for relaxation of the S_n and T_n states to their lower first-excited state levels, S_1 and T_1, respectively (internal conversion and ionization quenching are acting in the same time scale, approximately 10^{-11} s). Although not yet properly understood, important processes in ionization quenching should include:

$$S_n + S_m \rightarrow S_0 + [I^+ + e^-]$$

$$S_n \xrightarrow{E_{field}} I^+ + e^-$$

where E_{field} is the electric field due to the presence of nearby ionized molecules. The magnitude of the ionization quenching will depend on the ionization density, which in turn depends on the specific energy loss dE/dx of the high-energy particle. This explain the reason, for example, for the lower scintillation light yield of alpha particles in comparison with electrons of the same energy. The T_n states formed from ion recombination will be less susceptible to ionization quenching, due to the slower nature of the ion recombination process. The various factors will combine with the result that the final populations of S_1 and T_1 states will deviate from the 3:1 ratio derived only from spin statistics, and the precise ratio will be determined by the specific energy loss of the particle. As regard the matrix molecules in the S_1 and T_1 states, the S_1 states are then Förster-transferred to the primary dyes. On the other hand, as already mentioned, the matrix molecules in T_1 states are not involved, under regular conditions, in nonradiative energy transfer with the primary dyes and therefore they will relax via other nonradiative pathways. As regard the primary dye molecules, some of them will be therefore into an excited S_1 state, as a result of the transferred energy from the matrix molecules. Some other primary dye molecules, however, will be into a T_1 state, as a result of ion recombination phenomena of directly-ionized primary dye molecules with electrons. These dye molecules into a T_1 state will be denser along the high-energy particle track and if close enough (~1 nm) can give rise to bimolecular annihilation of T_1 states (i.e., triplet–triplet annihilation (TTA)), producing additional S_1 states according to the following scheme:

$$T_1 + T_1 \rightarrow S_0 + S_1$$

From spin statistics, generation of an overall singlet state (S_0 + S_1) from the combination of two T_1 states will occur only 1/9th of the time, and other possible combinations will lead simply to quenching of the triplet states. We precise that the

TTA mechanism can be easily favoured in liquid media by diffusion phenomena, but in rigid media the dye molecules need to be close enough to promote it [9,23].
As a result of the previous processes, the final scintillation light will be characterized by a *prompt fluorescence* and a *delayed fluorescence*. The prompt fluorescence will be the result of single state deexcitations of dye molecules occurring in regions of low ionization density, where the ionization quenching does not significantly affect the internal conversion process from S_n to S_1 of the matrix molecules before transferring their energy to the primary dye. On the other hand, the delayed fluorescence will be the result of S_1 state deexcitations occurring after TTA between dye molecules in T_1 states. In fact, since the excited single states coming from TTA form later, their emission occur at longer time, giving rise to a slower component in the emission. Moreover, since the T_n states are mainly formed by ion recombination, which is a slower process than ionization quenching, the delayed fluorescence is less affected by the ionization quenching. For this reason, it follows that the relative intensity of the delayed fluorescence in comparison with the prompt one will increase with the density of the ionized states, therefore depending on dE/dx. This phenomenon is therefore at the basis of the PSD technique, where the difference in the time-resolved scintillation pulse is used to distinguish between different particles (Figure 2.9) [9,23].

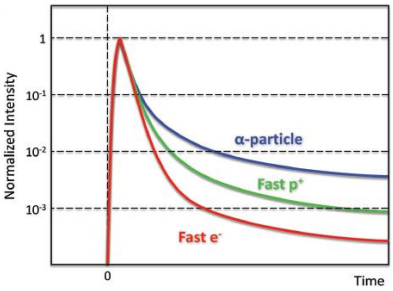

Figure 2.9: Normalized time-resolved scintillation pulses for particles having different specific energy loss [1,23].

An important equation describing the relationship between the intensity of the scintillation light emitted per unit length (dL/dx) and the specific energy loss is:

$$\frac{dL}{dx} = \frac{S\frac{dE}{dx}}{1 + kB\frac{dE}{dx}} \tag{2.1}$$

where S is the scintillation efficiency, $B\frac{dE}{dx}$ is the density of ionized species and k is the ionization quenching parameter [1].

2.1.4 Overview on hybrid solid scintillators

Hybrid scintillators have been developed with the aim to merge the advantages of organic materials with those of inorganics. Depending on the functionality of the inorganic doping material, two main categories can be identified. The first category foresees the use of inorganic doping materials in order to increase the scintillation yield under ionizing radiation, with particular focus on high-energy photons. The second category includes the use of inorganic doping materials in order to exploit nuclear reactions for the detection of slow neutrons. Further distinctions can be made depending on the type of sensitization material. In fact, first attempts to develop hybrid plastic scintillators were made by using organometallic compounds [28–31]. In the past two decades, however, significant advances in the development of nanostructured materials have been reported, and therefore an increasing interest has been dedicated at studying nanocomposite-based scintillators. In this context, nanoparticles tend to have higher thermal and air stabilities than the organometallic compounds. In addition, the different optoelectronic properties of various nanocrystals provide new opportunities for potentially improving the scintillation performance. Since the use of nanocrystals in organic solid scintillators is a topic of interest for this work, a brief overview on recent advances about hybrid scintillators is presented hereafter.

2.1.4.1 Sensitization for high-energy photons

According to the several studies reported in the literature, the sensitization of polymer-based solid scintillators by nanostructured materials can be divided in three groups:

- sensitization with nanosized traditional scintillation materials;
- sensitization with nonemitting large-band-gap nanoparticles;
- sensitization with inorganic Quantum Dots (QDs).

The first group of studies on nanocomposite scintillators reports the use of nanosized traditional scintillation materials as both the high-Z and emitting components, where polymers mainly act as a binder for structural integrity. In this context, the studies reported in the literature mainly involve the use of nanophosphors. Among a number of compounds such as Y_2SiO_5:Ln [32], $LuPO_4$:Ln [33], HfO_2:Ln [34] and GdOf:Ce [35], Ce-doped fluorides such as BaF_2 and LaF_3 were widely investigated due to their similar refractive indices with some organic matrices, deep blue emission, relatively short PL lifetimes (around 30 ns), and ease of synthesis [36,37]. However, the main problem

often reported is related with the aggregation of nanoparticles that causes the nanocomposite to be translucent at thicknesses of only few mm, often limiting the nanoparticle loading to few wt.%. Moreover, it has been shown that a significant portion of energy is deposited in the polymer matrix when the nanoparticle loading is limited [38]. As a result, even though a fluorescent matrix is used, without proper energy transfer to the luminescent nanoparticles this fraction of released energy cannot be effectively exploited to produce photons, therefore resulting in relatively low light yields [23].

The second set of research on nanocomposite scintillators relies on the use of nonemitting large-band-gap nanoparticles. In fact, nanosized traditional scintillation materials often suffer from long emission decay lifetimes because of their inherent trap-mediated emission mechanism. Obviously, to exploit the short scintillation lifetimes of organics and make use of the part of energy released in the plastics, fluorescent matrices need to be used. A fundamental prerequisite of this nanocomposite system is that the emission from plastics must not be absorbed or quenched by the inorganic nanomaterial. For this reason, the inorganic nanoparticles initially used for this purpose have very large band gaps (E_g > 4.2 eV, which is PVT's band gap) to eliminate photon absorption and exciton migration from the organics. In this system, the inorganic nanoparticles have the aim to favour the conversion of the high-energy photons into photoelectrons, while the exciton generation and photon emission processes are carried out in the organic matrix (Figure 2.10). For this nanocomposite scintillation systems, heavy metal oxide and fluorides are often chosen as the high-Z sensitizer due to: (1) their feasibility of satisfying the band gap requirement, (2) ease of synthesis, and (3) their relatively high chemical stability and low hygroscopicity. Among the several studies reported in the literature, an initial investigation was made by Cai et al. [39] using Gd_2O_3 nanoparticles dispersed in a PVT matrix loaded with a green fluorescent dye, 4,7-bis-{2'-9',9'- bis[(2"-ethylhexyl)-fluorenyl]}-2,1,3-benzothiadiazole (FBtF), emitting at 517 nm. The Gd_2O_3 nanoparticles were surface modified with methacrylate groups for covalently bonding to the growing polymer chain. As a result, subsequent in situ polymerization of the VT monomer solution containing such nanoparticles produced highly transparent nanocomposite monoliths with net Gd_2O_3 loading up to 20 wt.%. The decreasing band gaps of Gd_2O_3 (5.2 eV), PVT (4.2 eV), and FBtF (2.6 eV), in addition to the good spectral match between PVT and FBtF ensured an efficient unidirectional energy transfer from matrix to dye with little quenching by the nanoparticles. The high loading of Gd_2O_3 significantly improved the photoelectric cross-section of the plastics, and a 662 keV γ photopeak with 11.4% resolution was successfully detected using the nanocomposite [23].

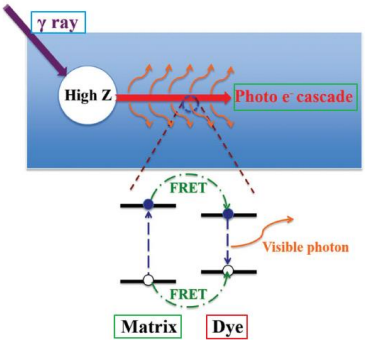

Figure 2.10: Gamma scintillation mechanism in a nanocomposite monolith loaded with high-Z nanoparticles [23].

The third set of research on nanocomposite scintillators is related with the sensitization through inorganic QDs. Since this represents an important topic for this thesis, it will be discussed more in detail in subsection 2.1.5 [23].

2.1.4.2 Sensitization for thermal neutron detection

Organic plastic scintillators are mainly composed by hydrogen and carbon atoms and for this reason they are able to detect fast neutrons, exploiting recoil protons, reporting in some cases also pulse shape discrimination capabilities [9,40,41]. However, as already mentioned, for the detection of slow neutrons a nuclear reaction needs to be exploited. For this reason, organic scintillators loaded with elements having a high cross section for slow neutrons have been developed over the past years. In fact, different types of plastic scintillators doped with organometallic boron complexes are present on the market, having concentration of boron up to 10% (e.g. BC-454 and EJ-254). At present, boron is widely used because of the high natural abundance of ^{10}B, which does not require enrichment, representing therefore a relatively inexpensive solution. Moreover, it is also a well-known and documented element, and the high cross-section leads to good efficiencies. On the other hand, the energy released by the reaction products is lower than other possible elements. For example, lithium has the advantage of higher energy of products generated during the neutron capture reaction, potentially increasing the scintillation light yield [42]. From the chemical point of view, lithium compounds are easier to produce, although the hygroscopicity of most Li compounds and the lower cross-section limit the diffusion of this element. In general, the main advantage of organic scintillator loaded with organometallic for thermal neutron detection is represented by their fast response, which is in some cases orders of magnitude higher than other systems. On the other hand, their performances in

terms of efficiency and scintillation light output are lower than inorganic scintillators, which still remain the most common scintillating systems for thermal neutron detection. In this context, the most used element is by far ^{6}Li, in the forms of ^{6}Li-glass(Ce), ^{6}LiI(Eu) and ZnS/^{6}LiF crystals, with the latter presenting the highest light output. Commercial examples of ZnS/^{6}LiF-based scintillators are EJ-426/EJ-420 and BC-704, which however present problems due to fragility and low adaptability. As a result, scintillators based on polysiloxanes and loaded with ^{6}Li-based crystals in different forms are under investigation [10,43].

2.1.5 Quantum dots in scintillators

Semiconductor QDs are a class of small-sized nanocrystals (1-10 nm diameter) displaying quantum confinement effects [44–46]. Their outstanding optical properties such as PL emission tunable over the whole visible spectral range (Figure 2.11), narrow emission (FWHM around 20–30 nm), fast PL decay lifetime (10s of nanoseconds), high PL quantum yield (up to unity) make them an attractive candidate as luminescence emitters in hybrid scintillation, with the possibility to replace the nonemitting nanocrystals previously discussed.

Figure 2.11: Colloidal QDs of different sizes under UV excitation.

As reported in subsection 2.1.4.1, plastic scintillators embedding nonemitting nanoparticles have a significantly improved Z and much shorter emission lifetime (several nanoseconds) in comparison with plastic scintillators embedding traditional scintillating materials. However, one drawback of the system is that the light yield of nanocomposite decreases proportionally with the addition of nonemitting nanoparticles, since the energy deposited in these nanoparticles cannot be efficiently transferred and converted into visible photons due to their extremely low PL quantum efficiency. For this reason, semiconductor QDs are promising candidate for increasing both the average Z of the nanocomposite and the overall light yield of the system. However, initial attempts made over the last decade mainly focused on the use of QDs like the nanosized scintillation materials discussed in subsection 2.1.4.1, where no other dyes were used for energy transfer from the QDs. For example, Létant and Wang [47,48] embedded CdSe/ZnS core/shell QDs into porous glass and tested the

nanocomposite for the detection of both alpha and gamma rays. In another study, Kang et al. [49] reported the production of CdTe/poly(vinyl alcohol) and CdTe/poly(methyl mathacrylate) nanocomposites for X-ray scintillation and imaging applications. Lastly, Lawrence et al. [50] reported the fabrication of CdTe/PVA thin film and CdSe/ ZnS core/shell QD/polystyrene nanocomposites for alpha scintillation and X-ray imaging. In general, these attempts of QD-based nanocomposites scintillators were not very successful in producing a clear, distinct photopeak. The major reason behind this is the low effective Z of these nanocomposites due to the limited loading of QDs (<5 wt.% to prevent aggregation). In addition, another problem of using QDs is their significant self-absorption due to small Stokes shift, which can easily decrease the light yield when both QD loading and nanocomposite thickness are increased. A possible way of resolving the self-absorption issue is to add a secondary organic luminescent dye as FRET acceptor for the QDs. In 2006, Campbell and Crone [51] proposed the mixing of CdSe/ZnSe core/shell QDs with a conjugated polymer, poly[2-methoxy-5-(2'-ethylhexyloxy)-p-phenylene vinylene] (MEH-PPV), as a nanocomposite scintillator, where MEH-PPV acts as both the matrix and FRET acceptor of the QDs. Scintillation (cathodoluminescence) intensity of the nanocomposite increased by 100% as the QD loading is increased to 15 vol.%, but then decreased to 50% as the QD loading is further increased to 21 vol.%. The improved scintillation intensity was ascribed to the lower ionization energy (i.e., more excitons generated per unit energy deposited of QDs, whereas the final intensity drop was correlated to an impaired FRET efficiency due to the aggregation of QDs [51].

By making a major step forward, the highest-impact study so far reported in the literature about QD-based nanocomposite scintillators was recently proposed by Liu et al. [11], reporting a transparent polymer/QD/dye ternary system. In this study, PVT, $Cd_xZn_{1-x}S$/ZnS core/shell QDs (CZS QDs), and FBtF were used as matrix, QD, and dye, respectively, as their good spectral overlaps promise an energy transfer process as depicted in Figure 2.12(a). With a partial methacrylate functionalization in situ polymerization process, the CZS QDs can be embedded at up to 60 wt.% in a 2 mm thick nanocomposite without significant transparency loss (Figure 2.12(b)). Due to the higher Z and the efficient extraction of QD-bound exciton, the light yield of the ternary nanocomposite was found to increase with the addition of QDs (Figure 2.12(c)). In addition, the efficient FRET to the FBtF dyes allows for preserving the short luminescence decay lifetime (7 ns for FBtF) typical of plastic scintillators in these nanocomposites. In summary, the authors reported the detection of a 662 keV photopeak with 9.8% resolution using the 60 wt.% CZS QD nanocomposite scintillator, demonstrating the great potential of using QD-based nanocomposite scintillators for gamma detection [11].

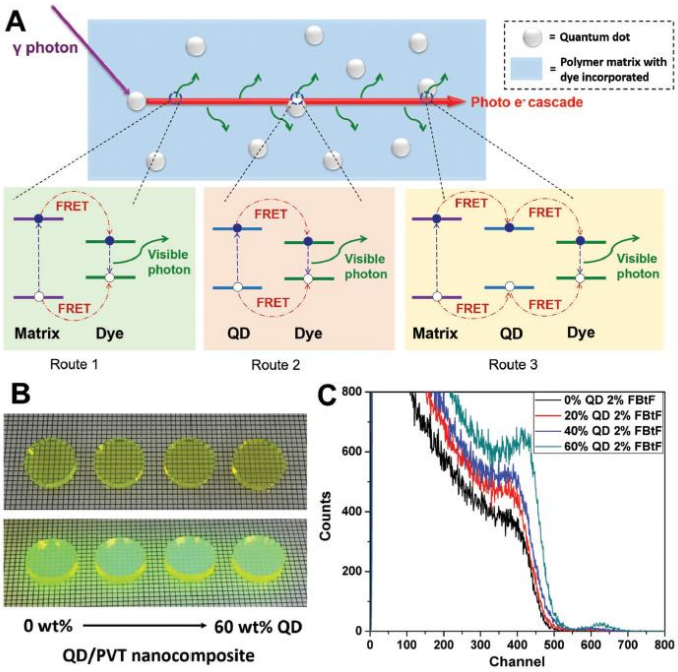

Figure 2.12: a) Schematic representation of the scintillation mechanism in a polymer/QD/dye ternary system; b) pictures of QD/PVT/FBtF nanocomposites without (upper) and with (lower) UV illumination; c) pulse height spectra of PVT-based samples with fixed amount of FBtF (2 wt.%) and different QD concentration (0-60 wt.%) [23].

2.2 Radiation detection with dosimeters

A radiation dosimeter is a device that measures, either directly or indirectly, quantities such as exposure, absorbed dose or equivalent dose, or their time derivatives (rates), or other related quantities. Therefore, unlike counters, dosimeters measure the integrated effect of several ionization events. Important properties of a dosimetry system are:

- High accuracy and precision.
- Linearity of signal with dose over a wide range: ideally, the dosimeter response should be linearly proportional to the dosimetric quantity. However, beyond a given dose a non-linearity always sets in. The linearity range and the non-linearity behaviour depend on the type of dosimeter and its physical characteristics (Figure 2.13).

- Small dose rate dependence: ideally, the response of a dosimetry system at different dose rates should remain constant. In reality, the dose rate may affect the dosimeter readings and appropriate corrections may be needed.
- Low directional dependence: the response of a dosimeter with the angle of incidence of radiation usually varies, due to its constructional details and physical size.
- Low energy dependence: ideally, the energy response should be flat. In reality, dosimeters are calibrated at a specified radiation energy and used over a much wide energy range, therefore the variation of the response requires correction.
- High spatial resolution: since the dose is a point quantity, the dosimeter should allow the determination of the dose from a very small volume.
- Ability to detect several radiation types.
- Large dynamic range with a low minimum measurable dose [52].

Figure 2.13: Response characteristics of two dosimetry systems. Curve A first shows linearity with dose, then supralinear behaviour and finally saturation. Curve B first exhibits linearity and then saturation at high doses [52]**.**

Since several different dosimeters exist, a general classification reporting the main types of dosimeters with their advantages and limitations is reported in Table 2.1.

Dosimeter type	Advantages	Disadvantages
Ionization chambers	-Accuracy and precision -Recommended for beam calibration -Instant readout	-Connecting cables required -High voltage supply required -Many corrections required for high-energy beam dosimetry
Semiconductor Devices (diodes, MOSFETs)	-Small size -High sensitivity -Real-time readout -Simple instrumentation	-Connecting cables required -Variability of calibration with temperature -Change in sensitivity with accumulated dose -Special care needed to ensure stability of response -Cannot be used for beam calibration
Film dosimeters (radiographic and radiochromic films)	-2D spatial resolution -Very thin (does not perturb the beam)	-Darkroom and processing facilities required (only for radiographic film) -Small variations between films and batches -Need proper calibration against ionization chamber measurements -Energy dependence problems -Cannot be used for beam calibration
Luminescent dosimeters (thermoluminescent dosimeters, optically-stimulated luminescent dosimeters)	-Small in size -Available in various forms -Some are reasonably tissue equivalent -Inexpensive	-Signal erased during readout -Easy to lose reading -No real-time readout -Accurate results are difficult to obtain -Readout and calibration time consuming -Not recommended for beam calibration

Table 2.1: Overview on the main types of dosimeters with their advantages and disadvantages [52]**.**

2.2.1 Luminescent passive dosimeters

Luminescent dosimeters are the most commonly used passive devices for personal radiation protection around the world. In thermoluminescent dosimeters (TLDs) ionizing radiation passing through the device's material induces the generation of electron-hole pairs (Figure 2.14). Electrons and holes are subsequently trapped in trapping centers within the bandgap, where they remain until thermal energy is provided. As the sample is heated and the temperature increases, trapped electrons are re-excited back to the conduction band. Assuming that this temperature value is lower than that required to free trapped holes, the liberated electrons migrate to near a trapped hole, where they can recombine with the emission of a photon. Optically-stimulated luminescence (OSL) dosimeters are based on a similar principle, however, instead of heat, light (from a laser) is used to release the trapped energy in form of luminescence. In any case, the emission spectrum is then exploited for the dose quantification. The most common thermoluminescent materials are lithium fluoride, calcium sulphate and lithium borate, where trapping centers are introduced by doping [20].

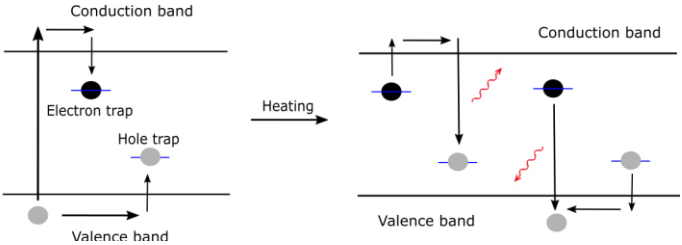

Figure 2.14: Formation of electron-hole pairs with subsequent carrier trapping. During heating, two possible modes of carrier recombination are possible, leading to the emission of a TL photon [20].

In general, TLDs have been and are still nowadays widely used for γ and β dosimetry, displaying linear responses approximately between few hundreds μGy and few tents Gy [13,20]. These devices are mainly used for point dose measurements, although 2D dose distributions can be also obtained by reading TL films with pixelated detectors [53–55]. In recent years, the development of ion beam cancer therapy and the research related to radio-protection in space, stimulated the use of TLDs also for ion dosimetry, especially because of their small dimensions, relative ease of handling, little interference with the radiation field and the usability in solid state phantoms [13,56]. However, the non-linear dose response curve of TLDs represents a limitation in ion dosimetry, resulting in a strong dependence of the device response on the radiation quality and on the particle LET, possibly leading to underestimated dose

measurements [13]. For this reason, there is an increasing interest in developing new passive dosimetry systems for ion dosimetry.

2.2.2 Quantum dots in passive dosimetry

Another possible application of QDs in radiation detection is related with their use in luminescent passive dosimetry systems [15–17,57]. In these context, colloidal QDs embedded in different media are irradiated with ionizing radiation at different doses. The samples are subsequently analyzed and the radiation-induced changes in the QD optical properties are related with the released dose. For example, Stodilka et al. [15] studied the effects of ^{60}Co γ irradiation in ambient air on the optical properties of colloidal CdSe/ZnS QDs dispersed in hexane, showing a degradation of the PL intensity with the increasing dose (0.1-100 Gy), phenomenon attributed to a loss of QD surface ligands (Figure 2.15). Similar results were reported by Gaur et al. [16], studying the X- and γ-ray effects on colloidal CdTe/CdS QDs embedded in a porous silica matrix. The authors correlated the QD PL degradation with radiation-induced photocatalytic oxidation of the thiol ligands and the subsequent formation of surface trap states.

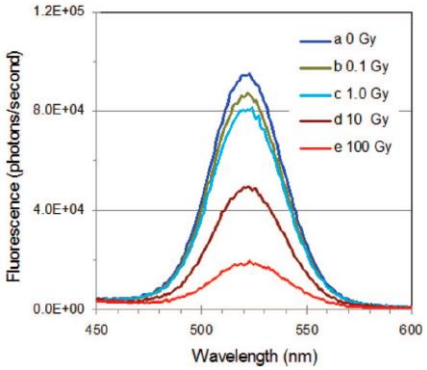

Figure 2.15: PL degradation of CdSe/ZnS colloidal QDs after γ irradiation at different doses [15].

The effects of γ irradiation on colloidal CdSe/ZnS QDs have been also reported by Withers et al. [17], reporting a degradation in the QD PL yield up to 50% after a cumulative exposure of 13 kR to 662 keV γ-rays (^{137}Cs), equivalent to 11.5 krad of absorbed dose. In general, the previous studies provided the proof-of-concept for the development of novel passive dosimeters for γ rays, exploiting the PL degradation of QDs.

Chapter 3 - Materials and methods

In this chapter the main properties of the materials used throughout this work will be presented. Moreover, the characterization techniques adopted for the optical characterization of the samples will be reported. Lastly, an overview about the scintillation measurements and the ion-beam-induced luminescence measurement will be proposed.

3.1 Polysiloxanes

3.1.1 General properties of polysiloxanes

Polysiloxanes, commonly known as silicones, represent a family of organo-silicon compounds based on (-Si-O-) backbone with two monovalent organic radicals attached to each silicon atom (-R_2Si-O-), as shown in Figure 3.1.

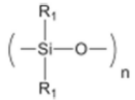

Figure 3.1: General structure of siloxane polymer [58]**.**

These silicon-oxygen bonds have a stronger bond energy (445 kJ/mol) in comparison with that of carbon-carbon bonds (346 kJ/mol) [59], the latters forming the main chain of other organic polymers used for plastic scintillators, like polyvinyltoluene (PVT) and polystyrene (PS). This difference is the main reason for the higher chemical and thermal stability of polysiloxanes in comparison with standard polymers used in scintillation. Moreover, silicones offer high flexibility and very low glass transition temperature (T_g), the latter going from -125 °C for the most known and widely used polydimethylsiloxanes (PDMS), to -30 °C for poly(methyl-phenylsiloxane) (PMPS), as a result of the higher rigidity imposed by the presence of phenyl groups [58]. These features result from the length of the silicon-oxygen bond (1.64 Å), longer then the carbon-carbon bond (1.53 Å), to the regular succession of substituted silicon and non-substituted oxygen and to the wide Si-O-Si bond angle (143°, against 110° for the standard tetrahedral structure). Moreover, the low Tg value reduces the arising of crazing, that strongly decreases the transparency of the material. In this context, crazing is more than an issue in standard plastic scintillators based on the more rigid PVT or PS, which have a Tg around 90°C [58]. Another important feature of polysiloxanes is their relatively high radiation hardness. In fact, in standard plastic scintillators the radiation interactions break the carbon-hydrogen or carbon-carbon

bonds, giving rise to free radicals that cause the yellowing of the material, and the subsequent light yield decrease. These phenomena arise at higher radiation doses in polysiloxanes, because of their stronger bonds. This resistance is further increased if phenyl side groups are present, since the π electrons absorb a fraction of the radiation energy therefore reducing the damage along the polymeric chain [2,3,60]. The addition of phenyl units to the polysiloxane chain confers to the material other important properties, from the scintillation point of view. Firstly, it gives to the material an intrinsic fluorescence, whose emission is related with the distribution and concentration of phenyl units. If more than two monomeric units are present between two phenyl groups, the interaction with neighbours is hindered, and the emission comes from the single monomeric unit (around 290-300 nm). On the other hand, if they are closer the emission arises at longer wavelengths (around 320-340 nm), indicating an emission coming from excimers [2,61]: excited state dimers temporary formed as a result of the interaction between an exited state phenyl group with a ground state one [1]. Anyway, these materials are characterized by the strong absorption of the aromatic groups, occurring around 260-280 nm. The presence of phenyl units also increases the refractive index of these compounds to values close to glass. This feature is of particular importance for scintillation, because it improves the optical matching between the sample and the photodetector window, therefore reducing light losses due to reflection phenomena. As regards the mechanical properties, the presence of aromatic moieties increases the rigidity of the material and therefore also its fragility. From the chemical point of view, the presence of the aromatic groups increases the dye solubility in the material. This is an important aspect since low dye solubility can lead to aggregations that strongly reduce the efficiency of the emitting molecule, and thus the scintillation light yield. Therefore, if high dye concentrations need to be achieved, polysiloxanes having high amounts of phenyl units are needed, although the fragility of the sample will be higher.

3.1.2 Cross-linking reactions

Different cross-linking reactions can be exploited in order to obtain an elastomeric matrix starting from viscous materials. These reactions can be induced spontaneously with the exposure of the precursors to atmospheric conditions as in the case of mono-component resins, or they can be induced with the addition of a second component, as happens in bi-component resins. The cross-linking reactions of interest for this work are of two main types: condensation cure and addition cure [58].
Condensation cure (Figure 3.2) is adopted with both mono- and bi-component resins presenting hydroxide side groups (silanol) and other hydrolysable terminations. In presence of the atmospheric moisture, these groups react with the silanol unit of other polymeric chains, giving rise to the formation of cross-links. Depending on the specific

type of reaction, condensation can be classified as alkoxy condensation, acetoxy condensation, amine condensation, and many others. In all cases, by-products are formed in this process, which are the main drawback of this type of reaction, since they can be difficult to remove.

Figure 3.2: Schematic representation of the cross-linking reaction of condensation, with the formation of volatile by-products [58]**.**

Another type of cross-linking reaction is represented by the addition cure (Figure 3.3). It is based on platinum-catalyzed vinyl addition, also called hydrosilylation reaction, arising between a terminal vinyl group and a hydrogen moiety of two different polymeric chains. The reaction is exploited in bi-component systems, with the addition of platinum as catalyst, in form of metallorganic complex. During this process no by-products are formed allowing for good dimensional stability and high transparency of samples, since the formation of pores and bubbles is highly reduced. Nonetheless, other problems may arise because of the presence of the metallorganic compound that could absorb light, therefore decreasing the transparency of the material. For this reason, it is important not to exceed the given amount of platinum needed for the reaction. In order to further improve the optical properties, a cure moderator can be added to the initial mixture, allowing for extending the pot life of the mixture. In this way, the compete deaeration of the material can be performed before the occurrence of cross-linking. Lastly, although the vinyl addition reaction is a type of room temperature vulcanization (RTV), it occurs faster if it is performed at temperatures around 50°C-60°C.

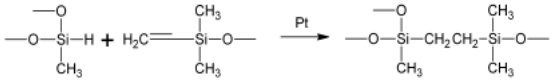

Figure 3.3: Schematic representation of platinum-catalyzed vinyl addition [58]**.**

3.1.3 Polysiloxane matrices used

In this work, different polysiloxane resins have been used:

- PMPS: (99%-100%) polyphenylmethyl siloxane vinyl terminated, purchased from Gelest (code PMV-9925) (Figure 3.4(a));

- PSS22: (22%-25%) diphenylsiloxane-dimethylsiloxane vinyl terminated, purchased from Gelest (code PDV-2331) (Figure 3.4(b));
- PDMS: polydimethylsiloxane vinyl terminated, purchased either from Gelest (code DMS-V21) or from Bluestar Silicones (Rhodorsil RTV 141) (Figure 3.4(c));
- PSS1418: (14-18% diphenylsiloxane)-dimethylsiloxane silanol terminated, purchased from abcr GmbH (code AB116667) (Figure 3.4(d)).

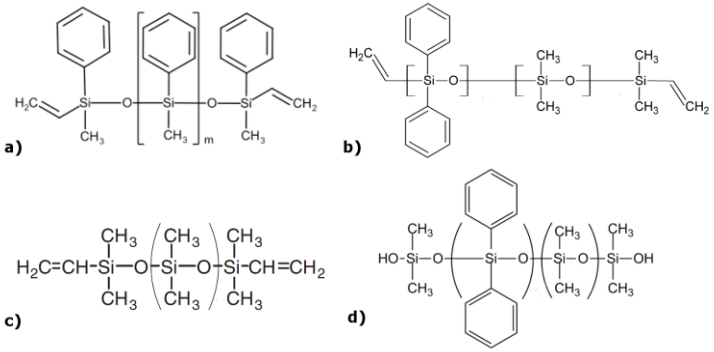

Figure 3.4: Chemical formulas of the base polysiloxane resins used in this work: a) PMPS, b) PSS22, c) PDMS, d) PSS1418.

The first three types are vinyl terminated polysiloxanes and therefore the cross-linking occurs for addition curing. A general standard procedure for the production of a polysiloxane sample using this method consists of a given amount of vinyl terminated polysiloxane (A part) with the addition of hydride terminated polyhydrosiloxane (B part), a cure moderator and a platinum complex, whose relative concentrations depend on the type of polysiloxane. In this work, the polyhydrosiloxane used is poly (45-50% methylhydrosiloxane-comethylphenylsoxane) hydride terminated, the moderator employed is 1,3,5,7-Tetravinyl-1,3,5,7 Tetramethyl-cyclotetrasiloxane, while Platinum-Divinyl-tetramethyl-disiloxane complex in xylene has been used as catalyst. The last type of polysiloxane is silanol terminated and therefore the cross-linking occurs for condensation curing. In this case the crosslinker (PSI-021 polydiethoxisiloxane 20.5-21.5% Si) and the catalyzer dioctyldilauryltin 95% were added in appropriate fractions to the main part. As can be noticed from Figure 3.4, all the polysiloxanes present phenyl groups apart from the simple PDMS (Figure 3.4(c)), which therefore does not present fluorescence properties.

3.2 Dyes

An organic dye suitable for scintillation applications should have the following properties:

- Quantum efficiency as close as possible to unity;
- High radiation tolerance;
- High chemical stability: it should not react with matrix or solvent materials, with other dyes or with other elements in the operating environment, since these reactions could decrease the efficiency of the dye;
- High solubility within the matrix.

Moreover, in order to choose the proper dye for a given system, it is relevant to have a wide overlap between the matrix emission and the primary dye absorption, and between primary dye emission and secondary dye absorption. This allows for the occurrence of energy transfer, essential for high scintillation efficiency, as reported in the previous chapter.
The organic dyes of interest for this work are 2,5-Diphenyloxazole (PPO) (Figure 3.5) as primary dye and a molecule belonging to the family of 1,8-Naphthalimides (Figure 3.6), commercially known as BASF Lumogen Violet (LV), as secondary dye (wavelength shifter).
2,5-Diphenyloxazole (PPO) has been used as dye in plastic scintillators since many years. Its use arises from the need to overcome the solubility of other common dyes, as p-terphenyl. In general, the replacement of a phenyl group with an oxazole or oxadiazole group greatly increases the solubility of a linear aromatic chain, without significantly affecting its quantum efficiency [1]. Furthermore, beside the high efficiency (close to unity) and the high solubility also in polysiloxane, PPO also demonstrated good radiation hardness [62]. Lastly, the molecule has an emission spectrum centered at about 360 nm and an excitation spectrum centered at 300 nm. The latter is well matching the emission of many polysiloxane bases, therefore allowing for a good energy transfer from the matrix to the primary dye.

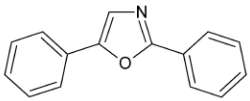

Figure 3.5: Molecular structure of the molecule 2,5-diphenyloxazole (PPO).

As regard the BASF Lumogen F Violet 570 (LV), it was originally used as dye in photovoltaic applications. It has an efficiency close to 85%, and it has been

demonstrated to be a very promising secondary dye in plastic scintillators, coupled with PPO as primary dye [6,63]. In fact, the molecule has an excitation spectrum very well overlapping with the PPO emission and it has an emission peak centred at 425 nm, corresponding the wavelength of maximum sensitivity of the most common PMTs.

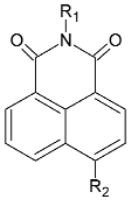

Figure 3.6: Generic molecular structure of 1,8-Naphthalimide, where the substituents R1 and R2 are patented for the LV molecule.

3.3 ^{6}LiF crystals

The ^{6}LiF crystals used for the thermal neutron sensitization of polysiloxane scintillators were synthesized by co-precipitation method [64]. In this process, ^{6}Li metal (enrichment 95%, purchased from Spectra 2000), was cut from an ingot and made to react with heated diluted hydrochloric acid, producing ^{6}LiCl. In order to obtain different crystallite sizes, the produced ^{6}LiCl white salt was dissolved in different ratios of water:ethanol (W:EtOH) mixture. A solution of ammonium fluoride NH_4F 0.2 M, dissolved in the same mixture, was added dropwise to the ^{6}LiCl solution. After few hours of stirring, the solution was centrifuged and the solids washed several times with distilled water. The ^{6}LiF crystals were then recovered after drying at 40°C under vacuum for several hours.

3.4 Colloidal quantum dots

The colloidal QDs used in this work are all commercial core-shell nanocrystals of type I, with electrons and holes confined in the core [44]. Depending on specific needs, QDs of different materials and features were used:

- InGaP/ZnS QDs, purchased from Evident Technologies, dispersed in toluene at the concentration of 2.5 mg/ml and functionalized with tri-n-octylphosphineoxide (TOPO). Declared emission wavelength of 656 nm.
- CdSe/ZnS QDs, purchased from Sigma-Aldrich, dispersed in toluene at the concentration of 5 mg/ml and functionalized with octadecylamine. Declared emission wavelength of 540 ± 10 nm.

- CdSeS/ZnS QDs, purchased from Sigma-Aldrich, dispersed in water at the concentration of 1 mg/ml and functionalized with carboxylic acid. Declared emission wavelength of 575 ± 10 nm.
- CdSe/ZnS QDs, purchased from Sigma-Aldrich, dispersed in water at the concentration of 1 mg/ml and functionalized with carboxylic acid. Declared emission wavelength of 540 ± 10 nm.

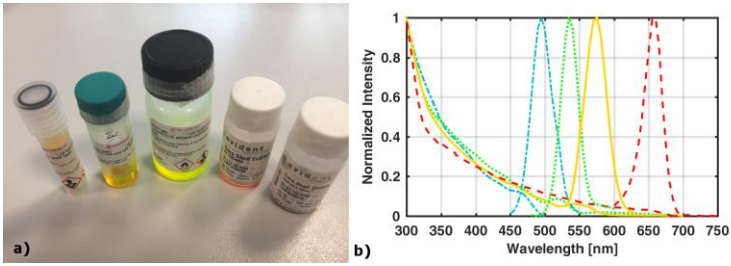

Figure 3.7: a) Different colloidal QDs in their vials and b) absorption and emission spectra of colloidal CdSe/ZnS QDs of different sizes.

3.5 Sample preparation

Since different types of samples have been prepared in this work, the production procedure may present small variation and therefore further specifications will be given in the appropriate chapters. However, the common steps of the procedure are:

- dissolution within the main part of the polysiloxane resin of a given solute, which can be either organic dyes (PPO and then LV), ^{6}LiF:Ag powder or colloidal QDs. The resulting mixture is stirred for some minutes at room temperature;
- the other components of the polysiloxane material are added in the proper quantities, depending on the type of resin used, and the resulting mixture is stirred for some more minutes at room temperature;
- the mixture is poured into a mold having the desired dimensions and the samples are degassed in low vacuum, in order to remove gas and bubbles produced during the stirring process;
- the mold is put in an oven for 12-48 hours (depending on the type of resin) at 60°C to accelerate the cross-linking reaction.

3.6 Characterization techniques

3.6.1 Optical measurements

The measurements adopted for the optical characterization of samples involved UV-Vis spectroscopy, steady-state fluorescence spectroscopy and time-resolved fluorescence spectroscopy.

3.6.1.1 UV-Vis spectroscopy

Absorbance and/or transmittance measurements were performed by using a Jasco V-570 double beam spectrophotometer, equipped with a deuterium lamp, (covering the range 190 nm - 350 nm) and a halogen lamp (covering the range 330 nm - 2500nm).

3.6.1.2 Steady-state fluorescence spectroscopy

Steady-state fluorescence measurements were performed by using either a Jasco FP-6300 spectrofluorometer or an optical system composed by an excitation source (either a laser or a LED) and an Ocean Optics QE65000 optical spectrometer equipped with an optical fiber.
The Jasco FP-6300 spectrofluorometer is equipped with a 150-Watt Xe lamp with shielded lamp house. The system is composed of excitation and emission monochromators, both having variable spectral bandwidths of 2.5, 5, 10, and 20 nm. Scanning speeds are step variable from 20 nm/min to 10,000 nm/min. The wavelength range provided is from 220 nm to 750 nm. The fluorescence emission and excitation spectra for the characterized samples were measured in front-face geometry. Spectra were acquired through the software SpectraManager.
The other optical system is composed of an excitation source that can be, depending on specific needs, one of the following:

- Horiba NanoLED model N-375L, emission wavelength of 375 ± 10 nm and pulse width <200 ps (Laser-diode head);
- Horiba NanoLED model N-280, emission wavelength of 285 ± 10 nm and pulse width <1.2 ns (LED head);
- PicoQuant PCL 800-B picosecond pulsed laser diode, emission wavelength of 470 ± 10 nm and pulse width <300 ps;
- Roithner LaserTechnik GmbH, model dl-7146-301s, emission wavelength of 405 ± 10 nm and pulse width <600 ps;
- Laser-compact model LCS-DTL-374QT, emission wavelength of 355 ± 10 nm and pulse width <10 ns.

As reported in Figure 3.8, the illumination source excites the sample which is located above a sample holder. The light emitted by the sample passes through a 4x Leica collimation optics and it is collected by an optical fiber (diameter 600 μm) connected with the Ocean Optics QE65000 portable spectrometer, which is equipped with a Hamamatsu S7031-1006 CCD detector having a spectral range of 200-1100nm. Spectra were acquired through the software SpectraSuite.

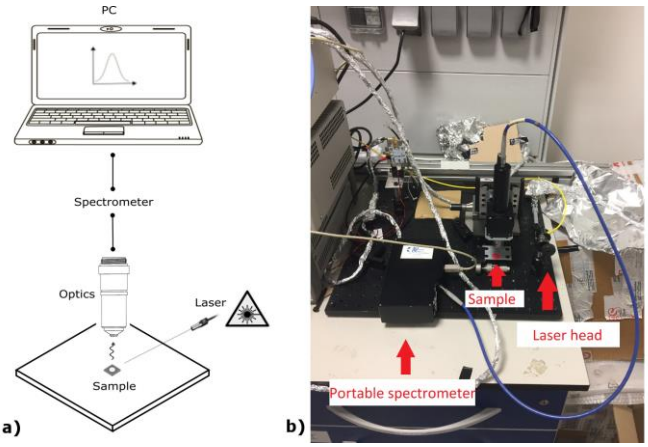

Figure 3.8: a) Schematic drawing and b) picture of the optical setup for steady-state fluorescence measurements.

3.6.1.3 Time-resolved fluorescence spectroscopy

Time-resolved fluorescence measurements were acquired by using a time-correlated single-photon counting (TCSPC) module (PicoQuant PicoHarp 300) coupled with either a silicon photomultiplier detector (NUV from AdvanSiD) or a Hamamatsu H10721-04 photomultiplier tube (PMT) (Figure 3.9). As regard the excitation source, one of the laser sources reported previously for the steady-state measurements was used depending on specific needs. Moreover, in order to acquire time-resolved measurement at specific emission wavelengths, a Horiba Monochromator is connected to the system, allowing for the selection of a wavelength between 180 and 1000 nm with a bandpass adjustable from 0 to 24 nm. Measurements are acquired through the software PicoHarp. Deconvolution of time-resolved curves with the Instrument Response Function (IRF) and their fitting were performed using DecayFit (Fluorescence Decay Analysis Software 1.3, FluorTools). Biexponential fitting of the time-resolved curves was performed with a function of the type:

$$I(t) = A_f e^{-\frac{t}{\tau_f}} + A_s e^{-\frac{t}{\tau_s}} \quad (3.1)$$

where τ_f and τ_f are the fast and slow lifetimes, respectively, and A_f and A_s their amplitudes. The fractional amplitude contribution of each component, either fast or slow, in the multi-exponential decay, was calculated by the following relationships [26]:

$$f_{fast} = \frac{A_{fast}\tau_{fast}}{A_{fast}\tau_{fast} + A_{slow}\tau_{slow}} \quad (3.2)$$

$$f_{slow} = \frac{A_{slow}\tau_{slow}}{A_{fast}\tau_{fast} + A_{slow}\tau_{slow}} \quad (3.3)$$

The average lifetime was calculated as [26]:

$$<\tau> = \frac{A_{fast}\tau_{fast} + A_{slow}\tau_{slow}}{A_{fast} + A_{slow}} \quad (3.4)$$

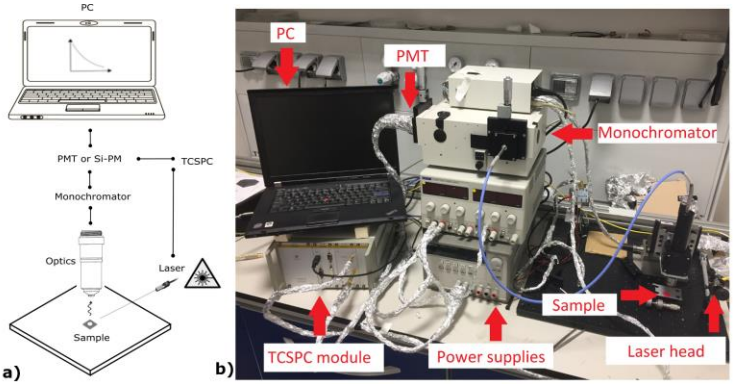

Figure 3.9: a) Schematic drawing and b) picture of the optical setup for time-resolved fluorescence measurements.

3.6.2 Scintillation measurements

3.6.2.1 Light yield measurements

Scintillation measurements were performed by coupling the polysiloxane scintillator with a PMT using a small amount of optical grease. To limit external loss of the scintillation light, sample was covered with an aluminized mylar sheet (Figure 3.10).

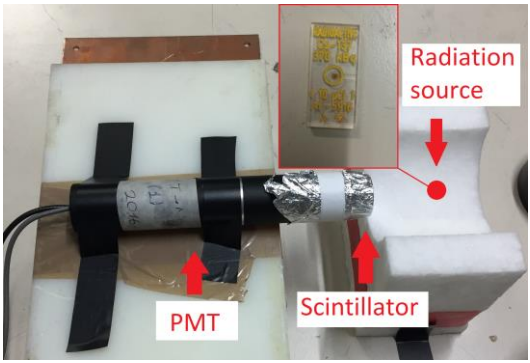

Figure 3.10: Picture reporting the general scintillation measurement geometry.

As source of radiation, light yield measurements were performed with γ-ray sources such as ^{137}Cs and ^{60}Co. Depending on the sample size, measurements were performed with two different PMTs (Hamamatsu H6524 and H1949-51), whose main features are reported in Table 3.1.

	Hamamatsu H6524	Hamamatsu H1949-51
Sensitivity range (nm)	300-650	300-650
Maximum sensitivity (nm)	420	420
Applied voltage (V)	-1100	-1500
Gain	1.7×10^6	2.0×10^7
Photocathode diameter (mm)	15	46

Table 3.1: Main features of the PMTs used in this work.

The PMT voltage was applied using a CAEN V6553 bias supply. The anode signal from PMT was directly read by a digitizer, model CAEN V1730, featuring 14-bit resolution with a 2 V peak-to-peak dynamical range and a sampling rate of 500 MSample/s. Within the CAEN module, an amplifier produces gaussian signals having amplitude proportional to the integral of the scintillation pulse. The signal is subsequently converted by an analog to digital converter (ADC) and a channel, proportional to the gaussian amplitude, is assigned to each signal. In this way the scintillation spectrum is recorded as a histogram displaying the number of counts for each channel. The higher the intensity of the scintillation pulse, the higher the channel number of the signal. As already mentioned, due to the composition of the scintillators (low Z and low density), the main interaction occurring when γ-rays impinge on the detectors is Compton scattering. Therefore, the light output (LO) is proportional to the Compton edge channel, and the relative scintillation yield is typically calculated as

compared to commercial scintillators, whose yield is known from manufacturer datasheets. Moreover, the Compton edge can be used to convert the pulse integral from channels to energy in keV *electron equivalent* (keVee), in a procedure known as *energy calibration* and described in [65,66]. We remind that, since the light yield depends on the type of particle, the unit keVee is used to quantify the light yield on an absolute basis. In this convention, the particle energy required to generate 1 keVee of light by definition is 1 keV for fast electrons [20].

3.6.2.2 Pulse shape discrimination measurements

For pulse shape discrimination (PSD) measurements, the sample is exposed to a neutron/γ source using a shielded ^{252}Cf source (about 5 × 10^4 neutrons/s), as shown in Figure 3.11. For fast-neutron/γ PSD measurements, lead is used as shielding material in order to selectively reduce the γ rate with respect to neutron rate. For thermal-neutron/γ PSD measurements, polyethylene is used in order to slow down neutrons. The distance between the source and the scintillator is set in order to have a suitable counting rate for acquiring a measurement with a good statistic in a reasonable period of time. The signals produced by the PMT are then fed into the CAEN V1730 digitizer, allowing for recording full waveforms of any single scintillation pulse.

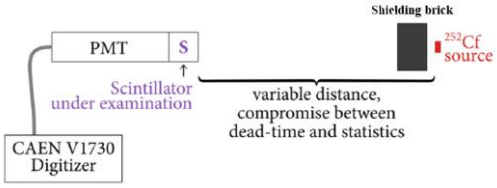

Figure 3.11: Experimental set-up for pulse shape discrimination measurements [9].

The PSD analysis, allowing for distinguish neutrons from gamma events, was carried out through the integration method used by Cester et al. [67], where two time intervals for integration of the scintillation pulse are defined in order to derive the pulse shape parameter (PSP). Thanks to internal FPGA (Field Programmable Gate Array), the digitizer provides for each event the following key parameters: the time stamp (a reference time from the beginning of the acquisition) and two integrals of the signal: one for the raising part of the signal, Q_{fast}, and for the total integral of the signal, Q_{total}. From these two integrals, the integral of the signal tail, Q_{tail}, can be easily obtained ($Q_{tail} = Q_{total} - Q_{fast}$). The PSP is therefore calculated, for each pulse, as:

$$PSP = \frac{Q_{total} - Q_{fast}}{Q_{total}} = \frac{Q_{tail}}{Q_{total}} \tag{3.5}$$

The PSP depends therefore on the shape of the scintillation signal, and it allows for distinguishing the events produced by different particles. Since every event (pulse) is characterized by a PSP and a Q_{total} (proportional to the light output), after several events a 2D histogram can be created, as reported in Figure 3.12(a), where γ-rays are characterized by a lower PSP and fast neutron by a higher PSP. Moreover, aiming at a clearer characterization of the n-γ discrimination capability of the scintillators and at a reliable comparison between different composition, size and age, a figure of merit (FoM) is usually calculated, that is defined as:

$$FoM = \frac{\Delta}{\delta_n + \delta_\gamma} \tag{3.6}$$

where Δ is the separation between the PSP centroids of neutron and γ distributions, and δ_n and δ_γ are the FWHM of the neutron and γ peaks, respectively. These values are calculated by fitting the two gaussian-like peaks resulting from the projection of the 2D PSD histogram on the y axis over a given energy threshold, as reported in Figure 3.12 (b).

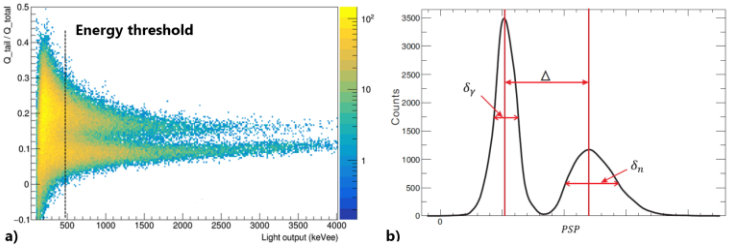

Figure 3.12: a) Example of 2D histogram showing the PSP versus light output where the dashed line indicates the threshold over which the FoM is calculated [9]. b) Example of projection of the 2D PSP distribution on the y axis over a given energy threshold [68]**.**

3.6.2.3 Time-of-flight measurements

In Time-Of-Flight (TOF) measurements, the large difference in the velocity of photons and neutrons is exploited for the classification of each particle on the basis of the difference in the arrival time. The particle identification on the basis of TOF classifications can be exploited as a reference to evaluate the performance of the chosen PSD method, using a two-dimensional correlation plot between the measured

PSP and the TOF. The TOF set-up consisted of a commercial scintillator used as "start" reference (EJ-301 liquid scintillator). The ^{252}Cf source was placed in front of the EJ-301 detector, while the triggering "stop" detector, i.e. the scintillator under study, was placed at a distance of 100 cm from the source, as reported in Figure 3.13. The TOF calculation is performed by the CAEN V1730 digitizer thanks to a Digital Constant Fraction Discrimination (DCFD) embedded in the firmware, allowing for very accurate on-line time measurements.

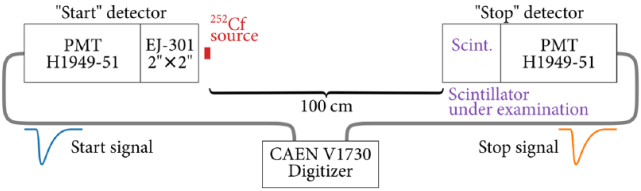

Figure 3.13: Experimental set-up for the TOF measurements [9].

3.6.3 Ion-beam-induced luminescence measurements

Ion-beam-induced luminescence (IBIL) measurements were performed either at the Legnaro National Laboratories (Padova, Italy) using the AN2000 Van de Graaff accelerator or at the proton therapy center of Trento, Italy. The AN2000 accelerates either H^+ or He^+ at the energy of 2 MeV with tunable beam spot sizes of few mm^2 and beam currents of few tens of nA. Irradiation occur in a vacuum chamber, where the sample is placed. In the proton therapy facility of Trento a cyclotron accelerates H^+ in the energy range 70-228 MeV, with beam spot size from few mm^2 to few tens mm^2 and beam currents in the range 1-320 nA [69]. Measurements are performed in air and if needed the energy of the beam can be decreased with appropriate absorber layers. In both facilities, ion-induced luminescence spectra are acquired by using a silica optical fiber (600 μm diameter) coupled with the Ocean Optics QE65000 portable spectrometer (Figure 3.14). The dedicated software (SpectraSuite) allows for acquiring multiple spectra during the irradiation by setting the integration time of each spectrum and the number of spectra to consecutively store.

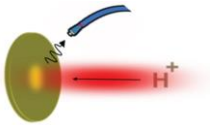

Figure 3.14: Schematic drawing representing the sample irradiation with H^+ ions and the real-time acquisition of the emitted light.

3.7 Simulation software

3.7.1 Stopping and Range of Ions in Matter (SRIM)

SRIM (Stopping and Range of Ions in Matter) is a software package based on Monte Carlo simulation methods developed by J. F. Ziegler and J. P. Biersack in 1980s for simulating the interaction of ions with matter [70]. As input parameters, it needs the ion type and energy (in the range 10 eV - 2 GeV) and the material composition of one or several target layers. As output, it plots the distribution (in 2D or 3D) of the ions in the solid and it provides several parameters, such as the particle penetration depth (range), the ion spread along the beam (straggle), the concentration of vacancies, the phonon production in the target material, the energy partitioning between the nuclear and electron losses, and several other information.

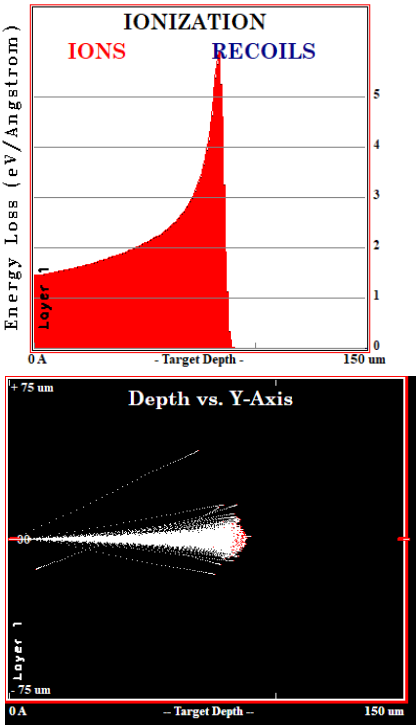

Figure 3.15: Example of SRIM simulation of 2 MeV protons impinging on a 150 μm layer of polydimethylsiloxane, providing the energy loss profile of the ions (top) and their longitudinal collision plot (bottom).

Chapter 4 - Polysiloxane-based organic scintillators for fast neutron detection

Part of this chapter has been published in:

SCIENTIFIC REPORTS
nature research

T. Marchi, F. Pino, C. L. Fontana, A. Quaranta, E. Zanazzi, M. Vesco, M. Cinausero, N. Daldosso, V. Paterlini, F. Gramegna, S. Moretto, G. Collazuol, M. Degerlier, D. Fabris & S. M. Carturan, *"Optical properties and pulse shape discrimination in siloxane-based scintillation detectors"*, Scientific Reports, 9 (2019) 9154.

In this chapter we report the study and characterization of polysiloxane scintillators embedding organic dyes for the detection of fast neutrons. The samples, composed of different primary dye concentrations, will be characterized with both steady-state and time-resolved fluorescence measurements. Then, their scintillation response will be investigated by coupling the scintillators with a photomultiplier tube and exposing the system to a given radioisotope. Scintillation light yield and pulse-shape discrimination capabilities of the polysiloxane scintillators will be compared with those of state-of-the-art scintillators based on polyvinyltoluene.

4.1 Introduction

As already mentioned, one of the stringent requirements when dealing with scintillators for the detection of fast neutrons is their pulse shape discrimination (PSD) capabilities, in order to distinguish fast neutrons from the γ-ray background. To date, the most common scintillators having fast-neutron/γ-ray discrimination capability are liquid-based systems like EJ-301 and BC-501A, where the toxicity level of the solvent used (a benzene-parent compound) is among the highest ones in the class of chemicals. Recently, less hazardous solvents having reduced vapour pressure at room temperature, higher flash-point and, in turn, minor health risk, have been proposed as dissolving media for scintillation substances, as in the case of EJ-309. Among them, linear dialkylbenzene (LAB) [71,72], and diisopropylnaphthalene (DIPN) [73] are the most common. Although with LAB or DIPN significant advances has been achieved as related to safety concerns, the problem of waste disposal or liquid spillage still represents a critical issue, because of the large volumes needed to perform efficient fast neutron/γ-rays detection. For these reasons, the need to develop solid scintillators capable of PSD is continuously growing.

In fast neutrons and γ-rays detection, the particles indirectly measured by the scintillators are recoil protons from fast neutrons and recoil Compton electrons from γ-rays (Chapter 1). Protons have a higher linear energy transfer (LET) than electrons, giving rise to a higher density of ionization events along their path. The higher the

ionization density, the higher the rate of formation of long-living triplet states (T_1), as a result of recombination of ionized dye molecules with electrons [74]. Two close T_1 molecules can experience triplet-triplet annihilation (TTA) generating a ground S_0 and an excited S_1 singlet state, that in turn decays with the emission of a delayed photon [75,76]. This delayed fluorescence has characteristic times of the order of tens of ns and it has the same emission wavelength of the prompt fluorescence emission, whose time scale is few ns. The intensity of the component having longer lifetime increases with the concentration of triplet states, therefore recoil protons give rise to scintillation pulses with a more intense long-living component in comparison with Compton electrons, therefore allowing their distinction through PSD techniques. Since TTA is a bimolecular short-range mechanism (less than 1 nm), in liquid scintillators this process can be favoured by diffusion phenomena, as demonstrated by many authors [27,74,75]. On the other hand, in plastic polymers such as polyvinyltoluene (PVT) or polystyrene (PS), TTA mechanism is hindered due to the stillness of the molecules in the rigid medium. Recently, a PVT-based scintillator with 30 wt.% of 2,5 diphenyloxazole (PPO) as primary dye and traces of 9,10–diphenylanthracene (DPA) as waveshifter has been proposed by Zaitseva et al. [40]. These concentrations assure the proximity of fluorescent molecules in order to promote the overlap of their orbitals, while the interacting radiation leads to the TTA mechanism by directly ionizing the PPO molecules. Then, the final singlet excited states, which could give rise to delayed fluorescence, transfer their energy to the waveshifter. It has been demonstrated that this commercially available scintillator (EJ-299-33A, Eljen Technology) presents optimal PSD capabilities in comparison with traditional liquid scintillators [41,67,77]. However, the long-term stability of the final highly-PPO loaded scintillator is still under investigation [76]. In fact, the high loading of the polymer network of extraneous compound can decrease the overall mechanical and thermal resistance, leading to deformation and deterioration with time of the device. Very recently, Zaitseva and co-workers published new results related to an upgraded version of EJ-299-33A, where light transmission and mechanical stability over time have been improved [78].

Another solution for enabling PSD in a solid scintillator can be explored by favouring the formation of PPO dye aggregates, with specific conformation to collect energy from the matrix through Förster-type mechanism, and allowing for the access to T_1 states in close proximity to promote TTA. In this context, the particular structure of polysiloxanes can be exploited for enabling PSD without increasing the load of primary dye beyond the limit where irreversible modifications in the main features of the polymer occur. Polylsiloxane elastomers are known to be extremely versatile since the main backbone is constituted by the strong, flexible Si-O-Si bridging bond, whereas lateral substituents of the Si atom can be changed to properly functionalize the main chain, therefore changing selectively some specific features, such as optical transparency, thermal resistance, refractive index and gas permeability/selectivity.

The PPO structure has two lateral, non-polar phenyl groups bounded to a five-atoms ring comprising two heteroatoms, oxygen and nitrogen, which makes the central portion of the molecule quite polar and capable of hydrogen-bonding as acceptor. The solubility of PPO is very low in polydimethylsiloxanes, but it can be increased by using precursor siloxane resins with phenyl lateral substituents in the main structure. Moreover, the peculiar conformational structure of polymethylphenylsiloxane (PMPS) has been thoroughly studied [2,3,79,80], and it was demonstrated that stable stacking of phenyl lateral rings can arise, where dyads and triads are optically active as excimers. Therefore, those specific excimers forming sites in PMPS can be exploited to collect PPO molecules in order to form a sandwich-like microstructures: in this way, if high amounts of T_1 excited states are created, the rate of TTA is enhanced due to the closeness of the molecules. Simultaneously, the amount of PPO needed to enable this phenomenon could be limited to few wt.%, without compromising the final thermal and optical properties of the polymer matrix.

4.2 Experimental section

PMPS (subsection 3.1.3) samples were prepared according to the procedure reported in subsection 3.5, with PPO concentrations from 1 to 6 wt.% and fixed LV concentration of 0.02 wt.% (24 h of cross-linking reaction at 60°C). Samples were prepared in two different sizes. Small samples (10 mm thickness and 25.4 mm diameter, Figure 4.1) were prepared with different PPO concentrations (2, 4, 6 wt.%) in order to evaluate the effect of the increasing primary dye on PSD performances, using an EJ-212 commercial scintillator of the same size for comparison purposes. Large samples (50 mm thickness and diameter) were prepared for comparison with EJ-299-33 and EJ-200 commercial scintillators of the same size. Samples aged 3 months and 3 years were analyzed for further comparison.

Figure 4.1: Pictures of samples (1" diameter, 1 cm thickness) produced in different years and with different PPO concentrations.

Samples with only PPO, without LV addition, were prepared for the sake of clarity in the optical measurements (with PPO concentrations from 1 to 8 wt.%). Summary of all the samples with their features is reported in Table 4.2. Absorbance spectra were acquired with the Jasco V-570 spectrophotometer (subsection 3.6.1.1). Steady-state

fluorescence measurements were acquired with the Jasco FP-6300 spectrofluorometer (subsection 3.6.1.2). Time-resolved fluorescence measurements were recorded with the 285 nm LED (subsection 3.6.1.3) at four different emission wavelengths (361, 385, 426 and 500 nm). Scintillation measurements (light yield, PSD and TOF) were performed as reported in subsection 3.6.2.

4.3 Results and discussion

4.3.1 Optical measurements

Optical measurements were performed on samples containing only PPO, with concentrations up to the maximum value of 8 wt.%, since at higher concentration aggregates visible to the naked eye were present, demonstrating a low solubility of the dye in PMPS. Nevertheless, up to 8 wt.% of loading the samples show negligible effects on the optical transparency, as demonstrated by the absorbance spectra reported in Figure 4.2(c). Moreover, the low amount of PPO is not expected to be in contrast with the proximity of the luminescent molecules even at this low concentration level with respect to the one used in aromatic polymers like PVT, as already mentioned. Hence, in order to analyze the distribution of PPO molecules into the PMPS matrix, we performed spectral and lifetime luminescence measurements on samples with different PPO concentrations, namely 1, 4, 6 and 8 wt.%.
Fluorescence emission spectra, acquired under 250 nm excitation, for samples with different PPO concentration are reported in Figure 4.2(a). In Figure 4.2(b), the same spectra are shown by normalizing the intensity to the maximum value. The presence of a long wavelength component at 420 nm for high PPO concentrations can be clearly identified. Its presence was correlated with the formation of excimers between an excited state and a ground state PPO monomer molecule, according to the following scheme:

$$S_1 + S_0 \rightarrow (SS)^* \rightarrow S_0 + S_0$$

In fact, the same effect has been observed also in PPO dispersed in toluene solutions [81,82], where for high PPO concentration enhanced excimer emission and decreased monomer emission can be observed, showing spectral features similar to the PMPS sample loaded with 6 wt.% of PPO. The PPO excimer formation and its features concerning the emission peak position and lifetime have been deeply investigated by several authors [81,83,84], by varying dye concentration, solution temperature and solvent viscosity. At high dye concentrations, the interaction probability between molecules increases, therefore the formation of excimers is promoted, as can be observed from the gradually more pronounced intensity of the long wavelength

feature. On the other hand, this increases self-absorption and thus concentration quenching. Figure 4.2(d) reports the time-resolved curves of the different samples acquired at the emission wavelength of 426 nm and at the excitation wavelength of 285 nm. As can be seen, the decaying part of the curves shows a double exponential character, with a long lifetime component whose relative contribution increases with PPO concentration, in agreement with previously reported results on PPO dissolved in liquid siloxanes [85].

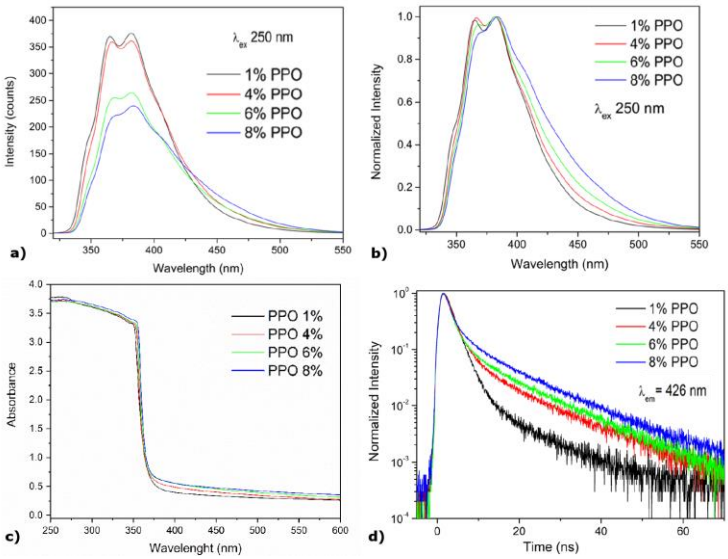

Figure 4.2: Optical measurements on samples containing only PPO: a) non-normalized and b) normalized fluorescence emission spectra; c) UV-Vis absorbance spectra; d) time-resolved fluorescence measurements.

PPO (wt.%)	τ_f (ns)	τ_s (ns)	f_f/f_s
1	2.09 ± 0.01	14.9 ± 0.3	7.8 ±0.7
4	2.20 ± 0.02	15.1 ± 0.9	2.5 ± 0.3
6	1.87 ± 0.02	13.1 ± 0.8	1.3 ± 0.1
8	1.72 ± 0.01	11.9 ± 0.6	0.6 ± 0.05

Table 4.1: Fitting results of the time-resolved curves.

Therefore, time-resolved curves were fitted with a double exponential function as reported in subsection 3.6.1.3. Table 4.1 reports the lifetimes with the error bars and the ratios between the fractional contributions of fast and slow components for the different concentrations. It is worth precising that the higher errors associated with the

slow lifetimes are due to the higher instrumental noise detected in the tail of the pulse. As can be noticed, τ_f is around 2 ns, with the value decreasing with increasing PPO concentration. On the other hand, τ_s is in the range between 15 and 11 ns. By increasing the dye concentration, the ratio between the fractional contribution of fast and slow components decreases of one order of magnitude, indicating an increasing contribution of the slower decay in the luminescence lifetime. The fast and slow components are generally ascribed, respectively, to the regular singlet-singlet transition [81,86], and to the emission of excimers formed by the coupling of very close PPO molecules [87,88]. The calculated data are in good agreement with other values previously reported for PPO in liquid solutions [88,89]. This comparison demonstrates that in phenyl-substituted polysiloxane the aggregation of monomers and formation of dyads of PPO is possible also at concentrations below 10 wt.%. In fact, the amount of PPO, which can be considered limited, does not imply a degradation of the intrinsic features of the polymer itself, which remains transparent and firm for several years. Moreover, the biexponential character of the time-resolved curves indicates that excimers are formed in the matrix even at 1 wt.% of concentration. By evaluating the relative excimer amount through the f_f/f_s ratio, where the f_s factor is proportional to the concentration of excimer in the sample, we can assert that it increases of more than one order of magnitude from 1 to 8 wt.% of concentration.

4.3.2 Scintillation measurements

4.3.2.1 Light yield measurements

Light yield measurements have been performed by exposing the samples to a ^{137}Cs γ-ray source. The pulse integral (Q_{total}) spectra for the 1" and 2" samples with different concentrations of PPO are reported in Figure 4.3. The light output (LO) is proportional to the Compton edge (CE) channel for each sample, and the relative scintillation yield was calculated as compared to commercial scintillators, namely EJ-212 or EJ-200, whose light yield is known from manufacturer datasheets [90]. The obtained values and the characteristics of each scintillator in terms of size, composition and age of production are reported in Table 4.2. It is worth precising that EJ-200 and EJ-212 are formally the same type of plastic scintillator as far as the LO is concerned (in terms of % of anthracene it is 64% for EJ-200 and 65% for EJ-212, the only difference between the two scintillators is the attenuation length, higher for EJ-200). Concerning the small samples (Figure 4.3(a)), the LO progressively decreases as the PPO concentration increases. This is coherent with the fluorescence emission spectra reported in Figure 4.2(a), where reabsorption and concentration quenching phenomena induced by the high amount of dye lead to a remarkable intensity drop. For small samples (1" diameter, 10 mm thickness), produced three months before the measurements (labeled 3m in Table 4.2), the scintillator with 2 wt.% PPO shows a LO of 56% respect

to EJ-212. This value moderately decreases by increasing the PPO concentration, down to 45% for 4 wt.% PPO and 42% for 6 wt.% PPO. Samples produced with the same composition two years before the measurements (labeled 2y) exhibit comparable light output, therefore demonstrating their high stability with time and weathering resistance. Regarding the thicker (2") samples, the standard plastic scintillator EJ-299-33A for n-γ discrimination purposes shows a LO of 62% respect to EJ-200 of the same size.

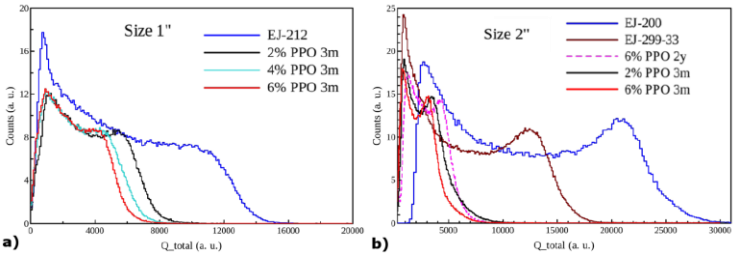

Figure 4.3: Pulse integral spectra of scintillators of different size a) 1" and (b) 2" upon exposure to ^{137}Cs source. In (a) the response of samples produced 3 months before the analysis with increasing PPO wt.% are shown.

Sample	Size Ø (mm) × h (mm)	Volume (cm^3)	% LO
EJ-212	25.4 × 10	5.1	100
PMPS 2% PPO (3m)	25.4 × 10	5.1	56
PMPS 4% PPO (3m)	25.4 × 10	5.1	45
PMPS 6% PPO (3m)	25.4 × 10	5.1	42
PMPS 2% PPO (3y)	25.4 × 10	5.1	57
PMPS 4% PPO (3y)	25.4 × 10	5.1	51
PMPS 6% PPO (3y)	25.4 × 10	5.1	47
EJ-200	50 × 50	98	100
EJ-299-33A	50 × 50	98	62
PMPS 2% PPO (3m)	50 × 48	94	20
PMPS 6% PPO (2y)	50 × 44	86	22
PMPS 6% PPO (3m)	52 × 53	112	17

Table 4.2: Sizes and light output of the scintillators under test. Light output is estimated with respect to standard scintillators, using ^{137}Cs γ-rays source. Sample age is also indicated.

Concerning the scintillator with 6 wt.% PPO (2" in diameter and thickness), aged 2 years, the LO is strongly decreased to 22% of the standard EJ-200. Such a low value can be partially correlated with the lower attenuation length of polysiloxanes in

comparison with PS and PVT-based systems, as indicated by transmission spectra reported in the literature [91]. Interestingly, the same composition but related to a sample aged only 3 months before the measurement shows a slightly lower LO owing to the increased optical path of the object (53 mm versus 44 mm), thus demonstrating that light loss due to reabsorption events is a crucial issue. On the other hand, the decreasing of the scintillation yield by increasing the sample size is a well-known phenomenon associated to several factors, namely self-absorption [1], scattering loss at the surface [92,93], proper wrapping [94], coupling with the PMT [95]. Indeed, the observed variation in light yield is quite high and some other phenomena could potentially contribute in lowering the light collection at the PMT interface. More specifically, the production of large-size siloxane scintillators can be optimized as for flatness of the contact surface with PMT window, PPO dissolution level, which requires longer times than in small samples, precise control of the Pt added catalyst, that should be as low as possible to minimize the formation of Pt nanoclusters with subsequent yellowing. All these aspects are currently being considered in the preparation of new large-size samples for a more complete and systematic characterization.

4.3.2.2 Pulse shape discrimination measurements

The averaged signals of fast neutron and γ-ray events, for the 1" and 2" PMPS scintillators with 6 wt.% PPO and for their corresponding standards of the same size, are reported in Figure 4.4. The signals correspond to a deposited energy of 480 ± 10 keVee. The waveforms related with the PMPS-based scintillators (6 wt.% PPO, either 1" or 2" in size) clearly indicate a discrimination between fast neutrons and γ-rays, while the sample EJ-212 does not show, as expected, a remarkable difference in the tail of the signal for different incident particles. Interestingly, the decay profiles in the case of EJ-299-33, the commercial standard for fast neutrons/γ-rays discrimination, are quite similar to those collected with the siloxane sample, therefore indicating a promising behaviour as far as PSD capability is concerned. In order to select the optimal parameters to set in the signal processing for the best particle discrimination, the most suitable time windows for integration of both the fast component and the slow one have been selected empirically, by optimizing the separation between γ-rays and fast neutrons signals. Then, the Pulse Shape Parameter (PSP) and the Figure of Merit (FoM) were calculated (subsection 3.6.2.2).
In Figure 4.5 we report the two-dimensional spectra of PSP versus the light output in keVee for the commercial standard EJ-212 and for three 1" size samples with increasing PPO concentration. The capability of the siloxane-based samples to discriminate different particles is evident, also for low PPO concentrations. On the other hand, EJ-212 does not show a clear distinction between fast neutrons and photons, confirming the intrinsic inefficiency of this plastic scintillator for particles discrimination.

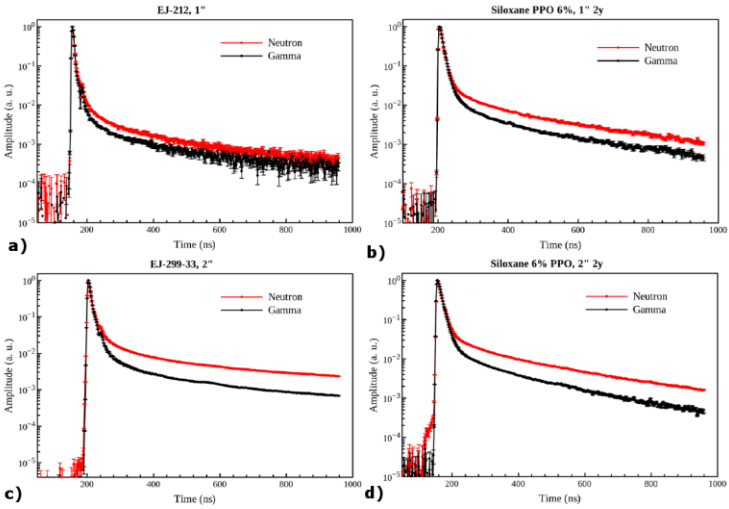

Figure 4.4: Scintillation pulses normalized on the pulse height obtained by averaging off-line waveforms for (a) 1" EJ-212; (b) 1" PMPS 6 wt.% PPO 2y; (c) 2" EJ-299-33 and (d) 2" PMPS 6 wt.% PPO 2y.

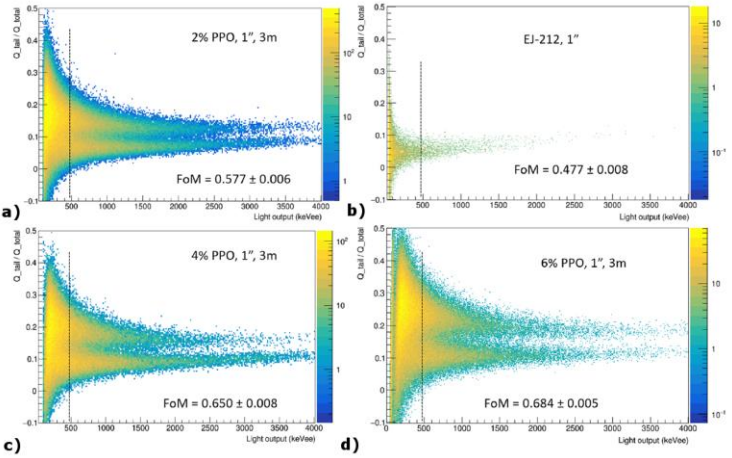

Figure 4.5: Two dimensional plots of PSP versus light output for the 1" samples (aged 3m) with different PPO concentration and of EJ-212 under irradiation with Pb shielded ^{252}Cf source; the evaluated FoM at the threshold 480 ± 75 keVee, shown in each plot as a dashed line, is also reported for each scintillator and listed in Table 4.3.

Sample	Size Ø (mm) × h (mm)	Volume (cm^3)	FoM
EJ-212	25.4 × 10	5.1	0.477±0.008
PMPS 2% PPO (3m)	25.4 × 10	5.1	0.577±0.006
PMPS 4% PPO (3m)	25.4 × 10	5.1	0.650±0.008
PMPS 6% PPO (3m)	25.4 × 10	5.1	0.684±0.005
EJ-299-33A	50 × 50	98	1.23±0.01
PMPS 2% PPO (2y)	50 × 54	86	0.36±0.01
PMPS 6% PPO (3m)	52 × 53	112	0.523±0.005
PMPS 6% PPO (2y)	50 × 44	86	0.611±0.005

Table 4.3: FoM values obtained using the parameters derived from PSP versus Light output plots at threshold 480 ± 75 keVee.

4.3.2.3 Time-of-flight measurements

The high performances of the siloxane scintillators in their PSD capabilities can be even more appreciated with 2" samples, whose PSP vs light output is reported in Figure 4.6(a, b, c). Exploiting the Time-Of-Flight (TOF) discrimination, γ-rays and fast neutrons are represented as blue and red dots, respectively, in the PSP vs light output plots. Figure 4.6(d, e, f) reports the scatterplot of PSP vs TOF, highlighting the correlation between the PSP and TOF parameters. In these plots, the two loci are assigned to γ-rays, lower TOF values, and neutrons, higher TOF values. The flat horizontal distribution is due to uncorrelated background events. It is worth noticing that for the standard plastic scintillator for n-γ discrimination, EJ-299-33, the PSP region with values higher than 0.15 can be assigned to neutrons and the events induced by γ-rays in this range are limited to a small fraction. Regarding the 2" PMPS scintillator with 2 wt.% PPO, it does not show a clear distinction in PSP for different particles, indicating a very low discrimination on the basis of the sole PSP. On the other hand, the sample containing 6 wt.% PPO shows good discrimination capabilities: the maximum of γ-rays induced events is centred at PSP=0.15 and the neutron ones at PSP=0.22. Furthermore, misclassification of the particles is limited as demonstrated by the TOF fingerprint of neutrons and γ-rays associated with PSP, where a clearer separation is observed for this scintillator, although not as good as for EJ-299-33.
Concerning the FoM values reported in Table 4.3 for both 1" (Figure 4.5) and 2" (Figure 4.6) scintillators, small detectors show enhanced FoM for the same energy values than the larger ones, as already reported in literature [96,97]. Together with a lower light yield, as previously reported, larger samples present a broader spread of the statistical distribution of detected scintillation photons as a function of time due to a wider distribution of paths and a higher number of reflections before reaching the PMT. These effects lead to a broadening in the PSP distribution and, in turn, to lower values of FoM for a given threshold energy. Regarding the ageing study, samples with

different ages show negligible variation in their PSD capabilities, as can be observed in Figure 4.7 and Table 4.3.

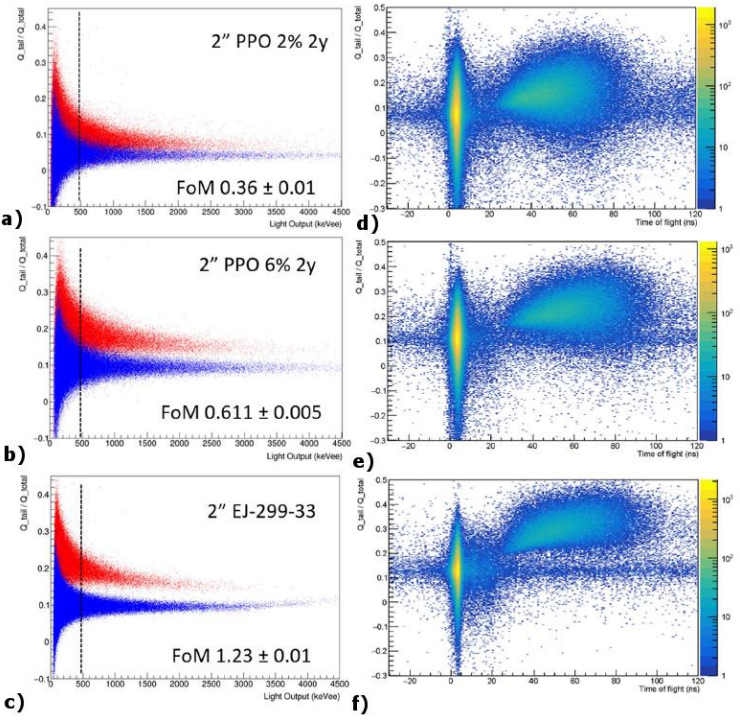

Figure 4.6: 2D plots reporting the PSP vs light output (left panel), with γ-rays and fast neutrons events labelled as blue and red dots, respectively. Scatter plots of PSP vs TOF (right panel), showing the distribution of γ-rays, fast neutrons and uncorrelated background events. The FoM estimated for each sample at 480 ± 75 keVee is also reported.

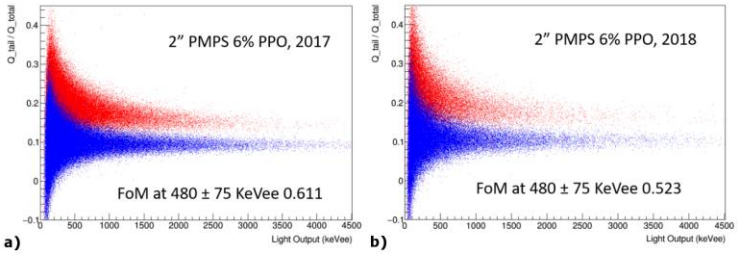

Figure 4.7: Two-dimensional plot of the PSP versus light output for two samples with the same composition but different age of production: (a) 2017 and (b) 2018. The FoM at the indicated threshold (480 keVee) is almost the same and the slightly better performance shown by the oldest sample can be associated to the smaller size and higher light yield of this scintillator, as indicated in Table 4.2.

4.4 Summary

In summary, the scintillation response of PMPS samples synthesized with concentrations of PPO as primary dye ranging from 1 to 8 wt.% and a fixed amount of waveshifter was presented, demonstrating the capability of these scintillators to discriminate between fast neutrons and γ-rays. This feature is related to the mechanism of TTA, which leads to delayed fluorescence and, in turn, to a longer decay time of the scintillation pulse for those particles having higher ionization density, such as recoil protons from impinging neutrons. To enhance TTA, one should promote either the diffusion and mobility or the closeness of triplet states induced in primary dye molecules. A locally high concentration of triplet states of primary dye can be achieved in aromatic polymers, such as PS or PVT, by adding a high amount of PPO, although remaining below the solubility limit. However, the possibility to improve the local concentration of triplet states of PPO molecules by avoiding overloading the polymer itself is very attractive, since it implies that the perturbation of the intrinsic properties of the matrix is minimized and the mechanical and optical stability over time are pursued. In PMPS, the torsional freedom of the Si-O-Si bond leads to the formation of stacks of lateral phenyl groups, with strong affinity towards the PPO molecule. Therefore, by exploiting the presence along the chain of PMPS of dyads of phenyl rings, it is possible to favour the aggregation of PPO molecules in these sites, keeping the overall concentration relatively low. The aggregation of PPO was demonstrated by the formation of excimers, as indicated by the fluorescence measurements. In scintillation, the closeness of PPO molecules makes possible the distinction of fast neutrons over γ-rays, owing to the TTA mechanism, giving rise to a variation in the shape of the scintillation light pulse according to the different ionization density of the particle. Samples with PPO as low as 6 wt.% show good n-γ discrimination capabilities,

as compared with commercial plastic scintillator EJ-299-33. Moreover, preservation of their light output and discrimination capability over long periods of time was demonstrated. Optical transparency, flexibility and high light response are ascribed to the minimal perturbation induced by the dissolved additives, whose amount is low enough to preserve all the functional properties of the matrix. This type of scintillators can have applications in environments where important mechanical stress occurs during the measurements and soft and flexible materials can therefore offer outstanding advantages. Moreover, the higher thermal resistance of polysiloxane can be exploited to produce scintillators capable to tolerate thermal gradients.

Chapter 5 - Polysiloxane-based hybrid scintillators for thermal neutron detection

Part of this chapter has been published in:

S.M. Carturan, M. Vesco, I. Bonesso, A. Quaranta, G. Maggioni, L. Stevanato, E. Zanazzi, T. Marchi, M. Cinausero, F. Gramegna, *"Siloxane-based ^{6}LiF composites for flexible thermal neutron detectors with high efficiency: effects of ^{6}LiF crystals size and dispersion homogeneity"*, Nuclear Inst. and Methods in Physics Research A, 925 (2019) 109–115.

In this chapter we report the study and characterization of polysiloxane scintillators embedding ZnS:Ag powder and ^{6}LiF crystals, for the detection of thermal neutrons. Since the neutron detection capabilities depend on the ^{6}LiF crystal size, crystal dispersion and type of polysiloxane, the samples will be investigated by changing these variables. Firstly, the optical and morphological characterization of the samples will be performed. Then, their scintillation response will be investigated and related with the optical and morphological features. Results will be compared with those of state-of-the-art plastic scintillators.

5.1 Introduction

As already introduced, commercial solid scintillators for thermal neutron detection are typically based on thin plates of ZnS activated with Ag (ZnS:Ag) mixed with ^{6}LiF powder. Largely used detectors of this type are EJ-426/EJ-420 (Eljen Technology, USA) and BC-704 (Saint Gobain, France). As reported in subsection 1.4.1, we recall that the ^{6}Li nucleus is sensitive to thermal neutrons through the following capture reaction:

$$^{6}_{3}Li + n \rightarrow {}^{3}_{1}H\ (2.73\ MeV) + \alpha\ (2.05\ MeV)$$

After leaving ^{6}LiF crystals, the generated particles impinge on the ZnS:Ag powder, giving rise to the production of scintillation light. Since the generated particles have a maximum range of about 30 μm (triton) and 6 μm (alpha particle) inside ^{6}LiF, as calculated by SRIM [70], the size of the ^{6}LiF crystals is a critical parameter for the detector performance: the smaller the crystal size, the lower the energy loss, the higher the energy released into the scintillator and, in turn, the higher the final light output. The ZnS:Ag and ^{6}LiF mixed powders are usually dispersed within a plastic binder,

acting barely as a support. The dispersion homogeneity of ^{6}LiF crystals between phosphor grains is another crucial parameter to optimize the collection of secondary particles by the scintillator and to minimize light scattering and re-absorption phenomena. Lastly, the overall layer has to be very thin, in order to minimize γ-rays sensitivity and light loss induced by opacity. However, a high amount of powder dispersed in the binder is needed to get maximum detection efficiency, which is around 30% for thermal neutrons on EJ-426 and 55% on EJ-420 [98,99]. In the case of self-supporting layers, the detector appears as an off-white, opaque composite, rigid and fragile. Most frequently, the layer is deposited on a plastic transparent support, which acts also as a light guide, to be coupled with the photomultiplier tube (PMT) window. So, the commercial thermal neutron scintillators are not easy to handle and care must be adopted in the manipulation of these screens, in order to avoid the development of cracks upon bending and/or under exposure to vibrations. Another critical issue for commercial thermal neutron detectors is their low heat resistance, which prevents their use in environments where the temperature is higher than in normal conditions, as for example in applications related to oil well logging [100].

The possibility to produce flexible, thermally resistant and easy to handle detectors for thermal neutrons is here explored, by synthesizing ^{6}LiF crystals by co-precipitation method [64], mixing them with ZnS:Ag commercial phosphor powder and embedding the final mixture in polysiloxane. The preparation of ^{6}LiF nanocrystal through different approaches has been previously attempted to obtain transparent composites, in order to exploit the good light output and radiation hardness of siloxane-based scintillators doped with suitable fluorophores [2,3,43]. However, the lack of solubility of ^{6}Li complexes led to severe loss of light output. Here, ^{6}LiF nanocrystals are mixed with ZnS:Ag in tenths of mm thin layer of polysiloxane. The size of ^{6}LiF crystals is changed in order to investigate the size effects and optimize the final performances. In addition, two base siloxane matrices either with methyl substituents only or with pendant phenyl groups are used, in order to investigate both energy transfer effects in case of fluorescent polymer and the role of the polymer structure in the dispersion homogeneity of the inorganic components. Lastly, the light yield under thermal neutrons is measured and it is correlated both to dimensions and dispersion of ^{6}LiF crystals and to the polysiloxane properties. The response to γ-rays is also evaluated in order to check the background sensitivity of the composite scintillators. As a result, flexible and resistant composite scintillators are obtained with a sensitivity to thermal neutrons which is about 90% that of the commercial analogue EJ-426.

5.2 Experimental section

^{6}LiF crystals were prepared as reported in subsection 3.3 with four different crystallite sizes, therefore dissolving the ^{6}LiCl white salt in different ratios of water:ethanol

(W:EtOH) mixture, namely 1:0, 1:1, 1:3, 0:1. ^{6}LiF powder was mixed with ZnS:Ag (EJ-600, purchased from Eljen Technology) in the weight ratio of 1:3. Two vinyl terminated siloxane resins were use, PSS-22 and DMS-V21, whose chemical formulas are reported in subsection 3.1.3. The solid content in each composite was fixed at 70 wt.% with the remaining 30 wt.% composed by viscous resin. Self-supporting flexible disks of 2" diameter and thickness ranging from 280 up to 350 μm were produced, as can be seen in Figure 5.1, where the picture of a representative sample is reported. Considering the amount of used ^{6}LiF and thickness of our disks, we can calculate the content of ^{6}Li in our scintillator as being around 2.6 mg/cm^{2}. Standard scintillators used to compare the microstructure and the thermal neutron response of the produced scintillators were purchased from Eljen Technology. The 1" disk of EJ-426 is composed of a 250 μm thick composite layer (^{6}LiF, EJ-600 and a binder) and a 250 μm thick supporting polyester layer [99]. The 2" disk of EJ-420 is 6.4 mm thick and it is composed of a transparent plastic disk with surface circular grooves containing the scintillating mixture ^{6}LiF/EJ-600, covered with a top layer of aluminium [99].
The morphology of the synthesized ^{6}LiF powders and the cross section of the obtained composites were investigated by Scanning Electron Microscopy (SEM-EDS, Tescan) equipped with a detector for backscattered electrons (BSE) and EDS probe (EDAX) for elemental analyses. Steady-state fluorescence measurements were acquired with the Jasco FP-6300 spectrofluorometer (subsection 3.6.1.2). The response to thermal neutrons was tested with a ^{252}Cf source, shielded with 6 cm of polyethylene bricks and placed at 30 cm distance from the front face of the detector. For further information on the scintillation measurements, we refer to subsection 3.6.2.

Figure 5.1: Picture of a flexible composite disk.

5.3 Results and discussion

5.3.1 Morphological characterization

Figure 5.2 shows the SEM images of ^{6}LiF powders synthesized with different W:EtOH volume ratios. The effect of ethanol as a co-solvent, in which ^{6}LiF has limited solubility, is clearly evident: in pure water (Figure 5.2(a)) the crystal growth is quite irregular, with

formation of acicular structures and incomplete cubic crystals very widely distributed in size, ranging from few μm up to tens of μm. As ethanol is added, the most evident effect is the decrease on average of the crystals size, as can be seen in (Figure 5.2(b) and (c): the average size decreases to less than 10 μm for the 1:1 W:EtOH volume ratio and even to less than 1 μm for the 1:3 ratio. On the other hand, the crystal growth is more regular leading to a narrower distribution in size of regularly shaped cubic crystals. For the synthesis in ethanol only, quite small and regular crystals are produced, with size of few hundreds of nm (Figure 5.2(d)).

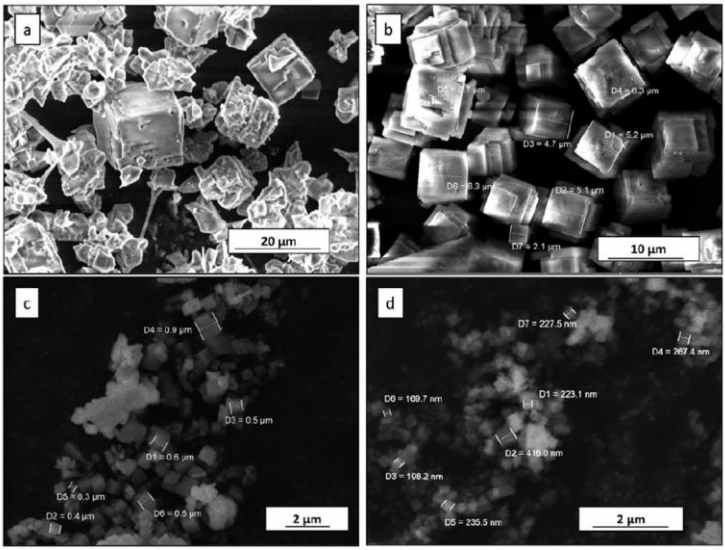

Figure 5.2: SEM images of ^{6}LiF powders synthesized with different W:EtOH volume ratios: (a) 1:0; (b) 1:1; (c) 1:3; (d) 0:1. The dimensions of some crystals are reported in the figures.

The precipitation in mixtures of solvents with different polarizability and hydrogen bonding capability is a technique which exploits the variation in solubility of both the reactants and the products for the crystal size control. While LiCl is highly soluble both in water and in ethanol, NH_4F is moderately soluble in ethanol, therefore the dissolution of NH_4F and formation of solvated F^- ions in ethanol/water solvent mixtures is the critical step in controlling the LiF crystal growth [101]. At the early stages of nucleation, the crystal seeds are surrounded by solvated ions, Li^+ and F^-, which are attracted toward the core and the crystal grows until the solubility of LiF in that solvent is reached. In pure water, the solubility and the dissociation of the reagents forming solvated ions is the highest, hence crystal growth rate is high and large crystals are

formed, with broad size distribution. When ethanol is added, the solubility of NH_4F decreases, and the small core crystal, surrounded by a large amount of non-dissociated molecules, attracts the few F^- ions in the neighbours. As the crystal grows, the concentration of solvated F^- ions decreases, thus promoting further dissociation of NH_4F and reaction progress. In these conditions, the growth is slow and steady, producing crystals with decreasing size as the ethanol fraction increases, until the nm range is reached for pure ethanol (Figure 5.2(d)).
Figure 5.3 shows the SEM images of the composites cross-section obtained by mixing the different ^6LiF powders with EJ-600 in weight ratio 1:3 and using PSS-22 as a binder (30 wt.%).

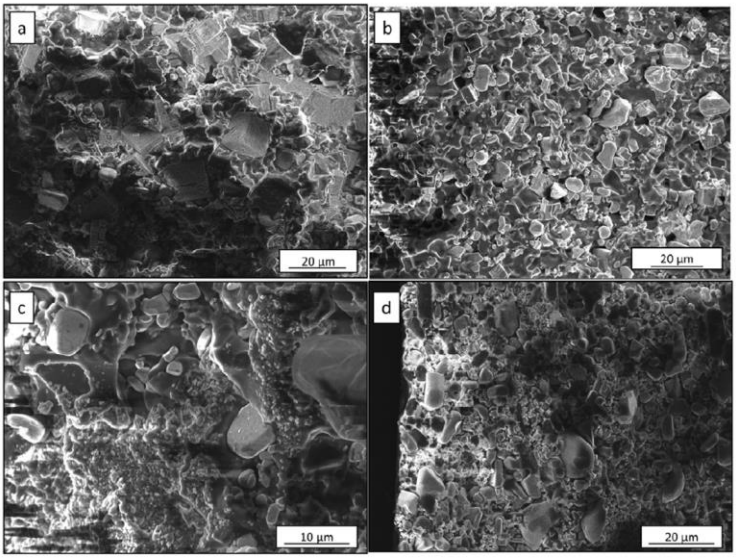

Figure 5.3: SEM cross-section images of the PSS-22 composites with ^6LiF crystal obtained from (a) pure water, (b) W:EtOH 1:1, (c) pure EtOH and (d) EJ-426.

The cross-section of the commercial detector EJ-426 is also shown for comparison (Figure 5.3(d)). The dispersion degree of EJ-600, appearing as roundly-shaped micron sized grains in a quite broad range of dimensions, the cubic crystals of ^6LiF and the siloxane resin can be observed in the different cases. For the composite obtained with crystals precipitated in pure water (Figure 5.3(a)), the large size cubic grains mostly appear as agglomerates, with size in the order of tens of µm, surrounded by resin and phosphor grains. In the case of crystals precipitated from W:EtOH 1:1 volume ratio (Figure 5.3(b)), an optimal level of dispersion of the inorganic components within the

organic matrix can be observed. The cubic crystals and the phosphor grains are finely distributed and only few agglomerates larger than some microns are visible. On the other hand, for the sample with crystals some hundreds of nm in size (W:EtOH 0:1 in Figure 5.3(c)), the tiny cubes are highly agglomerated in islands tens of μm wide, and surrounded by the resin, whereas the EJ-600 lumps are visible as clusters of grains several μm far from ^{6}LiF agglomerates. A rather unsatisfactory performance of this latter detector is expected because of the observed microstructure: as previously discussed the charged particles arising from neutron capture events have a range of 30 μm at maximum, hence the energy fraction released into EJ-600 grains, which are several microns far apart, is quite low. Moreover, the aggregation of EJ-600 can cause reabsorption of the emitted light, with a remarkable light output loss. It is worth to observe the microstructure of EJ-426 cross-section in Figure 5.3(d), where optimal dispersion of the components is present and the crystals of ^{6}LiF appear smaller on average than those synthesized by W:EtOH 1:1. Thus, it can be inferred that physical interaction between the ions escaping from the crystal after neutron capture and the scintillator grains is quite effective. In the case of DMS-V21 based composites, the inhomogeneous dispersion is already visible in the W:EtOH 1:1 samples, as can be observed from BSE images reported in Figure 5.4, where DMS-V21 and PSS-22 samples with average micron size ^{6}LiF crystals are compared.

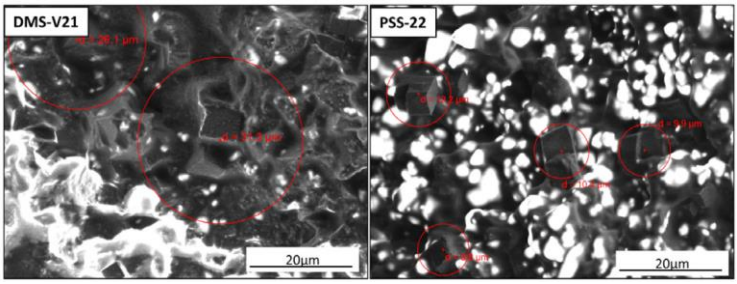

Figure 5.4: BSE images of DMS-V21 based (left) and PSS-22 based (right) derived composites cross-section. Both samples contain ^{6}LiF crystals synthesized in 1:1 W:EtOH volume ratio.

The detection of backscattered electrons allows to observe the remarkable difference in the dispersion homogeneity in the two different resins, as can be seen from the contrast between ^{6}LiF, visible as cubic shaped, dark crystals, and EJ-600 (ZnS:Ag), visible as bright grains. It is worth to observe that in PSS-22 the scintillator is finely distributed around the cubic crystals, whereas the use of DMS-V21 causes the formation of aggregates. Several different spots were investigated by BSE and this scenario was found almost everywhere along the cross-section of the samples. It can

be envisaged that in the case of PSS-22 the close proximity of the cubic grains, emitting ionizing particles, to the luminescent centres and, most importantly, the fine distribution of these components leads to a higher light output if compared with DMS-V21. In the latter, the aggregation either of ^{6}LiF or of EJ-600 causes, on one hand, the possibility that the ionizing particles are stopped into the crystals cluster before reaching the scintillator, on the other hand, that light emitted from EJ-600 can be re-absorbed, thus leading to light emission loss. The reason for the different morphology of the composites as the base resin is changed is ascribed to the polarizability of the resin itself: in the case of phenyl containing polysiloxane, the dipole-induced ion interaction of the delocalized π electrons with surface ions, either of the LiF crystal or the EJ-600 compound, results in the stabilization of the two phases, organic and inorganic, in a way similar to solvation [102]. For very small LiF crystals, as those obtained in pure ethanol, the strength of the interaction is not enough to prevent agglomeration, thus the phase separation observed in Figure 5.3(c) arises.

5.3.2 Optical measurements

Aiming at investigating the role of the polysiloxane matrix in the scintillation yield, a photoluminescence (PL) analysis, reported in Figure 5.5(a), was performed on both the pure resins and on composites obtained by mixing the resin with 5 wt.% of EJ-600.

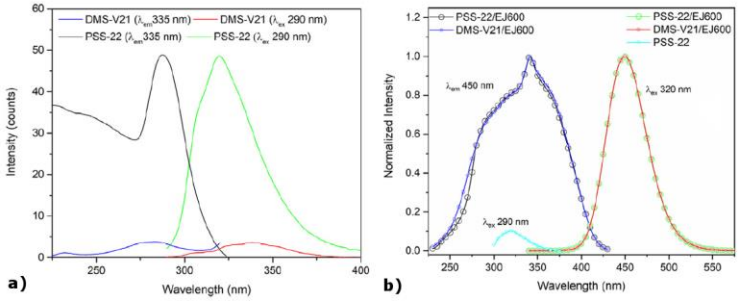

Figure 5.5: Excitation and emission spectra collected from (a) the pure resins and (b) from the resins with 5 wt.% of EJ-600. The emission spectrum of pure PSS-22 is added in (b) with intensity scaled to the normalized value of the composite for comparison purposes.

In fact, the secondary particles emitted from the LiF crystals can give rise to a further luminescence emission from the polymer matrix which, as absorbed by the phosphor crystals, could give an additional contribution to the final scintillation yield. From the emission and excitation spectra reported in Figure 5.5(a), it can be observed that DMS-V21 shows a negligible luminescence yield, as could be expected on the basis of its

chemical structure where phenyl groups are absent. On the other hand, PSS-22 shows intrinsic florescence under excitation at 280 nm, as previously reported in literature [2], with an emission peak centred around 320 nm. The PL spectra of EJ-600, shown in Figure 5.5(b), show a broad excitation band ranging between 250 and 400 nm, and an emission band centred at 450 nm, as coherently reported in the literature in a study investigating the electronic structure of luminescence center of ZnS:Ag phosphors [103]. The shape and intensity of the EJ-600 features in the two binders are very similar. The only appreciable difference is related to the excitation band of EJ-600 dispersed in PSS-22, which shows an inflection point in the UV region in correspondence of the excitation spectrum of the binder. This effect can be associated to self-absorption effects induced by the phenyl groups of the polymer. In any case, the light emission from EJ-600 is very intense, as visible in Figure 5.5(b) where the pure PSS-22 resin spectrum is reported with its relative intensity, that energy transfer effects from the intrinsically fluorescent matrix are not evidenced in this kind of analysis. Nonetheless, absorption processes of the light emitted by the matrix giving rise to secondary luminescence from the phosphor cannot be totally discarded at present.

5.3.3 Scintillation measurements

5.3.3.1 Thermal neutron response

In order to investigate the thermal neutron sensitivity of the produced composites, the scintillation pulses have been analysed through the method reported in subsection 3.6.2.2. Thermal neutron signals are characterized by higher values of Pulse Shape Parameter (PSP) with respect to background noise or γ-rays. In Figure 5.6 the time evolution of the pulse intensity related to the detection of thermal neutron from a moderated ^{252}Cf source for the EJ-420 sample is reported. It is worth observing that the long tail of the falling part of the signal is extending well beyond 1 μs. This particular feature of the pulse shape is related to the excitation density of the ions coming from the neutron capture event, namely triton and alpha. The high local energy deposited by the ions into the EJ-600 scintillator produces a high density of excited states, whose interaction slows down the decay to the ground state, giving rise to a longer lifetime than in case of irradiation with photons. In fact, the detection of γ-rays occurs through scattered electrons, producing a much lower excitation density along the path and giving rise to much shorter scintillation decay, in the order of hundreds of ns as previously observed in the literature [104,105]. In Figure 5.6 the widths of the integration gates for PSP are also reported. In particular, the Q_{fast} (Q_{short}) width was set to 80 ns and the Q_{tail} one to 1420 ns. The integration width for Q_{fast} starts 40 ns before the overcome of the acquisition threshold, that in the present case was set to

15 mV. In Figure 5.6(b) the plot of PSP versus Q_{total} is reported for the same sample, exposed to the moderated ^{252}Cf source for 30 min. For signals with amplitude just above the threshold, such as γ-rays from the source and from the background, the definition of the PSP parameter gives rise to the noise stripe at very low Q_{total}. For this kind of events (low Q_{total}), the PSP spread is produced by the baseline fluctuations in the time window where Q_{tail} is calculated.

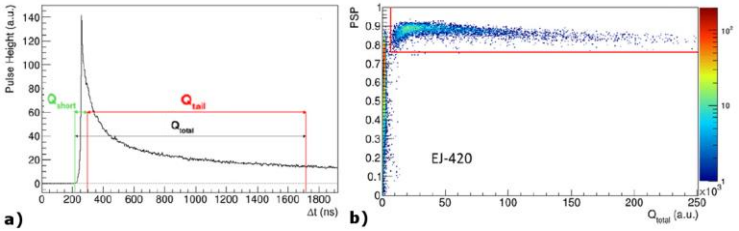

Figure 5.6: (a) The average signal as pulse intensity versus time collected from the commercial thermal neutron detector EJ-420; (b) PSP plot of EJ-420 versus total integration charge (Q_{total}) when exposed to ^{252}Cf source shielded with 6 cm of polyethylene (red lines highlight the region of events ascribed to thermal neutrons). The colour scale indicates the counts.

Thermal neutrons detection efficiency is defined as the ratio between the number of thermal neutron induced events on the detector and the number of impinging thermal neutrons, hence several parameters should be considered besides the source activity, such as the thickness of the moderator, the distance from the source, the solid angle of the detector and the signal-to-noise ratio.

In this experiment, we calculated the relative efficiency of our samples with respect to the commercial standard EJ-420, whose efficiency to thermal neutrons is evaluated as about 55% by the supplier. This relative efficiency was evaluated by counting the neutrons-induced events identified by PSD method in a defined acquisition time interval and in a given detector-source configuration, once the best condition (i.e. acquisition threshold, signal-to-noise rejection, signal integration gates) for signal processing were properly set. The ratio between the thermal neutron counts in different samples with respect to the counts in the standard EJ-420 define our ''relative efficiency''.

As illustrated in Figure 5.6(b) for the EJ-420 standard, a further software gate in the PSP-Q_{total} plane ($Q_{total} > 7 \times 10^3$ and $0.76 < PSP < 1.00$) was set for the final selection of thermal neutron induced events and reject others in the background. The 2D plot of PSP-Q_{total} plots for each sample are shown in the panels of Figure 5.7. The relative efficiency with respect to EJ-420 is reported in Figure 5.8(a) as a function of the W:EtOH volume ratio.

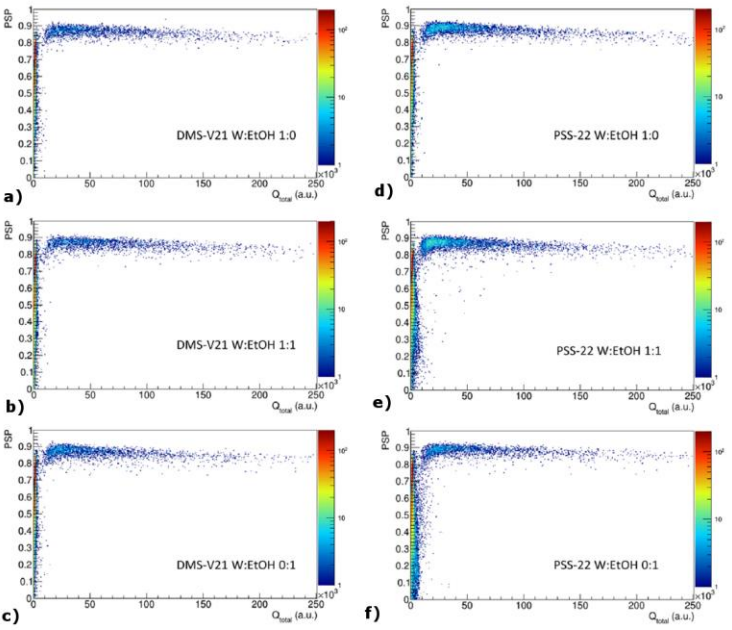

Figure 5.7: PSP plots versus Q_{total} of the produced scintillators with different average size crystal (decreasing from top to bottom) and different siloxane resins (DMS-V21 on the left column, PSS-22 on the right column). The colour scale indicates the counts.

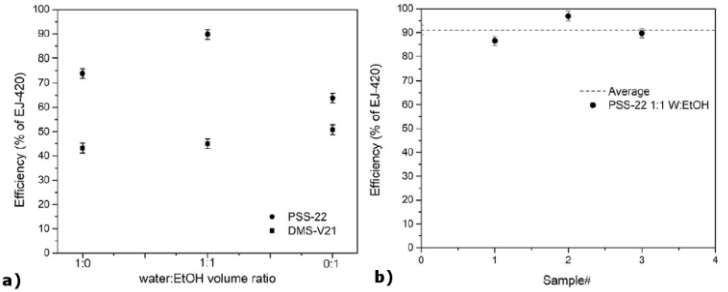

Figure 5.8: Thermal neutron detection efficiency relative to EJ-420 of the produced composites either with PSS-22 or DMS-V21 as a function of the volume fraction of ethanol in the synthesis of ^{6}LiF crystals (a) and average value of efficiency of three disks prepared in the same way (b). The error bars were calculated from the dispersions of four independent measurements on the same sample.

First of all, a remarkable difference in the response between the samples produced with PSS-22 rather than DMS-V21 can be clearly observed. This behaviour was expected from the different distribution evidenced by BSE images, where PSS-22 based composites proved to be more homogeneous in the distribution of ^{6}LiF cubic crystals and EJ-600 grains. Moreover, a trend can be noticed within the set of PSS-22 samples as regarding the ^{6}LiF crystals size: both large size (1:0 W:EtOH ratio) and small size (0:1 W:EtOH ratio) crystals show a lower efficiency with respect to samples containing crystals derived from 1:1 W:EtOH ratio. In the case of smaller crystals, with size of hundreds of nm on average, this is due to the bad dispersion of the powders in the resin as reported in the SEM images of Figure 5.3, where the agglomeration of the small cubes in large clusters with size in the order of some microns is clearly observed. In this case, the interaction between the ions produced from capture reactions and the EJ-600 grains is definitely less likely to occur. The same detrimental effect arises in the case of the composite with large crystals, such as ^{6}LiF cubes of tens of μm obtained in pure water as solvent, owing to the long path for the reaction products to exit the crystal and hit EJ-600 grain. The best result has been achieved with PSS-22 as base resin, 1:1 W:EtOH ratio for ^{6}LiF, reaching 96% of efficiency with respect to EJ-420, as can be observed in Figure 5.8(a). The data reported are the average result of four independent measurements obtained by removing the sample, cleaning the PMT glass window and repeating all the procedure to acquire the measurement, as described previously.

In order to test for the reproducibility of the experimental approach in producing the thermal neutron sensor, three different disks have been prepared using the same synthesis method, i.e. keeping constant the mixing ratio EJ-600: ^{6}LiF, the resin % volume, cross-linking conditions and final thickness. Then, each disk was tested under irradiation with thermal neutrons and the average relative efficiency value of 90 ± 6% was evaluated from the test as reported in Figure 5.8(b), leading to the conclusion that the preparation procedure has optimal reproducibility, owing to the great accuracy in controlling each synthesis step.

5.3.3.2 Sensitivity to γ-rays

The quite low thickness of the prepared scintillators should lead to limited sensitivity to γ-rays, which mainly interact with atomic electrons by Compton scattering (100 keV < Eγ < 1 MeV). Nevertheless, the evaluation of the sensitivity to γ-rays is an important issue to assess the reliability of the detector, since the release of neutrons is often accompanied by γ-rays, leading to spurious signals. In Figure 5.9 the pulse height spectra obtained by exposing the standard EJ-420 and the best performing PSS-22 disk to the moderated ^{252}Cf source are reported. The spectra are the projection on the x-axis of the bi-dimensional plots PSP versus Q_{total} shown in Figure 5.6(b) and in

Figure 5.7. The different contributions are separated on the basis of the selection window previously indicated in Figure 5.6(b), as for both total charge and PSP, hence thermal neutrons are unambiguously identified by their high value of PSP [104]. Nonetheless, the possibility that also other interactions, such as background radiation or electronic noise, contribute to the spectrum cannot be excluded. Therefore, the sensitivity towards γ-rays was tested by exposing the sample to a ^{137}Cs source, emitting γ-rays of 0.662 MeV.

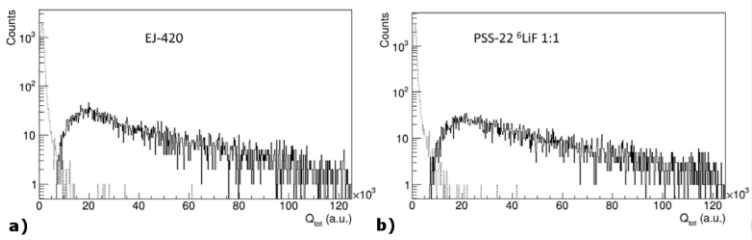

Figure 5.9: Pulse height spectra versus Q_{total} showing the different contribution of γ-rays and background radiation (dotted line) and thermal neutrons (continuous line) for (a) the standard EJ-420 and (b) the best flexible thermal neutron detector herein produced upon irradiation with moderated ^{252}Cf source.

The same experimental conditions, such as source position, distance of the sample from the source and acquisition time were kept constant for every disk under test, thus the solid angle has been evaluated as follows:

$$\Delta\Omega = 2\pi\left(1 - \frac{d}{\sqrt{(d^2 + r^2)}}\right) \tag{5.1}$$

where d is the distance (10 cm) between the source and the detector surface and R the disk radius (1"). Hence, knowing the source activity and the solid angle $\Delta\Omega$, the γ-rays flux from the source was estimated. Then, the sensitivity is defined as the ratio between the total counts recorded by the PMT at a certain threshold voltage for a defined acquisition time and the γ-rays that actually hit the detector.

The sensitivity for EJ-420 and the PSS-22 based disks versus the signal threshold for acquisition is reported in Figure 5.10. The most evident result is that the response is remarkably higher for PSS-22 with respect to EJ-420 and for a signal threshold of about 17 mV the difference is one order of magnitude, being 2×10^{-4} for EJ-420 and 2×10^{-3} for PSS-22. This behaviour can be ascribed to the intrinsic difference between the two sensors: the thickness of the scintillating composite layer deposited on the grooves of EJ-420 is not known from the manufacturer, but the areal density of ^{6}Li is

declared as 9 mg/cm^2 [99], whereas in our scintillator is around 2.6 mg/cm^2, though similar neutron sensitivity was evidenced. This may indicate that light transmission through our scintillator is enhanced, thus explaining the higher sensitivity towards γ-rays. Anyway, the sensitivity to γ-rays of the PSS-22 based disk remains very low, therefore highlighting the optimal performance of this flexible composite as thermal neutron detector where interfering signals from γ-rays are negligible.

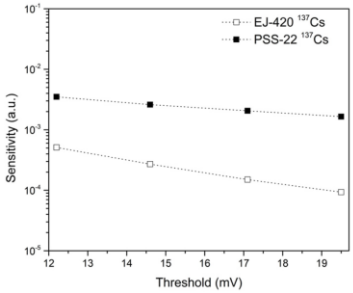

Figure 5.10: Sensitivity of the flexible thermal neutron detector based on PSS-22 towards γ-rays from ^{137}Cs source. The response of the standard EJ-420 in the same conditions is reported for comparison.

5.4 Summary

In summary, flexible and robust thermal neutron scintillation sensors were produced by mixing ZnS:Ag powder with ^{6}LiF nano-crystals in polysiloxane resins. The crystals were synthesized by a co-precipitation method and different crystal sizes ranging from hundreds of nm to tens of μm were obtained by varying the water to ethanol ratio in the solvent. Two polysiloxane resins, namely polydimethylsiloxane and polymethylphenylsiloxane, were tested as matrix. Different dispersions of the crystals were obtained depending on both the crystal dimension and the matrix. In particular, the samples with crystals size in the order of some μm (W:EtOH 1:1 volume ratio) in polymethylphenylsiloxane gave the best efficiency to thermal neutrons, reaching 90% of the commercial analogue, EJ-420. This result was related to the optimal dispersion of the ^{6}LiF crystals rather than to the luminescence contribution of the matrix. The γ-rays response of the scintillators is higher than EJ-420 but still very low and possible interference with the signal from thermal neutrons is negligible. The fabrication of this type of materials paves the way towards thermal neutron detection in extremely harsh environment, where resistance to high temperature and intense vibrations is crucial.

Chapter 6 - Sensitization of polysiloxane with colloidal quantum dots

Part of this chapter has been published in:

WILEY-VCH physica status solidi a applications and materials science ADVANCED SCIENCE NEWS www.advancedsciencenews.com

E. Zanazzi, M. Favaro, A. Ficorella, L. Pancheri, G. F. Dalla Betta, A. Quaranta, *"Real-Time Optical Response of Polysiloxane/Quantum Dot Nanocomposite under 2 MeV Proton Irradiation: Luminescence Enhancement of the Polysiloxane Emission through Quantum Dot Sensitization"*, Phys. Status Solidi A, 217 (2020) 1900586

In this chapter we report the study and characterization of polysiloxane samples embedding different concentrations of colloidal QDs, in order to evaluate the possible use of colloidal nanocrystals as energy acceptors in polysiloxane scintillators. Firstly, samples will be optically characterized in order to investigated the possible arising of energy transfer from the polymer matrix to the QDs. Then, the luminescence emission of the samples will be investigated in real-time under ionizing radiation (proton irradiation).

6.1 Introduction

As described in subsection 2.1.5, the use of colloidal QDs as sensitization material in organic scintillators has been already partially investigated, with the aim of increasing the scintillation yield under γ-rays. Among the studies reported in the literature, the most promising results have been obtained by Liu et al. [11] with a scintillator composed of $Cd_xZn_{1-x}S/ZnS$ QDs and FBtF dyes embedded in polyvinyltoluene (PVT). More specifically, the authors embedded a high amount of QDs (up to 60 wt.%) into the polymer matrix, exploiting an embedding procedure that assures a high transparency of the final sample. The working principle of the scintillator is therefore mainly based on the Förster resonance energy transfer (FRET) between the high-Z QDs (donor) and the FBtF dyes (acceptors). However, the authors do not exclude the possible arising of FRET between the PVT and the QDs (or the FBtF dyes), since the band-gap energy is decreasing from the PVT matrix (4.2 eV) to QDs (2.84 eV) and then to FBtF (2.56 eV). Anyway, thanks to the high stopping power offered by the inorganic nanocrystals, the γ-ray photopeak with 9.8% resolution was observed in the scintillation spectrum. With a different approach, in this chapter we investigate the possibility of exploiting colloidal nanocrystals as energy acceptors in polysiloxane. More specifically, colloidal nanocrystals dispersed at low concentrations should work as primary dyes, accepting the radiation-induced excitation within the matrix. In this context, no studies adopting this approach have been reported in the literature so far. However, as already mentioned, Liu et al. [11] indicated the possibility of having Förster energy transfer from the PVT matrix to the QDs. Similarly, Anni et al. [106]

reported the Förster energy transfer from a blue-emitting polymer, namely poly [(9,9-dihexylfluorenyl-2,7-diyl)-alt-co-(9,ethyl-3,6-carbazole)] (PDFC), to colloidal CdSe/ZnS QDs. On the other hand, however, Clapp et al. [107] demonstrated as colloidal QDs cannot be efficient energy acceptors with organic materials as donors, due to the difference in lifetime between donor and acceptor (lifetime of organics is typically shorter than those of QDs) and to excitation crosstalk (simultaneous excitation of donor and acceptor), as it will be later deepen. For these reasons, in general, the use of QDs as acceptors in non-radiative energy transfer processes has been reported to be more challenging than their use as donors [108]. In this context, the use of QDs as energy acceptors for the matrix, and therefore as final light emitters, would be of special interest in scintillators mainly because of the efficient, narrow and tuneable emission that these nanocrystals offer. In fact, especially the tuneable emission could potentially increase the versatility of the scintillators for what concern their efficient coupling with the wavelength of maximum sensitivity of the photodetector.

6.2 Experimental section

Samples were produced by starting from colloidal core-shell CdSe/ZnS QDs (stabilized with octadecylamine) with a declared emission wavelength of 540 ± 10 nm and dispersed in toluene (absorption and emission spectra are reported in subsection 3.4). QDs in solution were then dispersed in (14-18% diphenylsiloxane) - dimethylsiloxane silanol terminated copolymer (PSS-1418), whose chemical formula and preparation procedure are reported in subsections 3.1.3 and 3.5, respectively (drying at 60°C for 48 h was performed). Five PSS-based samples (5 mm thick) were prepared embedding QDs at the concentrations of 0.003, 0.015, 0.03, 0.3 and 1 wt.%. For comparison purposes, one undoped PSS sample was also prepared (Figure 6.1).

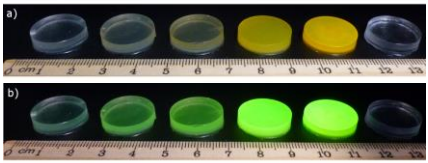

Figure 6.1: Picture of the samples under a) ambient light and b) UV light. From left to right: PSS embedding QDs at the concentrations of 0.003, 0.015, 0.03, 0.3 and 1 wt.%. respectively. The last sample on the right is the undoped polysiloxane.

The QD concentration in wt.% was calculated considering the effective mass of QDs added to the polymer in relation to the mass of the total polymer, the latter calculated from the total polymer volume approximating the density of the polymer to the density

of the main part (0.96 gr/cm^3). Aggregation of the nanocrystals were clearly visible at naked eye starting from 0.03 wt.% of QD concentration, with a significant loss of transparency. Moreover, above 0.03 wt.% a higher amount of nanocrystal was present at the bottom of the samples due to their precipitation during the 48 hours polymerization process. Optical characterization of the samples was performed by both steady-state and time-resolved PL measurements (subsection 3.6.1). IBIL measurements were carried out at the Legnaro National Laboratories (Padova, Italy) using the AN2000 Van de Graaff accelerator (subsection 3.6.3), with H^+ ions, beam spot size of 3×3 mm^2 and beam current of 40 nA, corresponding to a particle flux of 2.77×10^{12} $H^+cm^{-2}s^{-1}$. Sample irradiation lasted 195 sec and the luminescence spectra were acquired (in front-face geometry) every 1 sec with 1 sec of integration time, using the QE65000 portable spectrometer.

6.3 Results and discussion

6.3.1 Optical measurements

Figure 6.2(a) reports the excitation and emission spectra of pure PSS and of the QDs embedded in PSS.

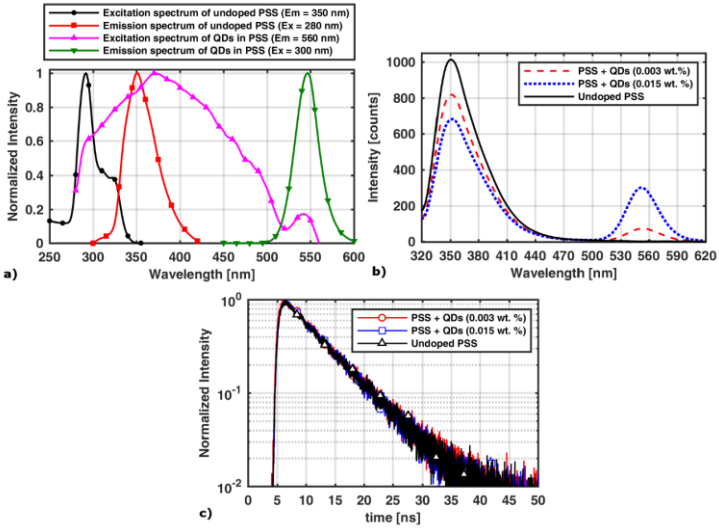

Figure 6.2: a) Excitation and emission spectra of undoped PSS and QDs in PSS; b) emission spectra of the samples acquired under 285 nm laser excitation and c) time-resolved PL curves of the samples acquired under 285 nm laser excitation at the emission of 350 nm.

As shown in Figure 6.2(a), the emission spectrum of PSS (peaked at 350 nm) overlays the excitation spectrum of the QDs, indicating the possibility of energy transfer phenomena between the polymer (donor) and the QDs (acceptor) [26]. Therefore, in order to deepen the phenomenon, emission spectra of the samples excited with the 285 nm laser source (corresponding to the excitation peak of the matrix) were acquired and reported in Figure 6.2(b). Here, it can be observed that the intensity of the PSS emission spectrum (at 350 nm) decreases with the increasing QD concentration (only the first two QD concentrations were considered, as it will be explained during the discussion). On the other hand, the emission intensity of the QDs (at 550 nm) also increases with the nanocrystal concentration. This behaviour is also in agreement with the occurrence of energy transfer phenomena between the polymer matrix (donor) and the QDs (acceptors). However, aiming at investigating the nature of the energy transfer, time-resolved measurements were acquired in order to probe the donor emission (at 350 nm) in the presence and in the absence of the potential acceptors (Figure 6.2(c)). In fact, if dealing with non-radiative (Förster's type) energy transfer, the donor lifetime in presence of the acceptor should be shorter in comparison with the donor lifetime in the absence of the acceptor [26]. However, Figure 6.2(c) shows no significant differences in the time decay curves. Although not reported, no differences were observed in the time-resolved measurements also in the other samples embedding QD at concentrations up to 1 wt.%. Therefore, the decrease in the PSS emission intensity and the simultaneous increase in the QD emission intensity is partially correlated with the arising of radiative energy transfer (RET), namely the photon emission by the matrix and the subsequent partial reabsorption by the QDs, which then emit at their emission wavelength. In fact, due to its inherent lower efficiency, RET does not affect the donor lifetime [109]. However, since with a 285 nm excitation there is also a probability to directly excite the QDs (Figure 6.2(a)), a partial contribution to the increasing intensity of the QD emission due to the larger quantity of nanocrystals cannot be discarded. Summarizing with the help of the simplifyed model reported in Figure 6.3, when a 285 nm photon interact with the sample, three different phenomena can occur. In the first case, as reported in Figure 6.3(a), the photon can excite the π electrons beloging to the aromatic groups of the polymer and the subsequent deexcitation of the excited molecule will give rise to the fluorescence emission at 350 nm. In the second case, reported in Figure 6.3(b), the 285 nm photon can excite a nanocrystal that will deexcite emitting at 550 nm. In the third case, as reported in Figure 6.3(c), the photon can excite the π electrons beloging to the aromatic groups of the polymer and the emitted photon can be subsequently absorbed by a QD, which it will then deexcite emitting at 550 nm. In order to comment the absence of non-radiative Förster's resonance energy transfer from the polysiloxane matrix to the QDs, we first ascertain that the most relevant studies reported in the literature on this topic are those proposed by Clapp et al. [107] and Anni et al. [106].

In this respect, Clapp et al. [107] investigated the use of luminescent CdSe/ZnS QDs as energy acceptors in FRET-based assays with organic dyes as energy donors, reporting no evidence of FRET between the dyes and QDs. The authors attributed these findings to an effective competition between the fast radiative decay channels of the donor dye and the slower nonradiative FRET decay pathways, due to a relatively longer exciton lifetime of the QD acceptor compared to that of the donor. Moreover, the authors also point out that, due to the broad excitation spectrum of QDs, the contribution of direct excitation of the QDs further decreases the probability of having FRET mechanisms. In the other study, Anni et al. [106] demonstrated the FRET from a blue-emitting polymer, namely poly [(9,9-dihexylfluorenyl-2,7-diyl)-alt-co-(9,ethyl-3,6-carbazole)], to colloidal CdSe/ZnS QDs. However, we observe as the excitation wavelength used by the authors (λ= 390nm) is outside the excitation band of the polymer, that ranges approximately between 400 and 600 nm [106]. In this framework, in our case we hypothesize, similarly to Clapp et al. [107], that the absence of FRET from the polysiloxane to QDs is attributed to the dominance of a fast radiative decay of the donor relative to a slow FRET decay rate. This is due to the longer exciton lifetime of the QD acceptor compared to that of the polymer, combined with substantial QD direct excitation.

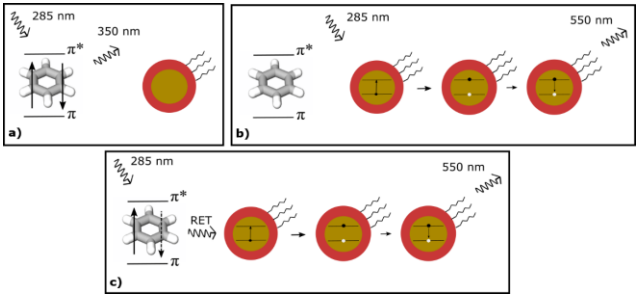

Figure 6.3: Simplified model describing the interaction of a 285 nm photon within the polysiloxane/QD nanocomposite; a) excitation of the polysiloxane molecule through the π orbital electrons of the aromatic group and the subsequent fluorescence emission; b) direct excitation of the QD with its subsequent deexcitation and fluorescence emission; c) excitation of the QD through the photon emitted by the polysiloxane molecule (RET) and subsequent fluorescence emission by the nanocrystal.

6.3.2 IBIL measurements

The proton-induced luminescence spectra of the samples after different irradiation fluences (exposure time) are reported in Figure 6.4(a) →(g). First of all, in Figure

6.4(a) → (c) we can observe the emission spectrum of the matrix located at 350 nm, in coherence with the optical measurements reported in Figure 6.2(a) and (b).

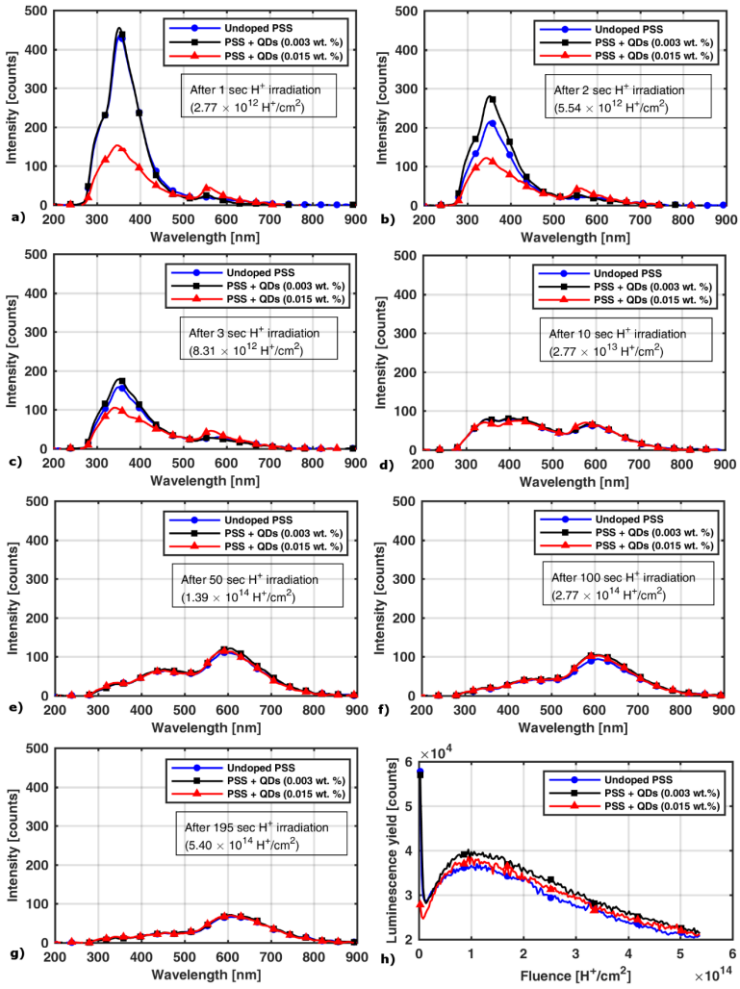

Figure 6.4: a)→g) Proton-induced luminescence spectra of the three samples after different irradiation fluences (exposure time); h) integrated luminescence yield (integral of the spectra) of the three samples plotted as a function of the irradiation fluence.

In fact, when a proton interacts with an organic aromatic material induces ionization and excitation events, which may involve both the π electrons of the aromatic groups

and also other electrons [1]. These ionization and excitation phenomena mainly occur indirectly, through the secondary electrons produced along the particle track [1]. However, in terms of luminescence spectra the behaviour of the system under proton irradiation gives the same features observed under UV irradiation, even if the excitation mechanisms are slightly different [1]. Regarding the QDs, as reported in Figure 6.4(a) → (c), a low-intensity peak around 550 nm can be observed in the spectra of the highest QD-concentrated sample (0.015 wt.%). On the other hand, no differences are observed at 550 nm between the spectra of the pure PSS and the spectra of the PSS embedding QDs at 0.003 wt.%. Although the entity of possible direct excitation (through protons) and indirect excitation (through secondary electrons) of the QDs need to be assessed, the small QD peak in Figure 6.4(a) → (c) is a further indication of the arising of RET phenomena also under proton irradiation, with the partial absorption by the QDs of photons emitted by the polymer matrix and the subsequent fluorescence emission by the nanocrystals. In fact, in the highest QD-concentrated sample, the intensity of the polymer emission at 350 nm remains, in the first seconds of irradiation, always lower than in the case of the other two samples (Figure 6.4(a) → (c)), consistently with the presence of RET. Considering the spectrum of the PSS embedding QDs at 0.003 wt. %, although no QD peak is observed, in the first seconds of irradiation (Figure 6.4(a) → (c)) the polymer band is always more intense than that of the undoped PSS sample. As regard the general evolution of the spectra, the first seconds of irradiation are characterized by an abrupt drop in the luminescence yield involving the polymer emission. Subsequently, as reported in Figure 6.4(c) → (g), a luminescence band arises between 550-600 nm, covering the QD emission peak. This luminescent feature, correlated with the formation of radiation-induced defects, has been already observed and discussed in our previous study [3]. In fact, proton irradiation on polysiloxanes may induces the formation of radicals and volatile products, which in turn become involved in chemical reactions resulting in cross-linking and scission events [3,110–112]. These phenomena may involve the cleavage of the (Si-O-Si) backbone of the polysiloxane molecule, affecting the optical properties of the polymer. Similar results have been also reported and discussed by Borjanovic et al. [112]. The authors performed PL measurements with a 488 nm laser source on polydimethylsiloxane irradiated by 2 MeV protons in the fluence range of 10^{13}-10^{15} cm^{-2}, observing the appearance of a luminescence band approximately in the range 500-650 nm. This band, although limited in intensity to few hundred counts and acquired with 5 minutes of integration time, increased in intensity with the irradiation fluence. This feature is ascribed by the authors to radiation-induced formation of defected silicon oxide, which may exhibit PL with emission peaks that vary according to the local structure of the defects [111,112]. By plotting the integral of each luminescence spectrum as a function of the irradiation fluence (Figure 6.4(h)), we can observe the light yield evolution of the three samples.

Moreover, by performing the integral of the curves reported in Figure 6.4(h) we can obtain the total light yield integrated to the entire irradiation time (Table 6.1).

QD concentration [wt.%]	Total luminescence yield [counts]	Luminescence yield increase [%]
0 (Undoped PSS)	5.6×10^6	/
0.003	6.0×10^6	8
0.015	5.7×10^6	3

Table 6.1: Total number of counts over the 195 sec irradiation time for the three samples and percentage increase of the light yield in comparison with the pure PSS sample.

As reported in Figure 6.4(h) and Table 6.1, both samples embedding QDs show a higher light yield in comparison with the undoped PSS. More specifically, the samples embedding QD at the concentrations of 0.003 wt.% and 0.015 wt.% show a light yield increase of 8% and 3% in comparison with the undoped PSS sample, respectively. Since the optical contribution of the QDs to the total emission can be considered from Figure 6.4(a) → (g) as negligible, the increasing light yield is correlated with the high-Z sensitization offered by the nanocrystals [23]. In fact, for γ irradiation it has been already demonstrated that the presence of inorganic nanocrystals within an organic polymer favour the conversion of the γ photons into photoelectrons, although the excitation events subsequently occur within the organic material [23].

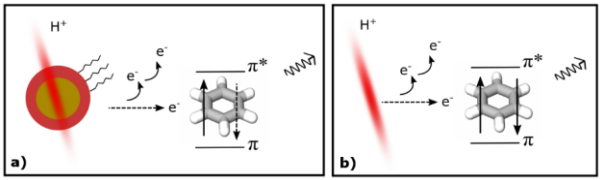

Figure 6.5: Simplified model describing the interaction of a proton within the polysiloxane/QD nanocomposite: a) excitation of the polymer mediated by a QD: the specific energy loss of the proton within the matrix is slightly increased thanks to the higher Z offered by the QD, and the excitation of the polymer is induced by the generated secondary electrons. b) Excitation of the polymer by secondary electrons generated by proton interactions directly within the matrix, without the involvement of a nanocrystal.

Similarly, in our case the presence of the nanocrystals slightly increases the specific energy loss experienced by protons, although the ionization and excitation events mainly occur within the polymer, giving rise to a slightly enhanced luminescence in comparison with the pure PSS (Figure 6.5(a)). Indeed, at these low QD concentrations it can be assumed that the proton interactions mainly occur within the polymer matrix, without the involvement of a QD. For this reason, the main contribution to the

polysiloxane emission probably remains the result of excitation events of the polymer itself by secondary electrons (Figure 6.5(b)). The increase of nanocrystal concentration, however, easily lead to QD aggregation, with the formation of scattering centers for the polymer photons and a decrease of sample transparency. This issue explains therefore the highest light yield observed in the lowest QD-concentrated sample.

6.4 Summary

In summary, the real-time optical investigation under 2 MeV protons of polysiloxane samples embedding QDs at different concentrations were reported. The optical characterization of the samples, in terms of time-resolved measurements, showed the absence of nonradiative Förster's resonance energy transfer (FRET) from the fluorescent polymer to the QDs, up to 1 wt.% of nanocrystal concentration. Similarly to what reported by Clapp et al. [107], we attribute the absence of FRET from the polysiloxane to QDs to the dominance of a fast radiative decay of the organic donor relative to a slow FRET decay rate. This is attributed to the longer exciton lifetime of the QD acceptor compared to that of the polysiloxane. Moreover, we observe as the excitation crosstalk (simultaneous excitation of both donor and acceptor) can further decrease the probability of having FRET mechanisms.
However, optical measurements indicated the possible arising of radiative energy transfer (RET), namely the absorption of a small fraction of the polymer photons by the QDs, which subsequently emit at their emission wavelength. The arising of RET is confirmed also under proton irradiation. However, since the entity of RET remains low, the main contribution to the proton-induced luminescence of the samples is given by the polysiloxane emission, since the nanocrystals do not contribute significantly to the total light yield. Nonetheless, the presence of nanocrystals dispersed at a very low concentration (0.003 wt.%) increased the total light yield (integrated over the entire irradiation time) of the samples up to 8% in comparison with the undoped polymer. This phenomenon is ascribed to the increased specific energy loss experienced by protons due to the presence of the QDs, although the radiation-induced excitations occur within the polymer itself. Lastly, important role played the very low QD concentrations in terms of sample transparency, as demonstrated by the drop in the light yield increase in the sample having the higher QD concentration (0.015 wt.%). In this context, as the concentration further increases, aggregation of QDs remains an important issue and more specific embedding procedure of the nanocrystals should be therefore adopted for preserving sample transparency.

Chapter 7 - Polysiloxane/quantum dot nanocomposites for passive dosimetry applications

Part of this chapter has been published in:

ACS Publications THE JOURNAL OF PHYSICAL CHEMISTRY C

E. Zanazzi, M. Favaro, A. Ficorella, L. Pancheri, G. F. Dalla Betta, A. Quaranta, *"Proton Irradiation Effects on Colloidal InGaP/ZnS Core-Shell Quantum Dots Embedded in Polydimethylsiloxane: Discriminating Core from Shell Radiation-Induced Defects through Time-Resolved Photoluminescence Analysis"*, J. Phys. Chem. C, 122 (2018) 22170−22177.

In this chapter we report the study and characterization of polysiloxane samples embedding colloidal QDs for their possible applications as luminescence dosimeters with proton beams. In this respect, samples will be optically characterized in terms of both steady-state and time-resolved photoluminescence (PL) measurements before and after their irradiation with protons at different doses, in order to study the irradiation effects of protons on colloidal nanocrystals and to correlate the radiation-induced PL degradation of the QDs with the released dose.

7.1 Introduction

As reported in subsection 2.2.2, colloidal QDs have been also investigated for applications in passive dosimetry by monitoring the luminescence yield after their exposure to ionizing radiation. In this context, the most promising studies reported in the literature are those proposed by Stodilka et al. [15], Gaur et al. [16] and Withers et al. [17]. All the previous articles report the PL degradation of cadmium-based QDs after their irradiation with γ-rays at different doses, where the colloidal nanocrystals are either in solution (Stodilka et al. and Withers et al.) or embedded in porous silica (Gaur et al.). In general, the reason of this PL degradation has been mainly associated to radiation-induced defects involving the ligands, namely the organic molecules passivating the QD surface, with the formation of surface trap states [15,16]. In this chapter, we extend this research from different aspects. First of all, protons instead of high-energy photons are used as source of ionizing radiation. In fact, the use of proton beams in therapy treatments of certain tumors is continuously growing and there are several facilities around the world exploiting protons for cancer therapy. This is due to the excellent ballistic properties of massive particles, such as protons and other ions, which lose most of their energy at the end of the path in tissue (Bragg peak, subsection 1.1), with modest lateral diffusion, thus preserving the surrounding healthy organs during tumor irradiation. Since in therapy treatments with ionizing radiation both tumor

control and normal tissue complication probability depend on the delivered dose, prediction of clinical results requires accurate knowledge of the absorbed dose for two reasons: (i) to obtain reproducible results for different patients of the same radiotherapy unit and (ii) to transfer clinical results of one radiotherapy unit to another. Therefore, the absorbed dose is required as an operative quantity to control beam delivery, to characterize the beam dosimetrically and to verify dose delivery [14]. For example, in clinical dosimetry with high-energy photons one of the basic quantities for measuring the patient dose and as well for optimizing the patient dose is the entrance surface dose (ESD), defined as the absorbed dose to air at the point of intersection of the radiation beam axis with the entrance surface of the patient. The ESD is usually determined by direct measurements using thermoluminescent dosimeters (TLDs). These devices can be stacked on the surface of a phantom in order to calculate the ESD and therefore to adequately plan a radiation treatment before it is performed on a patient (Figure 7.1). Moreover, TLDs can be also put inside or behind the phantom in order to have other dose measurements. Indeed, TLDs can be also used during the treatments with patients, in order to further monitoring the dose. With the growing of adrotherapies in cancer treatment, these TLDs have started to be used also for ions dosimetry. However, unlike photon radiation, which creates a nearly uniform dose distribution on a microscopic level, ions generate an extremely localized dose deposition along the trajectory of the primary ion reaching extremely high values and leading to saturation effects [13]. Therefore, the possible development of innovative systems for dose measurement with ion beams is of great importance. In this framework, a possibility could be the development of polysiloxane-based film embedding colloidal QDs, where the dose determination is performed with a post-irradiation optical measurement, exploiting the radiation-induced change in the QD optical properties, as partially already investigated in the literature for QDs dispersed in other media.

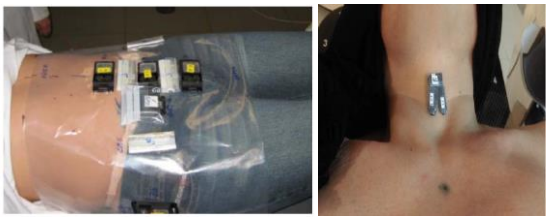

Figure 7.1: TLDs used for measuring the ESD for planning and monitoring radiotherapy treatments involving prostate (left) and thyroid (right) cancers [113]**.**

The interest towards colloidal nanocrystals as luminescent probe in passive dosimetry applications is mainly associated with the particular structure of the nanocrystals, which are composed of a semiconductor volume, and a further surrounding layer of

organic molecules (ligands). This QD structure is therefore inherently composed of a radiation-harder volume coupled with a radiation-weaker ligand layer, where the important role of these ligands in contributing to the overall PL yield has been already demonstrated [114]. Assuming to exploit the PL degradation for dose measurement, this particular QD structure can therefore potentially offer a wider dose dynamical range in comparison with completely-inorganic systems. As regard the embedding medium, in our study colloidal QDs are embedded in polysiloxane, therefore offering flexibility and resulting, for example, to better fit of these films on curved surfaces of phantoms. Lastly, cadmium-free InGaP/ZnS QDs are used: since cadmium has been reported as a major source of QD toxicity, non-cadmium based materials are highly desirable in application related with the biomedical field [115].
However, the possible development of luminescent passive dosimeters based on polysiloxane films embedding QDs requires, as first step, the study of the effects of proton irradiation on the optical properties of the colloidal QDs embedded in polysiloxane, as it will be explored in this chapter.

7.2 Experimental section

Colloidal InGaP/ZnS QDs (subsection 3.4) were diluted in a bi-component polydimethylsiloxane $(C_2H_6OSi)_n$ resin (Rhodorsil® RTV 141 A:B, mass ratio 10:1) in order to achieve a QD concentration of 0.6 mg/ml. The chemical formula of the resin is the same of the DMS-V21 reported in subsection 3.1.3. Resulting solution was then drop-casted in 4 mm diameter round-shaped molds glued on silicon substrates. Crosslinking in oven at 150°C for 1 hour was performed in order to obtain 4 transparent films with a thickness of 50 μm. Sample irradiation were carried out at the Legnaro National Laboratories (Padova, Italy) using the AN2000 Van de Graaff accelerator with a beam spot size of 2×3 mm^2 and beam currents in the range of 20-50 nA. Three samples were irradiated with 2 MeV H^+ ions at three different fluences, namely 10^{14} H^+cm^{-2}, 5×10^{14} H^+cm^{-2} and 10^{15} H^+cm^{-2}. In order to separate irradiation-induced phenomena from possible effects of natural degradation, one sample was not irradiated and kept as reference sample. The range of H^+ in PDMS, calculated with SRIM2013 and considering the density of PDMS as 0.965 gr/cm^3, is 86.4 μm. Therefore, protons go through the whole film thickness releasing an amount of energy of 817 keV, equivalent to the integral of the energy loss curve reported in Figure 7.2(a). Released doses for the three fluences were estimated at 2.7 MGy, 13 MGy and 27 MGy, respectively. These values are several orders of magnitude higher than radiotherapic doses. Nonetheless, the aim of this work is first of all to study the damage mechanisms and their effect on the QD optical properties. In fact, the used proton beam does not allow irradiation conditions suitable for radiotherapy, both in current and in energy.

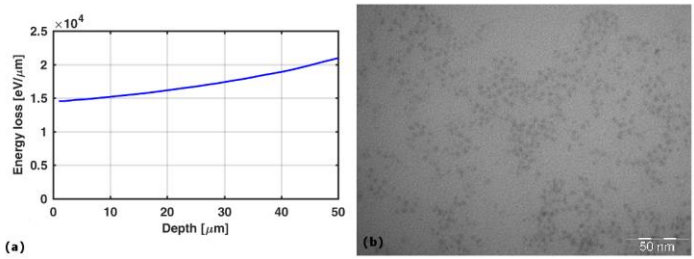

Figure 7.2: (a) energy loss of 2 MeV protons within the 50 µm tick PDMS film (SRIM2013 simulation) and b) TEM image of InGaP/ZnS QDs in solution.

In order to calculate the number of QD per unit volume, the weight of the single dot was evaluated by taking a value of Ga fraction ranging from 52% to 55% and a ZnS shell thickness of about 40% with respect to the InGaP core [116]. Moreover, the overall nanocrystal size of 4 nm was measured with a TEM analysis (Figure 7.2(b)). In this way, a concentration of 1.2×10^{15} QD/cm^3 was estimated. The post-irradiation optical characterization, considering both steady-state and time-resolved measurements, was performed with the optical setup described in subsection 3.6.1, using the 470 nm laser.

7.3 Results and discussion

7.3.1 Optical measurements

Photoluminescence spectra of the samples irradiated with 2 MeV protons at the fluences of 10^{14} H$^+$cm^{-2}; 5×10^{14} H$^+$cm^{-2} and 10^{15} H$^+$cm^{-2} are reported in Figure 7.3. Results in Figure 7.3(a) show a decrease of the average QD PL intensity (integral of the spectra) with the increasing fluence, with no appreciable change in both shape and peak positions of the spectra over the entire fluence range. This average PL decrease can be also appreciated in Figure 7.3(b), where the PL intensity, normalized by the value of the unirradiated sample, is reported in percentage as a function of the irradiation fluence, showing a decrease up to 70% for the highest fluence (10^{15} H$^+$cm^{-2}). This decrease of the average QD PL intensity indicates the introduction, due to the proton irradiation, of PL quenching centres. The observed lowering of the average PL intensity with the irradiation fluence is thus attributed to the increasing density of proton-induced PL quenching centres. However, for a more detailed interpretation time-resolved measurements were performed and reported in Figure 7.4(a), showing a radiation-induced change of the curves with the increasing irradiation fluence.

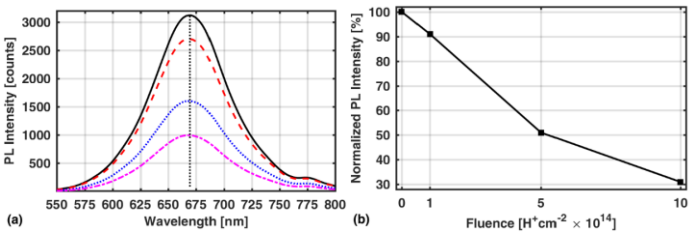

Figure 7.3: (a) PL emission spectra of the samples irradiated with 2 MeV protons at the fluences of 10^{14} H^+cm^{-2} (red dashed line), 5×10^{14} H^+cm^{-2} (blue dotted line) and 10^{15} H^+cm^{-2} (purple dash-dotted line); unirradiated (reference) spectrum reported in solid black; black dotted line indicates the peak position; (b) PL intensity (integral of the spectra) normalized by the value of the unirradiated sample and plotted in percentage as a function of the irradiation fluence.

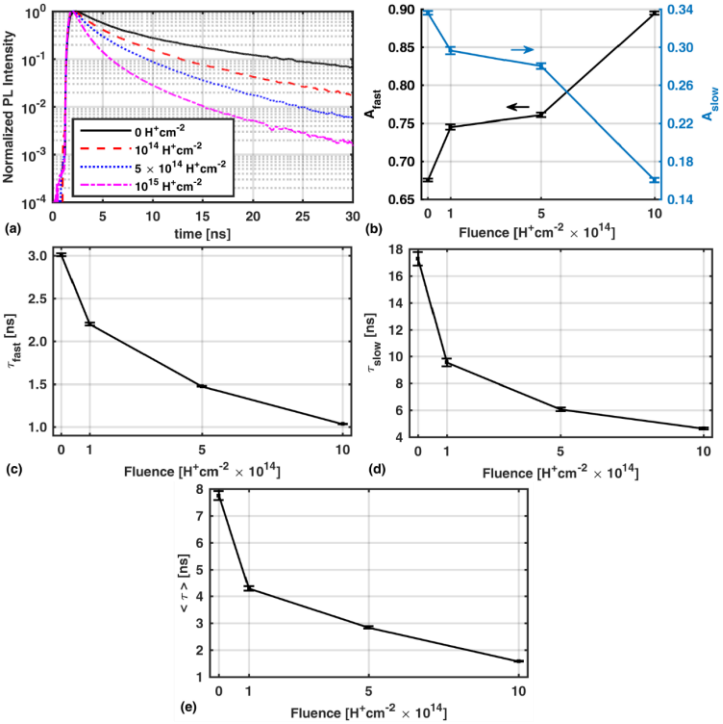

Figure 7.4: (a) PL decay curves of the unirradiated and irradiated samples normalized to the maximum; (b) coefficients of the fit plotted as a function of the irradiation fluence; (c) fast lifetime, (d) slow lifetime and (e) amplitude-averaged lifetime plotted as a function of the irradiation fluence.

7.3.2 Analysis of the QD PL decay

In order to deepen the mechanisms underlying the degradation of the PL intensity with the fluence, PL lifetimes of irradiated and unirradiated samples were analyzed. However, in order to understand the irradiation effects on QDs, the physical interpretation behind the QD PL decay need to be explained. To date, the most of the studies on the QD PL decay mainly refer to cadmium-based QDs [114,117,118], considering both core-type QDs [114] and core-shell QDs [117,118]. In these papers, the QD PL decay is modeled with a biexponential distribution of the type reported in Equation 3.1, with two characteristic lifetimes. In this model, in the framework of Lee et al. [118] for core-shell CdSe/ZnS QD, the fast lifetime (τ_{fast} ~ several nanoseconds) is attributed to recombinations of delocalized (untrapped) carriers and the slow lifetime (τ_{slow} ~ tens of nanoseconds) is associated to recombinations of localized (trapped) carriers, where the localization of electrons/holes is ascribed to heterointerface defects [118]. Similarly, by studying the PL decay of CdSe core-type colloidal QDs, Wang et al. [114] attributed the fast lifetime to the recombination of core states and the slow component to surface-related transitions. In fact, due to the large surface-to-volume ratios, it has been assessed that the surface of colloidal QDs plays an important role in carrier relaxation and recombination processes [114]. In this scenario, carrier trapping phenomena occur at the outer structure of the nanocrystal, leading to delayed recombinations (tens of nanoseconds). More specifically, since electrons have a smaller effective mass than holes in semiconductors, they have a greater probability to be trapped by surface defects, leaving the heavier hole within the QD core. This results in a poor overlap between the electron and hole wavefunctions, therefore increasing the recombination time [114].

As regard the decay dynamics of colloidal InGaP/ZnS QDs, no studies have been so far reported in the literature. However, considering the framework of Lee et al. [118] and under the type-I QD approximation, the measured PL decay curves were fitted with a double exponential function reported in Equation 3.1. The fast and slow coefficients of the fit (A_{fast} and A_{slow}) are plotted as a function of the irradiation fluence in Figure 7.4(b). Figure 7.4 (c), (d) and (e) show the fast, slow and amplitude-averaged lifetimes, respectively, plotted as a function of the irradiation fluence, where the amplitude-averaged lifetime $\langle\tau\rangle$ was calculated as reported in Equation 3.4. All the numerical data related to Figure 7.3 and Figure 7.4 are reported in Table 7.1.

Fluence [H^+/cm^2]	PL Intensity [counts]	τ_{fast} [ns]	τ_{slow} [ns]	$\langle\tau\rangle$ [ns]	A_{fast}	A_{slow}
0	2.86×10^5	3.01±0.02	17.3±0.5	7.7±0.2	0.675±0.002	0.336±0.002
10^{14}	2.59×10^5	2.20± 0.02	9.6 ±0.3	4.29±0.08	0.745 ±0.004	0.296±0.004
5×10^{14}	1.47×10^5	1.47± 0.01	6.1 ± 0.1	2.84±0.04	0.761± 0.003	0.281±0.003
10^{15}	8.98×10^4	1.04±0.01	4.65±0.08	1.58±0.01	0.895±0.002	0.160±0.002

Table 7.1: Numerical data of the steady-state and time-resolved analyses.

As can be observed in Table 7.1, the fast lifetime decreases from 3 ns to 1 ns (33% of the initial value) for the highest fluence, while the slow lifetime decreases with a slightly higher rate, from 17.3 ns to 4.65 ns, which is 27% of the initial value. The corresponding coefficients show that the prevailing component is the fast one, being the 67% in the unirradiated samples and the 85% in the sample irradiated at the highest fluence.

7.3.3 Phenomenological model

Considering both the steady-state measurements (Figure 7.3(a)) and the time-resolved measurements (Figure 7.4(a)), for a general interpretation let us consider the simplified model schematically reported in Figure 7.5.

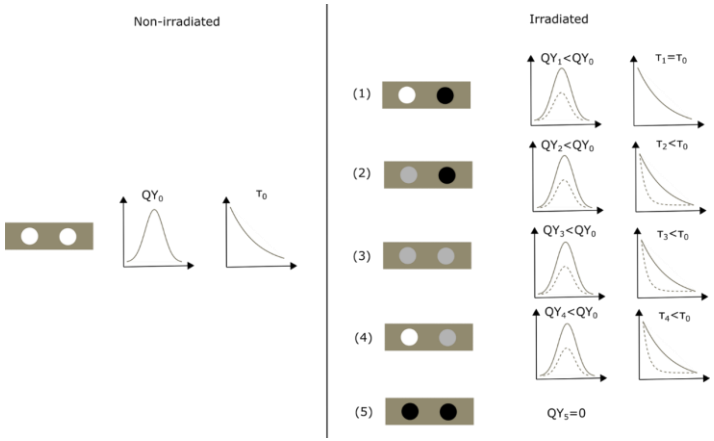

Figure 7.5: Simplified model of the irradiated PDMS volume considering only two embedded QDs.

Since the reported measurements are the results of the average signal coming from the irradiated PDMS volume, we can simplify the model considering only two QDs within this volume. In the nonirradiated sample, the undamaged QDs (represented in white in the left-side of Figure 7.5) are characterized by a given average PL intensity QY_0 and a given PL decay τ_0. In an irradiated sample, the proton interaction mechanisms within the sample can give rise to five different cases (right-side of Figure 7.5), which will be the results of both the nature of the track structure of proton interactions and of the increasing energy loss experienced by the protons with the increasing interaction depth (Figure 7.2(a)). In case (1) of Figure 7.5, the radiation interactions lead to a complete damage of one QD (represented in black), causing the

inhibition of the exciton generation mechanism. Conversely, the other nanocrystal remains completely undamaged. This scenario would give rise to a lowering of the average PL intensity after irradiation without any change in the average PL decay, since the result would be equivalent to a decrease in the QD concentration. Since our measurements show a lowering of the average PL intensity coupled with a change in the QD PL decay, the presence after irradiation of only completely-damaged and completely-undamaged nanocrystals can be excluded. Case (5), representing the complete damage of both QDs, in our irradiating conditions can be also discarded, since a PL signal is always observed, even after the sample irradiation at the highest fluence. The other cases (2, 3 and 4), for which the radiation interactions lead to both a lowering of the average PL intensity and to a change in the time-resolved curves, depict the necessary presence of QDs for which the radiation interactions led to a change in their carrier recombination dynamics (represented in grey in Figure 7.5). This means that the exciton generation mechanism was not completely inhibited by the proton interactions and therefore these nanocrystals can be considered as partially damaged. However, cases (2) and (4) highlight that the further presence of QDs which are completely damaged and undamaged, respectively, cannot be discarded. Under these considerations and assuming that our scenario fits cases 2, 3 and 4, the analysis of the time-resolved measurements represents a way to probe the carrier recombination mechanism of those QDs partially damaged by the radiation interactions. In this scenario, the lowering of the lifetimes reported in Figure 7.4(c) and (d) is due to the formation of PL quenching centres. More specifically, the decrease of the fast lifetime (Figure 7.4(c)) is ascribed to the formation, in the QD inner structure, of defects, which trap the carriers giving rise to non-radiative recombinations. Concerning the slow lifetime, its lowering can be associated to the presence of quenching defects at the outer structure of the nanocrystals, namely both at the shell level and at the shell surface. In this case, it can be assumed that the radiation-induced defects compete in carrier trapping with the other intrinsic defects responsible for the delayed recombinations, leading however to non-radiative recombinations.

Considering Figure 7.4(b) we can observe that the overall trend relies in the increase (decrease) of the fast (slow) coefficient with the increasing fluence. The increase of A_{fast} indicates that the relative number of QDs giving rise to radiative recombinations of delocalized carriers increases with the fluence. Conversely, the decrease of A_{slow} demonstrates that radiative recombinations related with localized carriers are less probable with the increasing fluence. In other words, as the fluence increases, it is more probable to have quenching defects localized at the outer (shell) region than in the inner (core) region of the QD structure. This behaviour is ascribed to the large surface-to-volume ratio of QDs, which translates into a higher density of radiation-induced defects localized at the shell than at the core. It is worth pointing out that, for core-shell QDs, the lowering of the slow lifetime is more likely due to radiation-induced

quenching defects located at the shell level than to those located at the shell surface. The reason relies on the electron/hole wavefunction amplitude in the shell, giving a higher probability for electron/holes to be captured in defects located within the shell than in those located at the shell surface [119]. However, a contribution in carrier trapping phenomena from defects located at the shell surface is also possible. In fact, the role of possible radiation-induced defects on the surface of core-shell QDs has been also discussed by both Stodilka et al. [15] and Gaur et al. [16]. Regarding the effects of γ irradiation on the optical properties of colloidal CdSe/ZnS QDs dispersed in hexane, Stodilka et al. [15] indicated a loss of QD surface ligands after irradiation. Similarly, Gaur et al. [16] associated the QD PL degradation with radiation-induced oxidation phenomena of the thiol ligands and the subsequent formation of surface trap states. In this sense, in our context the nature of the radiation-induced defects at the shell surface can be correlated also to the cleavage of TOPO units leaving dangling orbitals, which may act as non-radiative carrier trapping centres. Furthermore, although the PDMS matrix showed good radiation hardness in these irradiation conditions, a limited damage of the matrix with the formation of additional trapping centres near the shell surface of QDs remains possible. It is worth noting that these additional trapping centres may contribute to affect the QD optical properties [117].

7.3.4 Analysis of the quenching mechanism

In order to further investigate the quenching mechanisms in relation with the irradiation fluence the PL intensities were fitted according to the Stern-Volmer equation:

$$\frac{QY}{QY_0} = \frac{1}{1 + k\Phi} \tag{7.1}$$

and equivalently for the lifetimes:

$$\frac{\tau}{\tau_0} = \frac{1}{1 + k\Phi} \tag{7.2}$$

where QY_0 and τ_0 are the PL intensity and the lifetime of the reference (unirradiated) sample, QY and τ are the PL intensity and the lifetime of the irradiated sample, Φ is the fluence and k is the rate constant of the quenching mechanism, expressed in Φ^{-1}. The Stern-Volmer equation describes dynamic quenching due to diffusional collisions between emitting molecules and quenching units, whose concentration substitutes the fluence in Equation 7.1. In this work, the use of this model can be justified by considering that the quenching of the electron-hole radiative recombination is a dynamic process, driven by the probability for free charge carriers to be trapped by a

radiation defect on their path. Moreover, we can assume that the probability for the formation of a quenching radiation-induced defect is proportional to the fluence, so justifying the use of the fluence in the formula. According to Equations 7.1 and 7.2, data reported in Table 7.1 were therefore normalized by their respective reference values and plotted as a function of the irradiation fluence. Results of the fitting are reported in Figure 7.6 and Table 7.2.

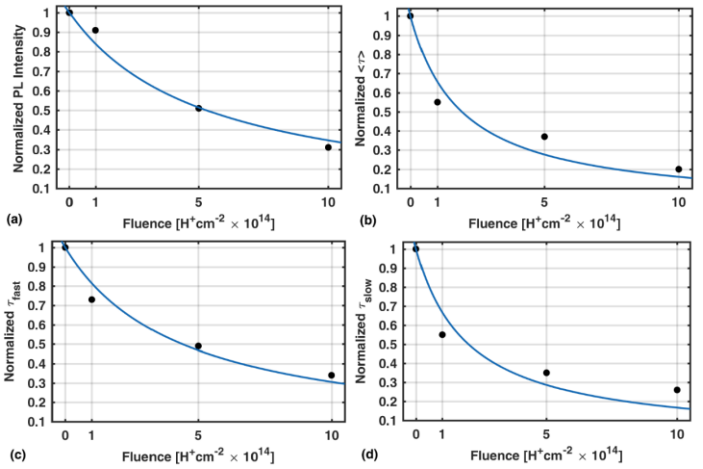

Figure 7.6: Data fitting according to the Stern-Volmer equations of (a) PL intensity, (b) average lifetime, (c) fast lifetime and (d) slow lifetime as a function of the irradiation fluence.

	k [10^{-14} × cm^2/H^+]
PL intensity	0.19 ± 0.02
Tau fast	0.23 ± 0.03
Tau slow	0.5 ± 0.1
Tau average	0.5 ± 0.1

Table 7.2: Rate constants k of the quenching mechanism.

As can be observed, the slow lifetime, related to shell-mediated recombination transitions, is characterized by a higher rate constant in comparison with the fast lifetime, representing the core transitions. This behaviour indicates that it is easier to produce outer defects, which can be either in the shell or on the QD surface as damaged ligands or matrix compounds. In particular, while for core defects a fluence of 4.5×10^{14} H^+cm^{-2} is necessary for halving the fast lifetime, only 2.2×10^{14} H^+cm^{-2} is enough for halving the slow lifetime. It is worth noting that the PL intensity decreases

with the fluence with a rate constant much more similar to the fast lifetime. This trend shows that the intensity decrease under radiation damage resembles that of the inner core transition emissions, whose relative contribution increases with the fluence. In fact, the surface is more prone to damage, being not only the most exposed part of the QD to the radiation and to the network but also the weaker region of the nanocrystal due to the presence of ligand units, where the radiation interaction events can easily give rise to dangling bonds and interface defects.

7.4 Summary

In summary, the optical properties of InGaP/ZnS QDs embedded in PDMS were investigated after their irradiation with 2 MeV protons at the fluences of 10^{14}, 5×10^{14} and 10^{15} $H^{+}cm^{-2}$, roughly corresponding to released doses within the film of 2.7 MGy, 13 MGy and 27 MGy, respectively. Considering the PL spectra, steady-state measurements showed a progressive lowering of the average QD PL intensity within the entire fluence range, phenomenon attributed to the radiation introduction of PL quenching centres. Through time-resolved PL measurements, the radiation-induced change in the QD carrier recombination dynamics was probed. Under the interpretation of the QD PL decay provided by Lee et al. [118], time-resolved curves were fitted with a biexponential function, where the two exponential terms represent the fast and the slow part of the PL decay, respectively. In this interpretation, the fast lifetime is associated with core radiative recombination of the generate exciton: after its generation the exciton directly recombines, with a characteristic time of few nanoseconds. On the other hand, the slow lifetime is associated with shell-mediated radiative recombination: after the exciton generation, either the electron or hole is captured by intrinsic interface defects of the QD structure. This phenomenon gives rise to a delayed radiative recombination, having therefore a longer lifetime (tens of nanoseconds). In this context, the optical characterization after irradiation showed a progressive decrease of both lifetimes with the radiation fluence, indicating the presence of PL quenching defects localized both at the inner and at the outer structure of the nanocrystal. These radiation-induced defects are of different nature in comparison with the intrinsic defects previously mentioned, since they lead to nonradiative recombinations. Therefore, it can be assumed that competition mechanisms between these different defects in capturing charge carriers probably arise. Furthermore, the study of the quenching dynamics revealed that radiation defects are easier to be formed at the outer structure of the QDs. In fact, the outer structure is the most exposed part of the nanocrystals to the radiation interactions as well as the weaker region, due to the presence of the organic ligands. In this respect, it is worth noticing that the important role of possible ligand bond breaks on the reduction of the QD PL has been already assessed in the literature [15,16,114].

As regards possible applications, our results highlighted how the radiation-induced changes in the optical properties of QDs embedded in polysiloxane may be exploited for flexible dose monitory systems involving proton beams.

Chapter 8 - Role of the polymer matrix in the post-irradiation quantum-dot optical response

Part of this chapter has been published in:

E. Zanazzi, M. Favaro, A. Ficorella, L. Pancheri, G. F. Dalla Betta, A. Quaranta, *"Radiation-induced optical change of ion-irradiated CdSeS/ZnS core-shell quantum dots embedded in polyvinyl alcohol",* Nuclear Inst. and Methods in Physics Research B, 435 (2018) 327–330.

E. Zanazzi, M. Favaro, A. Ficorella, L. Pancheri, G. F. Dalla Betta, A. Quaranta, *"Photoluminescence enhancement of colloidal CdSe/ZnS quantum dots embedded in polyvinyl alcohol after 2 MeV proton irradiation: crucial role of the embedding medium",* Optical Materials, 88 (2019) 271–276.

In this chapter we report the study of the proton irradiation effects on the optical properties of colloidal QDs embedded in polyvinyl alcohol. In fact, as deepening of the previous chapter, the use of another polymer allows to evaluate its role on the optical response of the colloidal nanocrystals after irradiation.

8.1 Introduction

As reported in the previous chapter, proton irradiation induces photoluminescence (PL) quenching on the colloidal nanocrystals embedded in polysiloxane. This quenching effect has been also observed in the most of the related articles reported in the literature, although involving different type of QDs irradiated with high-energy photons and embedded in other media [15–17]. In this chapter, by testing the use of a different polymer matrix, namely polyvinyl alcohol (PVOH), we report as with the use of this matrix in certain measurement conditions a PL enhancement of the colloidal QDs after irradiation can be observed. Indeed, this enhancement of the QD PL intensity after the irradiation has been also observed by other authors, although in different conditions, as reported for example by Chang et al. [120].

8.2 Experimental section

Samples based on polyvinyl alcohol (PVOH) $[-CH2CH(OH)-]_n$ were prepared starting from a 10 wt.% water solution of Mowiflex TC232 by Kuraray. Colloidal CdSe/ZnS QDs dispersed in water (subsection 3.4) were diluted in the polymer solution to achieve a final concentration of 0.7 mg/ml. The mixture was then sonicated for 15 minutes to assure a QD uniform dispersion and then casted in 1 cm diameter round-shaped molds. Overnight free air drying at room temperature was performed in order to obtain four PVOH-based samples embedding QDs. For subsequent data comparison, four undoped PVOH samples were also prepared. The amount of solution casted in the molds was defined by previous tests in order to achieve a film thickness of 70 ± 10 μm. Images of the samples are reported in Figure 8.1. Sample irradiation was carried out at the Legnaro National Laboratories (Padova, Italy) using the AN2000 Van de Graaff accelerator with a beam spot size of 3×3 mm^2 and beam currents in the range of 5-10 nA, corresponding to particle flux of about 5×10^{12} ions cm^{-2} s^{-1}. Six samples (three PVOH-based samples embedding QDs and three undoped PVOH samples) were irradiated with 2 MeV H^+ ions at three different fluences, namely 10^{13} H^+cm^{-2}; 5×10^{13} H^+cm^{-2}; 10^{14} H^+cm^{-2}. Two samples (one PVOH-based sample embedding QDs and one undoped PVOH sample) were kept unirradiated for comparison purposes. The range of H^+ ions in PVOH, calculated with SRIM2013, is of 68 μm, therefore, protons are implanted in the target releasing their entire energy (2 MeV). The post-irradiation optical characterization, considering both steady-state and time-resolved measurements, was performed with the optical setup described in subsection 3.6.1, using the 405 nm laser.

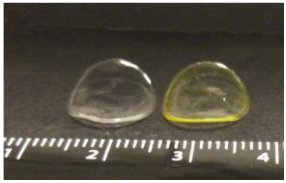

Figure 8.1: Picture of an undoped PVOH sample (left) and of a PVOH sample embedding QDs (right).

8.3 Results and discussion

Photoluminescence spectra, recorded under 405 nm laser excitation, of unirradiated and irradiated PVOH-based samples embedding QDs are reported in Figure 8.2(a). In Figure 8.2(b) the percentage variation of the main peak intensity is reported as a function of the fluence. As can be observed, the sample irradiated at the lowest fluence

(10^{13} H^+cm^{-2}) shows an 80% drop in the QD PL intensity (number of counts at 550 nm) in comparison with the unirradiated sample. At the intermediate fluence (5×10^{13} H^+cm^{-2}), however, a partial recovering of the QD PL intensity is observed. At the highest fluence (10^{14} H^+cm^{-2}) the QD PL intensity is further increased, exceeding the unirradiated sample of the 55%. Moreover, as indicated in Figure 8.2(a) by the dotted marker, in all the irradiated samples the maximum of the QD emission remains located at 550 nm, without significant peak shifts. Furthermore, Figure 8.2(a) shows, with the increasing fluence, the appearance of a new PL feature in the range 450-500 nm, having its maximum around 480 nm. This PL band, which is shown in enlarged picture in Figure 8.2(c), was already observed in our previous preliminary study on the effects of ion irradiation on CdSeS/ZnS QDs embedded in PVOH [121] and it is related to the damage of the polymer network. In Figure 8.2(d), PL spectra of irradiated undoped PVOH films are reported, showing a blue PL feature peaked around 480 nm that increases in intensity with the irradiation fluence. Previous studies on the effects of ionizing radiation on PVOH have pointed out the production of radicals and volatile species, leading to the formation of unsaturated C=C carbon bonds and, at high damage levels, of carbon clusters [122,123]. These species can give rise to the observed PL feature, whose intensity increases with the irradiation fluence owing to the increase of carbon-related emitting centres in the network.

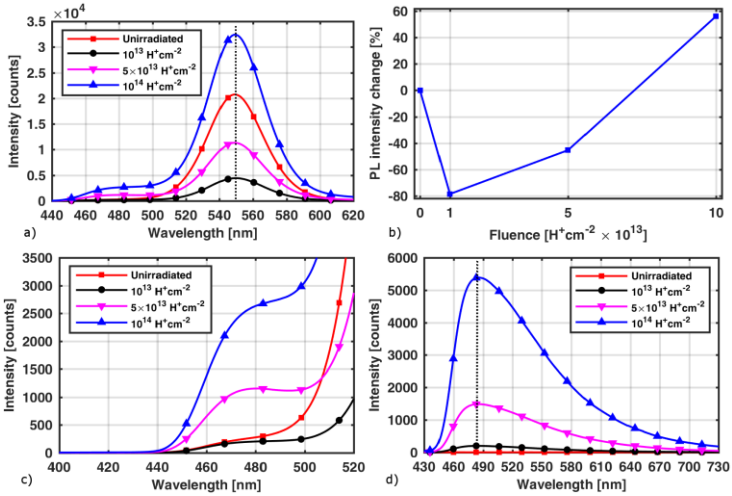

Figure 8.2: a) PL emission spectra of irradiated and unirradiated PVOH-based samples embedding CdSe/ZnS QDs (black dotted line indicates the QD peak position); b) relative PL change of the QDs emission intensity plotted in percentage as a function of the irradiation fluence; c) enlargement of the radiation-induced PL band in QD-doped PVOH samples; d) PL emission spectra of irradiated and unirradiated undoped PVOH samples (black dotted line indicates the peak position).

Since the PVOH PL bands are partially modified by the cut-off filter at 450 nm used for filtering the laser signal, further spectrofluorimetric measurements were performed on unirradiated samples and on the samples irradiated with the highest fluence (10^{14} H^+cm^{-2}). In Figure 8.3, the emission spectra recorded in the range 420-580 nm and acquired at different excitation wavelengths (300-400 nm, 5 nm spaced) are plotted as contour plots (color bar gives the PL emission intensity). Figure 8.3(a) shows the emission spectra of the unirradiated undoped PVOH sample, showing no significant PL feature (the signal is comparable with the background level). On the other hand, the emission spectra of the irradiated undoped PVOH sample, reported in Figure 8.3(b), further highlight the presence of a PL band at 450 nm, in agreement with the PL feature observed with the laser measurements (Figure 8.3(d)) which was partially cut by the optical filter, and of an excitation band peaked around 390 nm. Figure 8.3(c) and (d) show the PL emission spectra of the unirradiated and irradiated QD-doped samples, respectively, showing an increase of the QD PL intensity in the irradiated sample. Furthermore, Figure 8.3(d) also shows the feature of irradiated PVOH, although with a lower intensity in comparison with the irradiated undoped polymer (Figure 8.3(b)), in agreement with the laser measurements reported in Figure 8.2(a).

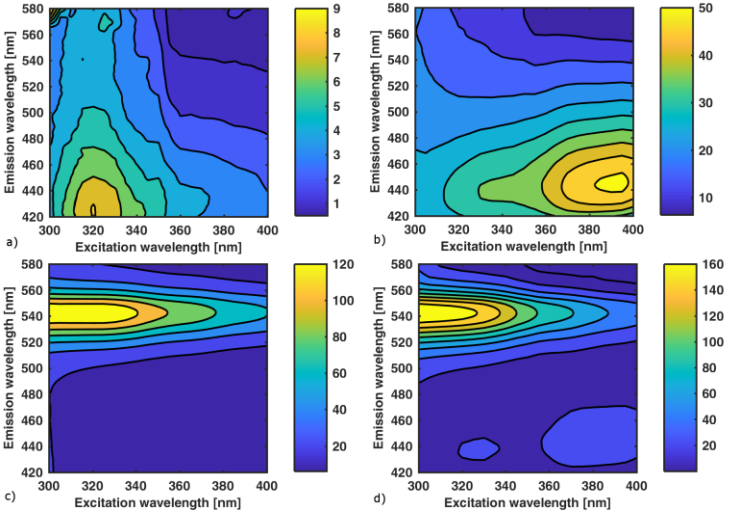

Figure 8.3: PL emission spectra recorded in the excitation range 300-400 nm and emission range 420-580 nm and plotted as contour plots of a) unirradiated undoped PVOH; b) irradiated undoped PVOH (10^{14} H^+cm^{-2}) c) unirradiated QD-doped PVOH and d) irradiated QD-doped PVOH (10^{14} H^+cm^{-2}). Intensity scale of PL emission is given by the color bar.

The observed QD PL recovering and the subsequent enhancement with the increasing fluence can be attributed to energy transfer mechanisms between photoluminescent proton-induced defects in the PVOH network, acting as donors, and QDs, acting as acceptors. In order to deepen this phenomenon, the PL band of the radiation-induced defects in the PVOH network was analyzed in the absence and in the presence of the acceptors (QDs). In fact, the energy transfer efficiency from the donor centers can be calculated through both their PL yield and their lifetime in the presence and in the absence of the acceptor QDs, following the relationship [26,124]:

$$E_{PL} = 1 - \frac{PL_{DA}}{PL_D} = E_\tau = 1 - \frac{\tau_{DA}}{\tau_D} \tag{8.1}$$

where PL_D, τ_D are the PL intensity and lifetime, respectively, of the donor in the absence of the acceptor and PL_{DA}, τ_{DA} are the PL intensity and lifetime, respectively, of the donor in the presence of the acceptor. Time-resolved measurements of irradiated QDs after different fluences and of irradiated PVOH with the highest fluence are reported in Figure 8.4. All the numerical data related to both the steady-state and time-resolved measurements are reported in Table 8.1.

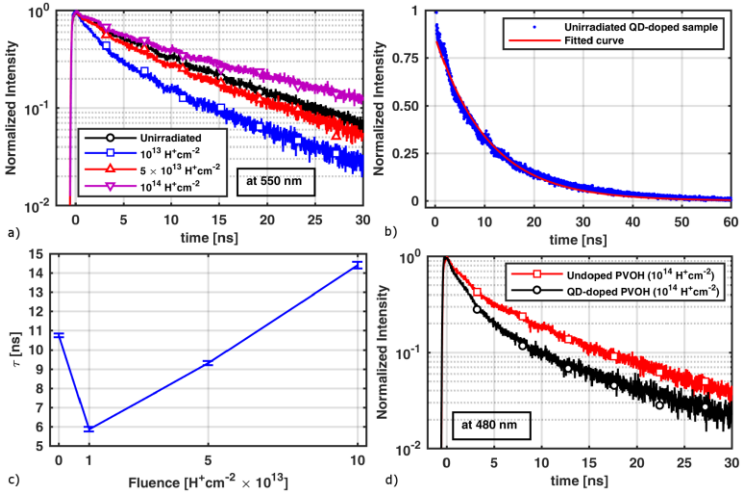

Figure 8.4: a) PL decays of unirradiated and irradiated samples acquired at the acceptor (QDs) emission wavelength (550 nm); b) example of fitted curve (unirradiated QD-doped sample) indicating a good agreement of the PL decay data with the fitting function; c) acceptor (QDs) lifetimes plotted as a function of the irradiation fluence; d) PL decays acquired at the donor emission wavelength (480 nm) in the absence of the acceptor (undoped PVOH) and in the presence of the acceptor (QD-doped PVOH) in samples irradiated at the highest fluence (10^{14} H^+cm^{-2}).

Considering the unirradiated QD-doped sample, in Figure 8.2(c) we can observe that at 480 nm the spectrum reports an emission yield (of about 280 counts) due to the tail of the QD emission peak. In fact, in this sample PL_D is zero and no energy transfer phenomena can occur (PL_{DA} = 0) (Table 8.1). Consequently, as depicted in Figure 8.5(a), the nanocrystals are directly excited by the laser source giving rise to a PL emission with a given intensity (Figure 8.2(a)) and lifetime (Figure 8.4(a)).

Fluence [H^+cm^{-2}]	QD PL intensity @ 550 nm [counts]	PL_D intensity @ 480 nm [counts]	PL_{DA} intensity @ 480 nm [counts]	E_{PL} [%]	τ_D @ 480 nm [ns]	τ_{DA} @ 480 nm [ns]	E_τ [%]	τ_A @ 550 nm [ns]
0	20746	0	0	/	/	/	/	10.8±0.1
10^{13}	4430	195	144	26	/	/	/	5.9±0.1
5×10^{13}	11328	1476	1002	32	/	/	/	9.3±0.1
10^{14}	32403	5348	2202	59	7.1±0.2	3.8±0.1	46	14.4±0.2

Table 8.1: Numerical data of the steady-state and time-resolved measurements.

Concerning the irradiated samples, it is worth mentioning that in the PL_{DA} values reported in Table 8.1 the relative contribution at 480 nm of the QD emission, calculated from the ratio with the main peak at 550 nm, has been already subtracted. In the sample irradiated at the lowest fluence (10^{13} H^+cm^{-2}), the PVOH PL feature starts to appear (PL_D = 195 counts). Moreover, PL_{DA} is lower than PL_D, possibly indicating that energy transfer phenomena occur between the proton-induced PVOH defects and the QD acceptors, (E_{PL} = 26%) (Figure 8.5(b)). However, according to the energy transfer theory [26] and other related studies [106,124], the occurrence of nonradiative energy transfer phenomena should lead to the increase of the acceptor (QDs) PL and lifetime. At this fluence, therefore, the lowering of the QD PL intensity (Figure 8.2(a)) and the shortening of the QD lifetime (Figure 8.4(a)) are mainly associated with the formation, due to proton irradiation, of PL quenching centers for the nanocrystals. In this context, previous studies on irradiated colloidal QDs have highlighted the crucial role of the ligands and their possible radiation-induced cleavage with the formation of PL quenching centres at the QD surface [16–18], leading to a lowering of the QD PL intensity [15,17,18] and a shortening of the QD PL lifetime [16–18].

In the samples irradiated at 5×10^{13} H^+cm^{-2}, PL_{DA} further drops in comparison with PL_D and the QD PL intensity is partially recovered. Accordingly, time-resolved measurement acquired at the QD emission peak indicate a partial lifetime recovering (Figure 8.4(a) and (c)). In this scenario, the higher concentration of radiation-induced PL defects in the PVOH, coupled with the shortening of the average distance between them and the neighbouring QDs, lead to a further increase of the energy transfer efficiency (E_{PL} = 32 %) (Figure 8.5(c)). We specify that, at the first two fluences (10^{13} H^+cm^{-2} and 5×10^{13} H^+cm^{-2}), the low emission intensity of the PVOH PL feature did not

allow us to properly probe the donor PL decay. However, compared to the unirradiated sample, the QD PL intensity and lifetime of the sample irradiated at 5×10^{13} H^+cm^{-2} remain lower, indicating that the damaging of the nanocrystals is still dominating over the tendency of the energy transfer phenomena to increase both the QD PL intensity and lifetime. In fact, as depicted in Figure 8.5, it is reasonable assuming that the PL quenching of the QDs is also increasing with the irradiation fluence [15,17,18].

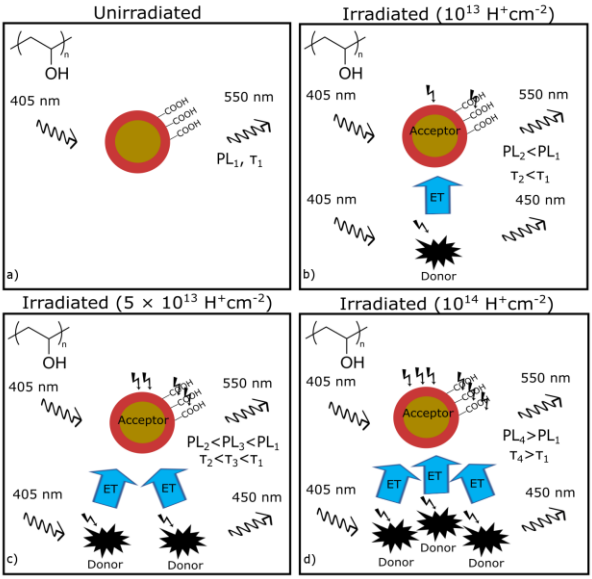

Figure 8.5: Schematic drawing representing a simplified model with one QD embedded in PVOH; a) unirradiated sample; b) sample irradiated at 10^{13} H^+cm^{-2}, showing the appearance of energy transfer phenomena between the radiation-induced PVOH defect and the QD; sample irradiated at c) 5×10^{13} H^+cm^{-2} and d) 10^{14} H^+cm^{-2}, where the higher concentration of radiation-induced PVOH defects leads to a progressive increase of the energy transfer efficiency.

Regarding the sample irradiated at the highest fluence (10^{14} H^+cm^{-2}), the energy transfer efficiency further increases (E_{PL} = 59 %). At this fluence, the higher emission intensity of the PVOH PL feature allowed us to properly probe the donor PL decay in the presence and in the absence of the QD acceptors (Figure 8.4(d)). Results of the fitting indicate a shortening of the donor lifetime in the presence of the acceptors, further demonstrating that energy transfer phenomena occurred between the radiation-induced PL defects in the PVOH and the QDs. More specifically, PL donor lifetime decreases from (7.1 ± 0.2) ns in the undoped PVOH sample to (3.8 ± 0.1) ns in the QD-doped PVOH sample, corresponding to energy transfer efficiency E_τ of 46%.

It is worth specifying, however, that the PL contribution of the QD emission tail at 480 nm cannot be subtracted from the time-resolved measurements, justifying the discrepancy between E_τ and E_{PL}. Moreover, steady-state and time-resolved measurements related to the QD emission peak indicate an enhancement of both the QD PL intensity and lifetime in comparison with the unirradiated sample, meaning that the energy transfer phenomena between the PVOH PL defects and the QDs dominate over the damaging phenomena of the nanocrystals. In general, the overall trend of the acceptor (QDs) lifetime with the increasing fluence (Figure 8.4(c)) agrees with that of the QD intensity of the steady-state measurements (Figure 8.2(b)). Lastly, it is worth mentioning that, due to the broad excitation spectrum of QDs, these are assumed to be only partially excited through the excitation of the PVOH defects (Figure 8.5(b), (c) and (d)).

8.4 Summary

In summary, the effects of 2 MeV protons on the optical properties of colloidal core-shell CdSe/ZnS QDs embedded in PVOH have been reported. The optical characterization of the sample irradiated at the lowest fluence (10^{13} H^+cm^{-2}) showed a drop of the QD PL intensity coupled with a shortening of the QD lifetime, mainly associated to the damage of the nanocrystals and to the introduction of PL quenching centres, as similarly observed in the previous chapter by using polysiloxane as matrix. In the present case, however, the lower radiation hardness of the matrix with the introduction of radiation-induced luminescent defects within the polymer played an important role in the post-irradiation response as the fluence was increased. In fact, at the middle fluence (5×10^{13} H^+cm^{-2}) steady-state and time-resolved measurements highlighted a partial recovering of the QD optical properties. The increasing concentration of PVOH PL defects in the sample irradiated at the highest fluence (10^{14} H^+cm^{-2}) led to an enhanced QD PL intensity and lifetime in comparison with the unirradiated sample. Indeed, it is reasonable assuming that the damage of the nanocrystal increased as well with the irradiation fluence, as reported in the previous chapter. This phenomenon of recovering and enhancing of the QD PL were correlated to the arising of energy transfer phenomena between radiation-induced PL defects in the PVOH, acting as donors, and the QDs, acting as acceptors. The energy transfer mechanism, investigated by probing both the donor and acceptor lifetimes at specific wavelengths, demonstrated to be of nonradiative nature, although with a maximum efficiency around 46% in the sample irradiated with the highest fluence. These results demonstrated as in certain conditions it is possible to have nonradiative energy transfer involving colloidal nanocrystals as acceptors. We hypothesize that the arising of nonradiative energy transfer in this case is related with the specific structure of the radiation-induced defects and their lifetime, that is closer to that of the colloidal

nanocrystals, allowing for partially overcame the excitation crosstalk. In general, this study highlights the important role of the embedding medium and of its radiation hardness on the optical response of the nanocrystals after irradiation.

Chapter 9 - Ongoing research

In this chapter we report a brief summary of the ongoing research activities, which are still uncomplete and therefore not yet published. More specifically, the thermal stability of polysiloxane scintillators is under investigation, as described in subsection 9.1. Moreover, the development of liquid scintillators based on QDs dispersed in solvents is also under study, as reported in subsection 9.2.

9.1 Thermal stability of polysiloxane scintillators

One of the topics under investigation is the study of the thermal stability of polysiloxane scintillators. In this context, light yield and PSD capabilities of polysiloxane scintillators (PMPS, 6 wt.% PPO and 0.02 wt.% LV) are investigated while heating the samples at different temperature steps ranging from 60°C to 120°C, with a setup schematically reported in Figure 9.1. Results are therefore compared with those of a PVT-based sample (EJ-299) subjected to the same heating treatment.

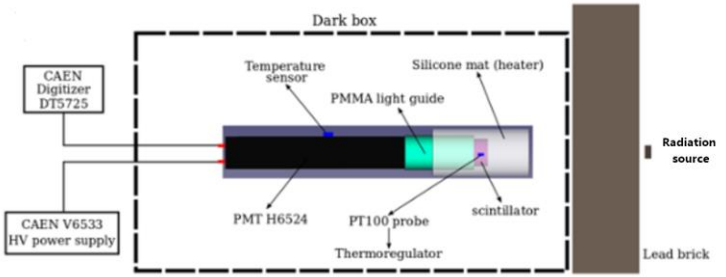

Figure 9.1: Schematic drawing used for the temperature-controlled scintillation measurements. Temperature control of the sample during heating is assured by a resistive temperature probe, connected to a thermoregulator. The heating element is a silicone pad.

As regards the light yield measurements, the scintillation spectra of the polysiloxane sample and of the EJ-299 acquired at different temperatures (RT, 50, 70, 90, 100 and 120°C) are reported in Figure 9.2. The light yield of the samples, evaluated by estimating the position of the Compton edge, is reported in Figure 9.2 (black lines) as relative percentage of the yield of EJ-299 measured at room temperature and plotted versus temperature. As can be observed, the EJ-299 displays a remarkable decrease in light yield as the temperature is increased: at 70°C the yield is almost halved as compared to the value measured at room temperature and at 120°C it is severely reduced to one third of the pristine one. On the other hand, the PMPS based scintillator still keeps the light yield almost constant independently on the heating temperature, being the reduction at 120°C of 7% only.

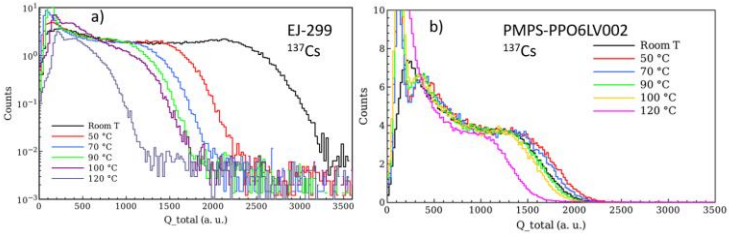

Figure 9.2: Pulse height spectra collected by exposing (a) the EJ-299 and (b) the polysiloxane scintillator to γ-rays from ^{137}Cs source.

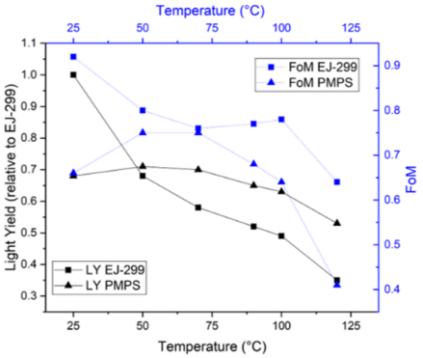

Figure 9.3: Light yield and FoM of the samples plotted as a function of the heating temperature.

As regard the PSP measurements, the FoM values of the samples are also reported in Figure 9.3 (blue lines). As regard the EJ-299, the FoM undergoes a steep decrease as the temperature is increased up to 70°C. Then, a plateu is observed up to 100°C, above which the value further decreases. Regarding the polysiloxane sample, the FoM increases with temperature up to 70°C then it displays a moderate decrease in the range 70-100°C, followed by an abrupt decrease as the scintillator is heated at 120°C. It is worth noticing that the trend of the FoM resembles, for both samples, the trend of the light yield, if we neglect the outer temperature values. Although these measurements are still under verification, the thermal stability of polysiloxanes is under assessment with positive outcomes.

9.2 Quantum-dot-based liquid scintillators

As we have reported in chapter 6, the embedment of colloidal QDs in polysiloxane by direct mixing of the nanocrystals with the aromatic resin does not lead to a uniform dispersion of the QDs. Moreover, evidence of nonradiative energy transfer were not observed up to 1 wt.% of QD concentration and only a small fraction of radiative energy transfer from the polysiloxane to the QDs was reported. Due to these limitations, we performed IBIL measurements on colloidal CdSe/ZnS dispersed in toluene at different concentrations (0, 0.03, 0.3, 3 mg/ml) (Figure 9.4). Measurements were performed at the proton therapy center of Trento by irradiating the samples for 10 seconds with 37 MeV protons at the beam currents of 100, 200 and 300 nA, which correspond to beam fluxes of 1.42×10^7, 2.84×10^7 and 4.32×10^7 $H^+cm^{-2}s^{-1}$.

Figure 9.4: Glass vials containing toluene with dispersed CdSe/ZnS QDs at the concentrations of 0, 0.03, 0.3 and 3 mg/ml under ambient light (left) and UV light (right).

Since the luminescence intensity of the samples remained stable over the irradiation time, only one IBIL spectrum is reported for each measurement, showed in Figure 9.5. As can be observed, around 325 nm a peak is observed in the samples with dispersed QDs at 0 and 0.03 mg/ml. This peak, that is part of the toluene emission cut by the glass vial around 300nm, disappears in the spectra of the other two samples having QD concentration of 0.3 and 3 mg/ml, respectively. This phenomenon, that may indicate the arising of energy transfer, was studied though the optical characterization of the samples. Results indicate that the disappearing of the toluene peak is simply related with its self absorption within the sample and that the aromatic solvent does not contribute to the QD emission. This means that in toluene the QD emission under irradiation is mainly the result of direct excitation mechanisms of the nanocrystals, either by protons or by secondary electrons. Figure 9.6(a) reports the peak intensity as a function of the beam current, showing a good linearity of the response in each sample. Moreover, it can be noticed that the highest emission intensity was observed in the highest QD-concentrated sample, as also showed by the graph in Figure 9.6(b), reporting the peak intensity as a function of the QD concentration.

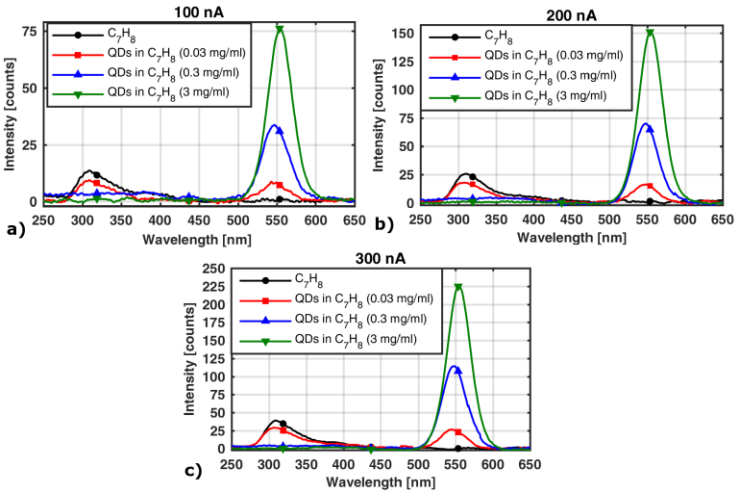

Figure 9.5: IBIL spectra of the four samples at different beam currents.

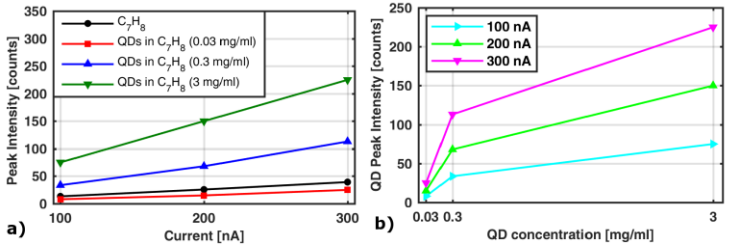

Figure 9.6: a) Peak intensity as a function of the beam current for the four samples and b) QD peak intensity as a function of the QD concentration for the three beam currents.

As future step, we are planning to perform scintillation measurements by coupling a quartz cell containing the QD solution with a PMT. The previous samples can be tested (QD concentration can be also further increased) and the results will be compared to those of a commercial liquid scintillator. In case of positive outcomes, since the aromatic solvent does not contribute to the scintillation process, colloidal QDs dispersed in water can be tested in order to decrease the toxicity of the potential scintillator.

Conclusion and future perspectives

In conclusion, characterization studies of different polysiloxane-based systems for radiation detection applications have been reported.

The first part of this research activity, reported in Chapters 4 and 5, has been dedicated at studying polysiloxane-based scintillators for neutron detection.

As regard polysiloxane scintillators for fast neutron detection, important advances have been made concerning their Pulse Shape Discrimination (PSD) capabilities, as discussed in Chapter 4. In fact, state-of-the-art scintillators based on polyvinyltoluene-(PVT) with PSD capabilities (EJ-299-33A) offer good n-γ discrimination performances, due to their high content of primary dye (30 wt.%) that assures the proximity of the dye molecules, therefore promoting triplet-triplet annihilation (TTA) mechanisms. However, a so high content of primary dye also has some drawbacks, since it can compromise the overall mechanical and thermal resistance of the sample. In our work, we demonstrated as with the use of polymethylphenylsiloxane (PMPS) good PSD capabilities can be achieved with moderate load of primary dye (6 wt.%), since the particular structure of PMPS favours the formation of PPO clusters, thus promoting TTA mechanisms although maintaining low the primary dye concentration. Therefore, the novelty of this work in comparison with the state of the art is represented by flexible polysiloxane-based scintillators having fast-neutron/γ PSD capabilities demonstrated to be comparable with those of PVT-based devices. As regard future perspectives, PSD capabilities of these scintillators in different operating temperatures are under investigation, where the higher thermal stability of polysiloxane in comparison with PVT is under assessment with positive outcomes. Future studies may be also focused at better quantifying the flexibility properties of these samples though mechanical measurements.

Important advances have been also achieved in polysiloxane hybrid scintillators for the detection of thermal neutrons, as reported in Chapter 5. In fact, since commercial scintillators (EJ-426/EJ-420, BC-704) based on ZnS activated with Ag (ZnS:Ag) and mixed with ^{6}LiF powder are fragile and with low adaptability, polysiloxane matrices were doped with the same inorganic materials in order to exploit the ^{6}Li (n, α) ^{3}H reaction for the detection process, although potentially maintaining robust and flexible samples. Since crucial role is played by the size of the ^{6}LiF nanocrystals in the detection efficiency, the scintillation performances were evaluated by tuning the crystal size: samples with crystals size in the order of some μm gave the best efficiency to thermal neutrons, reaching 90% of the commercial analogue, EJ-420. Moreover, two different siloxanes, either with pendant phenyl groups (PSS-22) or with aliphatic groups (DMS-V21) were used. Higher performances were achieved with the matrix having phenyl units, because of better dispersion of the ^{6}LiF crystals. In brief, the novelty of this work in comparison with the state of the art is represented by flexible

and robust polysiloxane-based scintillators for thermal neutron detection whose performances have been optimized according to the size of the ^{6}LiF crystals and to the type of polysiloxane. As regard future perspectives, polysiloxane with greater amounts of phenyl units may be tested in order to evaluate if a further better dispersion of the ^{6}LiF crystals can be achieved, possibly leading to a further increase in the performances. Moreover, quantitative flexibility studies may be particularly relevant also for these type of hybrid scintillators, since the high amount of inorganic materials tend to compromise the mechanical properties of the samples.

In the second part of this research activity, reported in Chapters 6, 7 and 8, systems based on Quantum Dots (QDs) dispersed in polysiloxane and other polymer network for radiation detection applications have been studied. In the first instance, particular interest has been recently dedicated at using colloidal QDs as loading elements in organic scintillators, since they can potentially offer both high-Z sensitization and luminescence properties. In this framework, a recent study by Liu et al. [11] reported promising results on the scintillation response of PVT-based transparent nanocomposites with very high QD loading (up to 60 wt.%), where the nanocrystals are embedded within the polymer with a specific chemical procedure assuring a high transparency of the samples. QDs are therefore exploited as donors in the scintillation process with organic dyes as acceptors. In our work, with a different approach we investigated, in Chapter 6, the possibility of using colloidal QDs as energy acceptors for the polysiloxane emission, by mixing the nanocrystals within the resin at different concentrations (0.003, 0.015, 0.03, 0.3 and 1 wt.%). However, problems related with nanocrystal aggregations and significant decrease of sample transparency were observed from 0.03 wt.%. Moreover, nonradiative energy transfer, crucial for enabling the scintillation process, was not observed for all the QD concentrations. This was mainly correlated, as also discussed by Clapp et al. [107], to the shorter lifetime of the organic donor in comparison with the inorganic acceptor, phenomenon that decreases the probability of having energy transfer. Moreover, the simultaneous excitation of donor and acceptor (excitation crosstalk) further contributes in lowering this probability, since the acceptor may be already into an excited state [107]. Nonetheless, by investigating the luminescence emission of the samples in real-time under proton irradiation we reported as for low QD concentrations (below 0.015 wt.%) an enhancement of the integrated polysiloxane emission up to the 8% is observed in comparison with the pure polysiloxane. This phenomenon, that represents the main novelty of this work, was correlated with the high-Z sensitization offered by the nanocrystals that slightly increases the specific energy loss experienced by protons, although the excitations occur within the polysiloxane, similarly as already observed for other hybrid scintillators under γ-rays [22]. Indeed, the good transparency maintained by the samples loaded at low QD concentrations also played a crucial role. As future perspective, the use of nanocrystals as energy acceptors in polysiloxanes

remains challenging and it therefore requires further investigation. However, the use of colloidal nanocrystals as donors for organic acceptors, as positively explored by Liu et al. in PVT [11], could probably represent a more promising topic of future research in polysiloxane scintillators. In this case, however, a huge quantity of QDs should be embedded (few tents wt.%) in order to provide a suitable stopping power for the radiation: the polysiloxane matrix would therefore mainly act as binder and an organic dye should be also embedded for accepting the energy from the QDs, reducing self-absorption. In general, the main challenge for the development of polysiloxane/QD scintillators consists in embedding the QDs and preserving at the same time an adequate transparency of the sample. In this way, although very challenging, a hybrid scintillator with both flexibility properties and good performances for γ-ray detection could be potentially developed.

Investigation on the use of QDs embedded in polysiloxane films for possible passive ion dosimetry applications has been reported in Chapter 7. In this field, state-of-the-art studies report the luminescence degradation of QDs after their irradiation with γ-rays at different doses, where the colloidal nanocrystals are either in solution [15,17] or embedded in porous silica [16]. These results provided the proof-of-concept for developing passive γ-ray dosimeters exploiting the radiation-induced change in the QD optical properties. Since there is an increasing interest towards the development of innovative passive dosimeters for ion dosimetry, the first novelty of our study was represented by the use of protons instead of high energy photons. In fact, the state-of-the-art passive dosimeters for γ and β dosimetry, the thermoluminescent dosimeters (TLDs), have recently started to be used also for ion dosimetry. These devices are widely used as support tools for planning cancer treatments with high-energy photons, for example by measuring the released dose by introducing TLDs in phantoms before the treatment with patients. However, TLDs show saturation effects when irradiated with ions, possibly leading to underestimation of the measured dose [13]. Moreover, TLDs do not offer flexibility: in this respect, another novelty of our study is the use of polysiloxane, that can potentially open the way for flexible passive dosimeters which can better fit curved surfaces. In this context, as first step we investigated the effects of proton irradiation on polysiloxane/QDs nanocomposites, with the aim of correlating the radiation-induced changes in the QD optical properties with the radiation dose. Results showed a decrease of the photoluminescence (PL) intensity of the nanocrystals with the increasing radiation fluence, due to the introduction of PL quenching centers, indicating that QD-based passive devices can be potentially developed also for proton dosimetry. Moreover, for the first time we demonstrated, by means of time-resolved PL analysis, the possibility to discriminate between inner and outer defects induced by the radiation within the QD structure. In this respect, we observed as the outer structure of the nanocrystals is more prone to be damaged by the radiation, being the most exposed and weakest part of the

structure, due to the presence of organic ligands passivating the QD surface. As future perspectives, investigating the long-term stability of the post-irradiation optical response is of great importance. Moreover, studying the possible induction of PL recovering phenomena as well as better quantifying the detectable dynamical range is of special interest. In this respect, we believe that the structure of the nanocrystals, composed of a radiation-harder core-shell volume and a further surrounding layer of inherently radiation-weaker organic molecules (ligands) can potentially offer a wide dose dynamical range. After the assessment of the previous aspects, polysiloxane films embedding QDs could be studied not only for point dose measurements but also as 2D dosimeters for mapping the spatial dose distribution of the beam. Lastly, we recall the importance also for this application of an adequate mechanical characterization of these polysiloxane/QDs films. As further deepening of the previous part, in Chapter 8 we demonstrated as the QD embedding matrix plays a role in the optical response of the nanocrystals after irradiation. In fact, by using a different polymer, namely polyvinyl alcohol, we observed as luminescent defects were easily introduced by the proton irradiation due to the low radiation hardness of the polymer itself. If the concentration of these defects is high enough, it was observed that in certain excitation conditions these defects can interact with the QDs through nonradiative energy transfer with the nanocrystals acting as acceptors. More specifically, although the damaging of the nanocrystals increases as well with the irradiation fluence, causing the quenching of their PL properties, the energy transfer mechanism tends, on the other hand, to increase their PL intensity and lifetime. This process led, in the sample irradiated with the highest fluence, to an increase of the QD PL intensity and lifetime in comparison with the unirradiated sample. These results, never reported in the literature before, highlighted as in certain cases nonradiative energy transfer to QDs as acceptors can arise, and it has been correlated to the specific conformation of the radiation-induced defects, their concentration and their lifetime, the latter closer to that of inorganic nanocrystals, allowing for partially overcoming the excitation crosstalk.

Concluding, many advances have been achieved in the study and development of organic and hybrid polysiloxane-based radiation detection systems for scintillation and passive dosimetry applications and several future investigating perspectives have been highlighted.

Appendix A - List of abbreviation and acronyms

CE	Compton Edge
DCFD	Digital Constant Fraction Discrimination
FPGA	Field Programmable Gate Array
FRET	Förster Resonance Energy Transfer
FWHM	Full Width at Half Maximum
IBIL	Ion-Beam Induced Luminescence
IRF	Instrument Response Function
LO	Light Output
LAB	dialkylbenzene
LET	Linear Energy Transfer
LV	Lumogen Violet
PDMS	PolyDiMethylSiloxane
PL	Photoluminescence
PMT	Photomultipliertube
PPO	2,5-diphenyloxazole
PS	PolyStyrene
PSD	Pulse Shape Discrimination
PSP	Pulse Shape Parameter
PSS-100	(99%-100%) polyphenylmethyl siloxane vinyl terminated
PSS-1418	(14-18% diphenylsiloxane)-dimethylsiloxane silanol terminated
PSS-22	(22%-25%) diphenylsiloxane-dimethylsiloxane vinyl terminated
PVOH	polyvinyl alcohol
PVT	PolyVinylToluene
QD	Quantum Dot
RTV	Room-Temperature Vulcanization
SEM	Scanning Electron Microscope
TCSPC	Time-correlated single-photon counting
TLD	ThermoLuminescence Dosimeter
TOF	Time-Of-Flight
TTA	Triplet-triplet annihilation

Appendix B - List of figures

Appendix C - List of tables

References

[1] J.B. Birks, The Theory and Practice of Scintillation Counting, Pergamon Press, 1964.

[2] A. Quaranta, S.M. Carturan, T. Marchi, V.L. Kravchuk, F. Gramegna, G. Maggioni, M. Degerlier, Optical and scintillation properties of polydimethyl-diphenylsiloxane based organic scintillators, IEEE Trans. Nucl. Sci. 57 (2010) 891–900. doi:10.1109/TNS.2010.2042817.

[3] A. Quaranta, S. Carturan, M. Cinausero, T. Marchi, F. Gramegna, M. Degerlier, A. Cemmi, S. Baccaro, Characterization of polysiloxane organic scintillators produced with different phenyl containing blends, Mater. Chem. Phys. 137 (2013) 951–958. doi:10.1016/j.matchemphys.2012.10.041.

[4] L. Basiricò, A. Ciavatti, T. Cramer, P. Cosseddu, A. Bonfiglio, B. Fraboni, Direct X-ray photoconversion in flexible organic thin film devices operated below 1 V, Nat. Commun. 7 (2016) 13063. doi:10.1038/ncomms13063.

[5] A. Ciavatti, E. Capria, A. Fraleoni-Morgera, G. Tromba, D. Dreossi, P.J. Sellin, P. Cosseddu, A. Bonfiglio, B. Fraboni, Toward Low-Voltage and Bendable X-Ray Direct Detectors Based on Organic Semiconducting Single Crystals, Adv. Mater. 27 (2015) 7213–7220. doi:10.1002/adma.201503090.

[6] S. Carturan, A. Quaranta, T. Marchi, F. Gramegna, M. Degerlier, M. Cinausero, V.L. Kravchuk, M. Poggi, Novel polysiloxane-based scintillators for neutron detection, Radiat. Prot. Dosimetry. 143 (2011) 471–476. doi:10.1093/rpd/ncq403.

[7] A. Quaranta, S. Carturan, T. Marchi, M. Buffa, M. Degerlier, M. Cinausero, G. Guastalla, F. Gramegna, G. Valotto, G. Maggioni, V.L. Kravchuk, Doped polysiloxane scintillators for thermal neutrons detection, J. Non. Cryst. Solids. 357 (2011) 1921–1925. doi:10.1016/j.jnoncrysol.2010.10.043.

[8] M. Dalla Palma, A. Quaranta, T. Marchi, G. Collazuol, S. Carturan, M. Cinausero, M. Degerlier, F. Gramegna, Red emitting phenyl-polysiloxane based scintillators for neutron detection, IEEE Trans. Nucl. Sci. 61 (2014) 2052–2058. doi:10.1109/TNS.2014.2302036.

[9] T. Marchi, F. Pino, C.L. Fontana, A. Quaranta, E. Zanazzi, M. Vesco, Optical properties and pulse shape discrimination in siloxane-based scintillation detectors, Sci. Rep. (2019) 1–13. doi:10.1038/s41598-019-45307-8.

[10] S.M. Carturan, M. Vesco, I. Bonesso, A. Quaranta, G. Maggioni, L. Stevanato, E. Zanazzi, T. Marchi, D. Fabris, D. Cinausero, F. Pino, F. Gramegna, A Flexible scintillation sensors for the detection of thermal neutrons based on siloxane 6 LiF containing composites : Role of 6 LiF crystals size and dispersion, Nucl. Inst. Methods Phys. Res. A. 925 (2019) 109–115. doi:10.1016/j.nima.2019.01.088.

[11] C. Liu, Z. Li, T.J. Hajagos, D. Kishpaugh, D.Y. Chen, Q. Pei, Transparent Ultra-High-Loading Quantum Dot/Polymer Nanocomposite Monolith for Gamma Scintillation, ACS Nano. 11 (2017) 6422–6430. doi:10.1021/acsnano.7b02923.

[12] E. Zanazzi, M. Favaro, A. Ficorella, L. Pancheri, G.F. Dalla Betta, A.

Quaranta, Real-Time Optical Response of Polysiloxane/Quantum Dot Nanocomposites under 2 MeV Proton Irradiation: Luminescence Enhancement of Polysiloxane Emission through Quantum Dot Sensitization, Phys. Status Solidi Appl. Mater. Sci. 1900586 (2019) 1–7. doi:10.1002/pssa.201900586.

[13] D. Boscolo, E. Scifoni, A. Carlino, C. La Tessa, T. Berger, M. Durante, V. Rosso, M. Krämer, TLD efficiency calculations for heavy ions: An analytical approach, Eur. Phys. J. D. 69 (2015) 11–13. doi:10.1140/epjd/e2015-60208-3.

[14] C.P. Karger, O. Jäkel, H. Palmans, T. Kanai, Dosimetry for ion beam radiotherapy, Phys. Med. Biol. 55 (2010). doi:10.1088/0031-9155/55/21/R01.

[15] R.Z. Stodilka, J.J.L. Carson, K. Yu, B. Zaman, C. Li, D. Wilkinson, Optical Degradation of CdSe / ZnS Quantum Dots upon Gamma-Ray Irradiation, J. Phys. Chem. C. 113 (2009) 2580–2585. doi:10.1021/jp808836g.

[16] G. Gaur, D.S. Koktysh, D.M. Fleetwood, R.A. Weller, R.A. Reed, B.R. Rogers, S.M. Weiss, Influence of Ionizing Radiation and the Role of Thiol Ligands on the Reversible Photodarkening of CdTe/CdS Quantum Dots, ACS Appl. Mater. Interfaces. 8 (2016) 7869–7876. doi:10.1021/acsami.5b09657.

[17] N.J. Withers, K. Sankar, B.A. Akins, T.A. Memon, T. Gu, J. Gu, G.A. Smolyakov, M.R. Greenberg, T.J. Boyle, M. Osiński, Rapid degradation of CdSe/ZnS colloidal quantum dots exposed to gamma irradiation, Appl. Phys. Lett. 93 (2008) 2011–2014. doi:10.1063/1.2978073.

[18] E. Zanazzi, M. Favaro, A. Ficorella, L. Pancheri, G.F. Dalla Betta, A. Quaranta, Proton Irradiation Effects on Colloidal InGaP / ZnS Core-Shell Quantum Dots Embedded in Polydimethylsiloxane : Discriminating Core from Shell Radiation-Induced Defects through Time-Resolved Photoluminescence Analysis, J. Phys. Chem. C. 122 (2018) 22170–22177. doi:10.1021/acs.jpcc.8b06181.

[19] E. Zanazzi, M. Favaro, A. Ficorella, L. Pancheri, G.F. Dalla Betta, A. Quaranta, Photoluminescence enhancement of colloidal CdSe / ZnS quantum dots embedded in polyvinyl alcohol after 2 MeV proton irradiation : crucial role of the embedding medium, Opt. Mater. (Amst). 88 (2019) 271–276. doi:10.1016/j.optmat.2018.11.047.

[20] G.F. Knoll, Radiation Detection and Measurement, 4th Edition, John Wiley & Sons, 2010.

[21] https://www.nuclear-power.net/, (n.d.).

[22] G.H. V. Bertrand, M. Hamel, F. Sguerra, Current Status on Plastic Scintillators Modifications, Chem. - A Eur. J. 20 (2014) 15660–15685. doi:10.1002/chem.201404093.

[23] T.J. Hajagos, C. Liu, N.J. Cherepy, Q. Pei, High-Z Sensitized Plastic Scintillators: A Review, Adv. Mater. 30 (2018) 1–13. doi:10.1002/adma.201706956.

[24] https://eljentechnology.com/products/plastic-scintillators, (n.d.).

[25] B. Valeur, M.N. Berberan-Santos, Molecular Fluorescence: Principles and

Applications, 2012. doi:10.1002/9783527650002.
[26] J.R. Lakowicz, Principles of Fluorescence Spectroscopy, Springer, 2006. doi:10.1007/978-0-387-46312-4.
[27] T.A. King, R. Voltz, The time dependence of scintillation intensity in aromatic materials, Proc. R. Soc. London. Ser. A. Math. Phys. Sci. 289 (1966) 424–439. doi:10.1098/rspa.1966.0021.
[28] K.C. Tsou, Evaluation of organometallic compounds for gamma detection in plastic scintillators, IEEE Trans. Nucl. Sci. 12 (1965) 28–33. doi:10.1109/TNS.1965.4323493.
[29] S.R. Sandler, K.C. Tsou, Evaluation of organometallics in plastic scintillators toward γ-radiation, Int. J. Appl. Radiat. Isot. 15 (1964) 419–426. doi:10.1016/0020-708X(64)90140-1.
[30] S.R. Sandler, K.C. Tsou, Quenching of the Scintillation Process in Plastics by Organometallics, J. Phys. Chem. 68 (2007) 300–304. doi:10.1021/j100784a015.
[31] J. Dannin, S.R. Sandler, B. Baum, The use of organometallic compounds in plastic scintillators for the detection and resolution of gamma rays, Int. J. Appl. Radiat. Isot. 16 (1965) 589–597. doi:10.1016/0020-708X(65)90095-5.
[32] N. V Jalabadze, R. Chedia, T. Kukava, L. Nadaraia, Development of New Technologies for the Manufacturing of Nanocrystalline Scintillation Materials, 55 (2008) 1514–1522.
[33] V. Vistovskyy, T. Malyy, A. Pushak, A. Vas, A. Shapoval, N. Mitina, A. Gektin, A. Zaichenko, A. Voloshinovskii, Luminescence and scintillation properties of LuPO4-Ce nanoparticles, J. Lumin. 145 (2014) 232–236. doi:10.1016/j.jlumin.2013.07.027.
[34] A. Lauria, I. Villa, M. Fasoli, M. Niederberger, A. Vedda, Multifunctional Role of Rare Earth Doping in Optical Materials : Nonaqueous Sol-Gel Synthesis of Stabilized Cubic HfO 2 Luminescent Nanoparticles, ACS Nano. (2013) 7041–7052. doi:10.1021/nn402357s.
[35] W. Cai, A. Wang, L. Fu, J. Hu, T. Rao, J. Wang, J. Zhong, Preparation and luminescent properties of GdOF : Ce , Tb nanoparticles and their transparent PMMA nanocomposites, Opt. Mater. (Amst). 43 (2015) 36–41. doi:10.1016/j.optmat.2015.02.020.
[36] T.M. Demkiv, O.O. Halyatkin, V. V Vistovskyy, A. V Gektin, A.S. Voloshinovskii, Luminescent and kinetic properties of the polystyrene composites based on BaF 2 nanoparticles, Nucl. Instruments Methods Phys. Res. A. 810 (2016) 1–5. doi:10.1016/j.nima.2015.11.130.
[37] J.A. Phys, P. Guss, R. Guise, D. Yuan, S. Mukhopadhyay, R.O. Brien, D. Lowe, Z. Kang, P. Guss, R. Guise, D. Yuan, S. Mukhopadhyay, R.O. Brien, D. Lowe, Z. Kang, H. Menkara, V. V Nagarkar, Lanthanum halide nanoparticle scintillators for nuclear radiation detection, Appl. Phys. Lett. 113 (2013) 64303. doi:10.1063/1.4790867.
[38] A.-L. Bulin, A. Vasil'ev, A. Belsky, D. Amans, G. Ledoux, C. Dujardin, Modelling energy deposition in nanoscintillators to predict the efficiency of the X-ray-induced photodynamic effect, Nanoscale. (2015). doi:10.1039/b000000x.

[39] W. Cai, Q. Chen, N. Cherepy, A. Dooraghi, D. Kishpaugh, A. Chatziioannou, S. Payne, W. Xiang, Q. Pei, Synthesis of bulk-size transparent gadolinium oxide– polymer nanocomposites for gamma ray spectroscopy, J. Mater. Chem. C. 1 (2013) 1970–1976. doi:10.1039/c2tc00245k.

[40] N. Zaitseva, B.L. Rupert, I. Pawe, A. Glenn, H.P. Martinez, L. Carman, M. Faust, N. Cherepy, S. Payne, Plastic scintillators with efficient neutron / gamma pulse shape discrimination, Nucl. Instruments Methods Phys. Res. A. 668 (2012) 88–93. doi:10.1016/j.nima.2011.11.071.

[41] S.A. Pozzi, M.M. Bourne, S.D. Clarke, Pulse shape discrimination in the plastic scintillator EJ-299-33, Nucl. Inst. Methods Phys. Res. A. 723 (2013) 19–23. doi:10.1016/j.nima.2013.04.085.

[42] R.D. Breukers, C.M. Bartle, A. Edgar, Transparent lithium loaded plastic scintillators for thermal neutron detection, Nucl. Inst. Methods Phys. Res. A. 701 (2013) 58–61. doi:10.1016/j.nima.2012.10.080.

[43] S.M. Carturan, T. Marchi, G. Maggioni, F. Gramegna, M. Degerlier, M. Cinausero, M. Dalla Palma, A. Quaranta, Thermal neutron detection by entrapping 6 LiF nanocrystals in siloxane scintillators, J. Phys. Conf. Ser. 620 (2015) 012010. doi:10.1088/1742-6596/620/1/012010.

[44] K.D. Sattler, Handbook of nanophysics - Nanoparticles and Quantum Dots, CRC press, 2013. doi:10.1017/CBO9781107415324.004.

[45] A.L. Rogach, Semiconductor Nanocrystal Quantum Dots - Synthesis, Assembly, Spectroscopy and Applications, Springer, 2008. doi:10.1007/978-3-211-75237-1.

[46] A.M. Smith, S. Nie, Semiconductor nanocrystals: Structure, properties, and band gap engineering, Acc. Chem. Res. 43 (2010) 190–200. doi:10.1021/ar9001069.

[47] S.E. Létant, T.-F. Wang, Study of porous glass doped with quantum dots or laser dyes under alpha irradiation, Appl. Phys. Lett. 88 (2006) 67–70. doi:10.1063/1.2182072.

[48] S.E. Létant, T.-F. Wang, Semiconductor Quantum Dot Scintillation under γ-Ray Irradiation, Nano Lett. 6 (2006) 2877–2880. doi:10.1021/nl0620942.

[49] Z. Kang, Y. Zhang, H. Menkara, B.K. Wagner, C.J. Summers, W. Lawrence, V. Nagarkar, CdTe quantum dots and polymer nanocomposites for x-ray scintillation and imaging, Appl. Phys. Lett. 98 (2011). doi:10.1063/1.3589366.

[50] W.G. Lawrence, S. Thacker, S. Palamakumbura, K.J. Riley, V. V. Nagarkar, Quantum dot-organic polymer composite materials for radiation detection and imaging, IEEE Trans. Nucl. Sci. 59 (2012) 215–221. doi:10.1109/TNS.2011.2178861.

[51] I.H. Campbell, B.K. Crone, Quantum-dot/organic semiconductor composites for radiation detection, Adv. Mater. 18 (2006) 77–79. doi:10.1002/adma.200501434.

[52] S.H. Benedict, Review of Radiation Oncology Physics: A Handbook for Teachers and Students, J. Appl. Clin. Med. Phys. 5 (2004) 91–92. doi:10.1120/jacmp.2021.25315.

[53] D. Kabat, D. Nahajowski, E. Góra, B. Rozwadowska-Bogusz, J. Lesiak, B.

Polak, Czopyk, P. Olko, M.P.R. Waligórski, On the clinical applicability of large-area 2-D TL dosimetry for verifying small photon radiotherapy beams, Radiat. Meas. 43 (2008) 1004–1007. doi:10.1016/j.radmeas.2007.11.057.

[54] P. Olko, Ł. Czopyk, M. Kłosowski, M.P.R. Waligórski, Thermoluminescence dosimetry using TL-readers equipped with CCD cameras, Radiat. Meas. 43 (2008) 864–869. doi:10.1016/j.radmeas.2007.12.037.

[55] B. Marczewska, P. Bilski, P. Olko, M.P.R. Waligórski, Measurement of 2-D dose distributions by large-area thermoluminescent detectors, Radiat. Meas. 38 (2004) 833–837. doi:10.1016/j.radmeas.2004.03.014.

[56] T. Berger, M. Hajek, TL-efficiency-Overview and experimental results over the years, Radiat. Meas. 43 (2008) 146–156. doi:10.1016/j.radmeas.2007.10.029.

[57] P.R. Hobson, D.E. Leslie, D.R. Smith, Effect of gamma radiation on potential ionising radiation detectors and dosimeters based on quantum dots, 2011 IEEE Nucl. Sci. Symp. Conf. Rec. (2011) 3015–3017. doi:10.1109/NSSMIC.2011.6152542.

[58] J.E. Mark, H.R. Allcock, R. West, Inorganic Polymers , Second Edition, Oxford University Press, 2005. doi:10.1002/adma.19930050116.

[59] A. Tiwari, M.D. Soucek, Concise Encyclopedia of High Performance Silicones, J. Wiley and Sons, 2014. doi:10.1002/9781118938478.ch3.

[60] M. Bowen, S. Majewski, D. Pettey, J. Walker, R. Wojcik, C. Zorn, A new radiation-resistant plastic scintillator, IEEE Trans. Nucl. Sci. 36 (1989) 562–566. doi:10.1109/23.34501.

[61] T. Itoh, Spectroscopy and photophysics of methylphenylsiloxane- and diphenylsiloxane-based molecules and polymers, Res. Chem. Intermed. 27 (2001) 669–685. doi:10.1163/156856701317051761.

[62] A. Quaranta, S. Carturan, T. Marchi, A. Antonaci, C. Scian, V.L. Kravchuk, M. Degerlier, F. Gramegna, G. Maggioni, Radiation hardness of polysiloxane scintillators analyzed by ion beam induced luminescence, Nucl. Instruments Methods Phys. Res. Sect. B Beam Interact. with Mater. Atoms. 268 (2010) 3155–3159. doi:10.1016/j.nimb.2010.05.077.

[63] M. Hamel, V. Simic, S. Normand, Fluorescent 1,8-naphthalimides-containing polymers as plastic scintillators. An attempt for neutron-gamma discrimination, React. Funct. Polym. 68 (2008) 1671–1681. doi:10.1016/j.reactfunctpolym.2008.09.005.

[64] N.D. Alharbi, N. Salah, S.S. Habib, E. Alarfaj, Synthesis and characterization of nano- and microcrystalline cubes of pure and Ag-doped LiF, J. Phys. D. Appl. Phys. 46 (2013). doi:10.1088/0022-3727/46/3/035305.

[65] D. Cester, M. Lunardon, G. Nebbia, L. Stevanato, G. Viesti, S. Petrucci, C. Tintori, Pulse shape discrimination with fast digitizers, Nucl. Instruments Methods Phys. Res. Sect. A Accel. Spectrometers, Detect. Assoc. Equip. 748 (2014) 33–38. doi:10.1016/j.nima.2014.02.032.

[66] L. Stevanato, D. Fabris, X. Hao, M. Lunardon, S. Moretto, G. Nebbia, S. Pesente, L. Sajo-Bohus, G. Viesti, Light output of EJ228 scintillation neutron detectors, Appl. Radiat. Isot. 69 (2011) 369–372. doi:10.1016/j.apradiso.2010.10.022.

[67] D. Cester, G. Nebbia, L. Stevanato, F. Pino, G. Viesti, Experimental tests of the new plastic scintillator with pulse shape discrimination capabilities EJ-299-33, Nucl. Instruments Methods Phys. Res. Sect. A Accel. Spectrometers, Detect. Assoc. Equip. 735 (2014) 202–206. doi:10.1016/j.nima.2013.09.031.

[68] B. Wan, X.Y. Zhang, L. Chen, H.L. Ge, F. Ma, H. Bin Zhang, Y.Q. Ju, Y. Bin Zhang, Y.Y. Li, X.W. Xu, Digital pulse shape discrimination methods for n-γ separation in an EJ-301 liquid scintillation detector, Chinese Phys. C. 39 (2015) 1–6. doi:10.1088/1674-1137/39/11/116201.

[69] F. Tommasino, M. Rovituso, S. Fabiano, S. Piffer, C. Manea, S. Lorentini, S. Lanzone, Z. Wang, M. Pasini, W.J. Burger, C. La Tessa, E. Scifoni, M. Schwarz, M. Durante, Proton beam characterization in the experimental room of the Trento Proton Therapy facility, Nucl. Inst. Methods Phys. Res. A. 869 (2017) 15–20. doi:10.1016/j.nima.2017.06.017.

[70] J.F. Ziegler, M.D. Ziegler, J.P. Biersack, SRIM - The stopping and range of ions in matter, Nucl. Instruments Methods Phys. Res. Sect. B Beam Interact. with Mater. Atoms. 268 (2010) 1818–1823. doi:10.1016/j.nimb.2010.02.091.

[71] T. Kögler, R. Beyer, E. Birgersson, R. Hannaske, A.R. Junghans, R. Massarczyk, A. Matic, A. Wagner, K. Zuber, Light yield and n–γ pulse-shape discrimination of liquid scintillators based on linear alkyl benzene, Nucl. Instruments Methods Phys. Res. Sect. A Accel. Spectrometers, Detect. Assoc. Equip. 701 (2013) 285–293. doi:10.1016/j.nima.2012.10.059.

[72] I.B. Nemchenok, V.I. Babin, V.B. Brudanin, O.I. Kochetov, V. V. Timkin, Liquid scintillator based on linear alkylbenzene, Phys. Part. Nucl. Lett. 8 (2011) 129–135. doi:10.1134/S1547477111020099.

[73] P.K. Lightfoot, V.A. Kudryavtsev, N.J.C. Spooner, I. Liubarsky, R. Luscher, N.J.T. Smith, Development of a gadolinium-loaded liquid scintillator for solar neutrino detection and neutron measurements, Nucl. Instruments Methods Phys. Res. Sect. A Accel. Spectrometers, Detect. Assoc. Equip. 522 (2004) 439–446. doi:10.1016/j.nima.2003.11.390.

[74] D.L. Horrocks, Pulse Shape Discrimination with Organic Liquid Scintillator Solutions, Appl. Spectrosc. 24 (1970) 397–404. doi:10.1366/000370270774371435.

[75] R. Voltz, J.L. da Silva, G. Laustriat, A. Coche, Influence of the Nature of Ionizing Particles on the Specific Luminescence of Organic Scintillators, J. Chem. Phys. 45 (1966) 3306–3311. doi:10.1063/1.1728106.

[76] G.H.V. Bertrand, M. Hamel, S. Normand, F. Sguerra, Pulse shape discrimination between (fast or thermal) neutrons and gamma rays with plastic scintillators: State of the art, Nucl. Instruments Methods Phys. Res. Sect. A Accel. Spectrometers, Detect. Assoc. Equip. 776 (2015) 114–128. doi:10.1016/j.nima.2014.12.024.

[77] P. Roy, K. Banerjee, A.K. Saha, C. Bhattacharya, J.K. Meena, P. Bhaskar, S. Mukhopadhyay, S. Bhattacharya, Detailed investigation on the possibility of using EJ-299-33A plastic scintillator for fast neutron spectroscopy in large scale experiments, Nucl. Instruments Methods Phys. Res. Sect. A Accel. Spectrometers, Detect. Assoc. Equip. 901 (2018) 198–202.

doi:10.1016/j.nima.2018.06.007.
[78] N.P. Zaitseva, A.M. Glenn, A.N. Mabe, M.L. Carman, C.R. Hurlbut, J.W. Inman, S.A. Payne, Recent developments in plastic scintillators with pulse shape discrimination, Nucl. Instruments Methods Phys. Res. Sect. A Accel. Spectrometers, Detect. Assoc. Equip. 889 (2018) 97–104. doi:10.1016/j.nima.2018.01.093.
[79] A. Rubio, J.J. Freire, I.F. Pièrola, A. Horta, Excimer-Forming Sites of Poly(methylphenylsi1oxane), Macromolecules. 22 (1989) 4014–4019.
[80] J.J. Freire, I.F. Pièrola, A. Horta, Conformational Analysis of Methyl - Phenyl - Siloxane Chains, Macromolecules. 29 (1996) 5143–5148.
[81] I.B. Berlman, O.J. Steingraber, Liquid scintillation solution for pulse-shape discrimination, Nucl. Inst. Methods Phys. Res. (1973) 587–591.
[82] D.L. Horrocks, Scintillation efficiencies at high solute concentrations: Possible energy transfer from S3 states of excited aromatic solvents, J. Chem. Phys. 52 (1970) 1566–1572. doi:10.1063/1.1673168.
[83] J.B. Birks, M. Salete, S.C.P. Leite, Energy transfer in organic systems. IX. Effect of diffusion on transfer efficiency, J. Phys. B At. Mol. Phys. 3 (1970) 513–525. doi:10.1088/0022-3700/3/4/006.
[84] R.A. Agbariat, D. Gill, Extended 2,5-Diphenyloxazole-y-Cyclodextrin Aggregates Emitting 2,5-Diphenyloxazole Excimer Fluorescence, J. Phys. Chem. (1988) 1052–1055.
[85] M. Dalla Palma, T. Marchi, S. Carturan, C. Checchia, G. Collazuol, F. Gramegna, N. Daldosso, V. Paterlini, A. Quaranta, M. Cinausero, M. Degerlier, Pulse Shape Discrimination in Polysiloxane-Based Liquid Scintillator, IEEE Trans. Nucl. Sci. 63 (2016) 1608–1615. doi:10.1109/TNS.2016.2530307.
[86] J.B. Birks, L.G. Christophorou, 'Excimer' fluorescence. IV. Solution spectra of polycyclic hydrocarbons, Proc. R. Soc. London. Ser. A. Math. Phys. Sci. 277 (1964) 571–582. doi:10.1098/rspa.1964.0041.
[87] I.B. Berlman, Transient dimer formation by 2,5-diphenyloxazole, J. Chem. Phys. 34 (1961) 1083–1084. doi:10.1063/1.1731661.
[88] O.J. Steingraber, I.B. Berlman, Versatile technique for measuring fluorescence decay times in the nanosecond region, Rev. Sci. Instrum. 34 (1963) 524–529. doi:10.1063/1.1718424.
[89] J. Yguerabide, M. Burton, Luminescence decay times: concentration effects, J. Chem. Phys. 37 (1962) 1757–1774. doi:10.1063/1.1733366.
[90] Eljien Technology, Https://Eljentechnology.Com/Products/Plastic-Scintillators. (n.d.).
[91] J. Harmon, J. Gaynor, V. Feygelman, J. Walker, Linear polydiorganosiloxanes as plastic bases for radiation hard scintillators, Nucl. Inst. Methods Phys. Res. B. 53 (1991) 309–314. doi:10.1016/0168-583X(91)95619-O.
[92] M. Moszyński, G.J. Costa, G. Guillaume, B. Heusch, A. Huck, S. Mouatassim, Study of n-γ discrimination with NE213 and BC501A liquid scintillators of different size, Nucl. Inst. Methods Phys. Res. A. 350 (1994) 226–234. doi:10.1016/0168-9002(94)91169-X.

[93] M. Moszyński, M. Kapusta, M. Mayhugh, D. Wolski, S.O. Flyckt, Absolute light output of scintillators, IEEE Trans. Nucl. Sci. 44 (1997) 1052–1061. doi:10.1109/23.603803.

[94] G. Hull, S. Du, T. Niedermayr, S. Payne, N. Cherepy, A. Drobshoff, L. Fabris, Light collection optimization in scintillator-based gamma-ray spectrometers, Nucl. Instruments Methods Phys. Res. Sect. A Accel. Spectrometers, Detect. Assoc. Equip. 588 (2008) 384–388. doi:10.1016/j.nima.2008.01.092.

[95] J.T.M. De Haas, P. Dorenbos, Advances in yield calibration of scintillators, IEEE Trans. Nucl. Sci. 55 (2008) 1086–1092. doi:10.1109/TNS.2008.922819.

[96] K. Banerjee, T.K. Ghosh, S. Kundu, T.K. Rana, C. Bhattacharya, J.K. Meena, G. Mukherjee, P. Mali, D. Gupta, S. Mukhopadhyay, D. Pandit, S.R. Banerjee, S. Bhattacharya, T. Bandyopadhyay, S. Chatterjee, Variation of neutron detection characteristics with dimension of BC501A neutron detector, Nucl. Instruments Methods Phys. Res. Sect. A Accel. Spectrometers, Detect. Assoc. Equip. 608 (2009) 440–446. doi:10.1016/j.nima.2009.07.034.

[97] B. Wan, X.Y. Zhang, L. Chen, H.L. Ge, F. Ma, H. Bin Zhang, Y.Q. Ju, Y. Bin Zhang, Y.Y. Li, X.W. Xu, Digital pulse shape discrimination methods for n-γ separation in an EJ-301 liquid scintillation detector, Chinese Phys. C. 39 (2015). doi:10.1088/1674-1137/39/11/116201.

[98] C. Wu, B. Tang, Z.J. Sun, Q. Zhang, Z. Yang, J. Zhang, Y.D. Yang, J.C. Liang, J.J. Wu, A study of ZnS(Ag)/6LiF with different mass ratios, Radiat. Meas. 58 (2013) 128–132. doi:10.1016/j.radmeas.2013.04.004.

[99] https://eljentechnology.com/products/neutron-detectors/ej-426, (n.d.).

[100] M.-L. Mauborgne, F. Allioli, C. Stoller, M. Evans, M. Manclossi, L. Nicoletti, Exploring for oil with nuclear physics, EPJ Web Conf. 146 (2017) 09009. doi:10.1051/epjconf/201714609009.

[101] F. Wang, X. Fan, D. Pi, M. Wang, Synthesis and luminescence behavior of Eu3+-doped CaF2nanoparticles, Solid State Commun. 133 (2005) 775–779. doi:10.1016/j.ssc.2005.01.014.

[102] X. He, X. Han, H. Wang, B. Wang, B. Wu, Polysiloxanes-based stationary phases containing methoxy-substituted tetraphenyl–phenyl groups for gas chromotographic separations, RSC Adv. 6 (2016) 76514–76523. doi:10.1039/C6RA19537G.

[103] Y. Uehara, Electronic structure of luminescence center of ZnS:Ag phosphors, J. Chem. Phys. 62 (1975) 2982–2994. doi:10.1063/1.430903.

[104] F. Pino, L. Stevanato, D. Cester, G. Nebbia, L. Sajo-Bohus, G. Viesti, Study of the thermal neutron detector ZnS(Ag)/LiF response using digital pulse processing, J. Instrum. 10 (2015). doi:10.1088/1748-0221/10/08/T08005.

[105] Y. Abreu, Y. Amhis, L. Arnold, G. Ban, W. Beaumont, M. Bongrand, D. Boursette, J.M. Buhour, B.C. Castle, K. Clark, B. Coupé, A.S. Cucoanes, D. Cussans, A. De Roeck, J. D'Hondt, D. Durand, M. Fallot, S. Fresneau, L. Ghys, L. Giot, B. Guillon, G. Guilloux, S. Ihantola, X. Janssen, S. Kalcheva, L.N. Kalousis, E. Koonen, M. Labare, G. Lehaut, J. Mermans, I. Michiels, C. Moortgat, D. Newbold, J. Park, K. Petridis, I. Piñera, G. Pommery, L.

Popescu, G. Pronost, J. Rademacker, A. Reynolds, D. Ryckbosch, N. Ryder, D. Saunders, Y.A. Shitov, M.H. Schune, P.R. Scovell, L. Simard, A. Vacheret, S. Van Dyck, P. Van Mulders, N. Van Remortel, S. Vercaemer, A. Waldron, A. Weber, F. Yermia, A novel segmented-scintillator antineutrino detector, J. Instrum. 12 (2017). doi:10.1088/1748-0221/12/04/P04024.

[106] M. Anni, L. Manna, R. Cingolani, D. Valerini, A. Cretí, M. Lomascolo, Förster energy transfer from blue-emitting polymers to colloidal CdSe/ZnS core shell quantum dots, Appl. Phys. Lett. 85 (2004) 4169–4171. doi:10.1063/1.1814795.

[107] A.R. Clapp, I.L. Medintz, B.R. Fisher, G.P. Anderson, H. Mattoussi, Can luminescent quantum dots be efficient energy acceptors with organic dye donors?, J. Am. Chem. Soc. 127 (2005) 1242–1250. doi:10.1021/ja045676z.

[108] A.R. Clapp, I.L. Medintz, J.M. Mauro, B.R. Fisher, M.G. Bawendi, H. Mattoussi, Fluorescence Resonance Energy Transfer between Quantum Dot Donors and Dye-Labeled Protein Acceptors, J. Am. Chem. Soc. 126 (2004) 301–310. doi:10.1021/ja037088b.

[109] M. Lunz, A.L. Bradley, Förster resonance energy transfer in CdTe nanocrystal quantum dot structures, in: J.F. Donegan, Y. Rakovich (Eds.), Cadmium Telluride Quantum Dots Adv. Appl., 2014.

[110] R. Huszank, S.Z. Szilasi, D. Szikra, Ion-Energy Dependency in Proton Irradiation Induced Chemical Processes of Poly(dimethylsiloxane), J. Phys. Chem. C. 117 (2013) 25884–25889. doi:10.1021/jp406984d.

[111] V. Borjanovic, W.G. Lawrence, S. Hens, M. Jaksic, I. Zamboni, C. Edson, I. Vlasov, O. Shenderova, G.E. McGuire, Effect of proton irradiation on photoluminescent properties of PDMS-nanodiamond composites, Nanotechnology. 19 (2008) 455701. doi:10.1088/0957-4484/19/45/455701.

[112] V. Borjanović, L. Bistričić, I. Vlasov, K. Furić, I. Zamboni, M. Jakšić, O. Shenderova, Influence of proton irradiation on the structure and stability of poly(dimethylsiloxane) and poly(dimethylsiloxane)-nanodiamond composite, J. Vac. Sci. Technol. B Microelectron. Nanom. Struct. 27 (2009) 2396. doi:10.1116/1.3258156.

[113] B. Farhood, M.T. Bahreyni Toossi, H. Vosoughi, S. Khademi, C. Knaup, Measurement of thyroid dose by TLD arising from radiotherapy of breast cancer patients from supraclavicular field, J. Biomed. Phys. Eng. 6 (2016) 147–156.

[114] X. Wang, L. Qu, J. Zhang, X. Peng, M. Xiao, Surface-related emission in highly luminescent CdSe quantum dots, Nano Lett. 3 (2003) 1103–1106. doi:10.1021/nl0342491.

[115] Y.T. Lim, M.Y. Cho, J.H. Kang, Y.W. Noh, J.H. Cho, K.S. Hong, J.W. Chung, B.H. Chung, Perfluorodecalin/[InGaP/ZnS quantum dots] nanoemulsions as19F MR/optical imaging nanoprobes for the labeling of phagocytic and nonphagocytic immune cells, Biomaterials. 31 (2010) 4964–4971. doi:10.1016/j.biomaterials.2010.02.065.

[116] A. Joshi, M.O. Manasreh, E.A. Davis, B.D. Weaver, Optical properties of colloidal InGaP/ZnS core/shell nanocrystals, Appl. Phys. Lett. 89 (2006) 1–

4. doi:10.1063/1.2354031.
[117] G. Schlegel, J. Bohnenberger, I. Potapova, A. Mews, Fluorescence Decay Time of Single Semiconductor Nanocrystals, Phys. Rev. Lett. 88 (2002) 4. doi:10.1103/PhysRevLett.88.137401.
[118] W.Z. Lee, G.W. Shu, J.S. Wang, J.L. Shen, C.A. Lin, W.H. Chang, R.C. Ruaan, W.C. Chou, C.H. Lu, Y.C. Lee, Recombination dynamics of luminescence in colloidal CdSe/ZnS quantum dots, Nanotech. 16 (2005) 1517–1521. doi:10.1088/0957-4484/16/9/018.
[119] B.O. Dabbousi, J. Rodriguez-Viejo, F. V. Mikulec, J.R. Heine, H. Mattoussi, R. Ober, K.F. Jensen, M.G. Bawendi, (CdSe)ZnS Core−Shell Quantum Dots: Synthesis and Characterization of a Size Series of Highly Luminescent Nanocrystallites, J. Phys. Chem. B. 101 (1997) 9463–9475. doi:10.1021/jp971091y.
[120] S. Chang, X. Wu, J. Lan, Z. Li, X. Zhang, H. Zhang, γ-Radiation Enhanced Luminescence of Thiol-Capped Quantum Dots in Aqueous Solution, Nanomaterials. 9 (2019) 506. doi:10.3390/nano9040506.
[121] E. Zanazzi, M. Favaro, A. Ficorella, L. Pancheri, G.F. Dalla Betta, A. Quaranta, Radiation-induced optical change of ion-irradiated CdSeS/ZnS core-shell quantum dots embedded in polyvinyl alcohol, Nucl. Instruments Methods Phys. Res. Sect. B Beam Interact. with Mater. Atoms. 435 (2018) 327–330. doi:10.1016/j.nimb.2018.05.027.
[122] K. Sharma, R.P. Chahal, S. Mahendia, A.K. Tomar, S. Kumar, Optical behaviour of swift heavy ions irradiated poly (vinyl alcohol) films, Radiat. Eff. Defects Solids. (2013) 37–41. doi:10.1080/10420150.2013.767250.
[123] F.A. Mir, A. Gani, K. Asokan, Gamma irradiation studies of composite thin films of poly vinyl alcohol and coumarin, RSC Adv. 6 (2016) 1554–1561. doi:10.1039/C5RA15633E.
[124] K. Chou, A. Dennis, Förster Resonance Energy Transfer between Quantum Dot Donors and Quantum Dot Acceptors, Sensors. 15 (2015) 13288–13325. doi:10.3390/s150613288.

Scientific Production

Published papers

E. Zanazzi, M. Favaro, A. Ficorella, L. Pancheri, G. F. Dalla Betta, A. Quaranta, "*Radiation-induced optical change of ion-irradiated CdSeS/ZnS core-shell quantum dots embedded in polyvinyl alcohol"*, Nuclear Inst. And Methods in Physics Research B, 435 (2018) 327–330.

E. Zanazzi, M. Favaro, A. Ficorella, L. Pancheri, G. F. Dalla Betta, A. Quaranta, "*Proton Irradiation Effects on Colloidal InGaP/ZnS Core-Shell Quantum Dots Embedded in Polydimethylsiloxane: Discriminating Core from Shell Radiation-Induced Defects through Time-Resolved Photoluminescence Analysis"*, J. Phys. Chem. C, 122 (2018) 22170−22177.

E. Zanazzi, M. Favaro, A. Ficorella, L. Pancheri, G. F. Dalla Betta, A. Quaranta, "*Photoluminescence enhancement of colloidal CdSe/ZnS quantum dots embedded in polyvinyl alcohol after 2 MeV proton irradiation: crucial role of the embedding medium"*, Optical Materials, 88 (2019) 271–276.

S.M. Carturan, M. Vesco, I. Bonesso, A. Quaranta, G. Maggioni, L. Stevanato, E. Zanazzi, T. Marchi, M. Cinausero, F. Gramegna, "*Siloxane-based ^{6}LiF composites for flexible thermal neutron detectors with high efficiency: effects of ^{6}LiF crystals size and dispersion homogeneity"*, Nuclear Inst. And Methods in Physics Research A, 925 (2019) 109–115.

T. Marchi , F. Pino, C. L. Fontana, A. Quaranta, E. Zanazzi, M. Vesco, M. Cinausero, N. Daldosso, V. Paterlini, F. Gramegna, S. Moretto, G. Collazuol, M. Degerlier, D. Fabris & S. M. Carturan, "*Optical properties and pulse shape discrimination in siloxane-based scintillation detectors",* Scientific Reports, 9 (2019) 9154.

E. Zanazzi, M. Favaro, A. Ficorella, L. Pancheri, G. F. Dalla Betta, A. Quaranta, "*Real-Time Optical Response of Polysiloxane/Quantum Dot Nanocomposite under 2 MeV Proton Irradiation: Luminescence Enhancement of the Polysiloxane Emission through Quantum Dot Sensitization"*, Phys. Status Solidi A, 217 (2020), 1900586

Presentations at conferences, schools and workshops

Poster presentation at the 19th international conference on Radiation Effects in Insulators (REI 19), 2nd-7th July 2017, Versailles, France, "*Effects of ion irradiation on colloidal core-shell quantum dots embedded in polymeric matrices for dosimetry applications*".

Oral presentation at the 103rd Congress of Italian Physical Society (Società Italiana di Fisica, SIF), 11th -15th September 2017, Trento, Italy, "*Effects of ion irradiation on colloidal core-shell quantum dots embedded in polymeric matrices for dosimetry applications*".

Poster presentation at the Advanced School of quantum detectors (SQUAD 2017), 16th -18th October 2017, Trento, Italy, "*Effects of ion irradiation on colloidal core-shell quantum dots embedded in polymeric matrices for dosimetry applications*".

Poster presentation at the workshop "Photonics as a key enabling technology" 17th November 2017, Bruno Kessler Foundation (FBK), Trento, Italy, "*Effects of ion irradiation on colloidal core-shell quantum dots embedded in polymeric matrices for dosimetry applications*".

Poster presentation at the Summer School on Neutron Detectors (NDRA 2018), 2nd - 5th July, 2018, Riva del Garda (TN), Italy, *"Proton irradiation effects on colloidal InGaP/ZnS core-shell quantum dots embedded in polydimethylsiloxane: discriminating core from shell radiation-induced defects through time-resolved photoluminescence analysis".*

Oral presentation at the European Material Research Society (EMRS) 2019 Spring Meeting, 27th-31st May 2019, Nice, France, Symposium W: semiconductor nanostructures towards electronic and opto-electronic device applications, *"Proton irradiation effects on colloidal InGaP/ZnS core-shell quantum dots embedded in polydimethylsiloxane: discriminating core from shell radiation-induced defects through time-resolved photoluminescence analysis"*.

Acknowledgement

Come to the end of this doctoral course, I would like to thank several people who contributed to this work and to this growth experience.
First of all, I would like to express my gratitude to Prof. Alberto Quaranta, for trusting me in undertaking the doctoral course, following me constantly during the entire activity and for providing motivation.
Secondly, I wish to thank very much Dr. Sara Carturan since without her work part of this thesis wouldn't have been possible. Then, a special thanks is dedicated to my colleague Matteo Favaro for his important contribution through his very professional technical support. Moreover, I wish to thank for their help Andrea Ficorella, Prof. Lucio Pancheri and Prof. Gian Franco Dalla Betta.
Lastly, I would like to thank Prof. Sandra Dirè and Prof. Luca Fambri for their annual feedback during the admission exams.

Enrico Zanazzi